

Retinal dynamic vascular biomarkers of arterial stiffness

Mahdieh Rezaeian (*M. Eng*)

A thesis of The Department of Clinical Sciences, Faculty of Medicine and Health Sciences, Macquarie University, submitted in fulfilment of the requirements for the degree of Doctor of Philosophy.

Supervisor:

Professor Stuart Graham

Associate supervisors:

Professor Alberto Avolio

Doctor Mark Butlin

Doctor Mojtaba Golzan

March 2019



MACQUARIE
University
SYDNEY • AUSTRALIA

Declaration of originality

I hereby declare that the work presented in this thesis has not been submitted for a higher degree to any other university or institution. To the best of my knowledge this submission contains no material previously published or written by another person, except where due reference is stated otherwise. Any contribution made to the research by others is explicitly acknowledged.

Mahdieh Rezaeian

Department of Clinical Sciences
Faculty of Medicine and Health Sciences
Macquarie University

March 2019

Declaration of contributions

Chapter 4: The candidate was the major contributor to this work. The experiment was directed by Dr Mojtaba Golzan and data was collected by Dr Golzan and Miss Dana Georgevsky in 2015 before the candidate commenced her PhD. All the processing and analysis of the data were performed by the candidate.

Chapter 5: The candidate was the major contributor to the experiment presented in this chapter. The experiment was directed by Dr Mark Butlin. Miss Dana Georgevsky collaborated in animal preparation and data collection. Retinal recordings and all analysis were performed by the candidate.

Chapter 6: The candidate was the major contributor to this work. The study was designed by Dr Mojtaba Golzan. The data was collected by Miss Dana Georgevsky. All the data processing and analysis were performed by the candidate.

Chapter 7: The experiment was directed by Dr Mark Butlin. Dr Angela Schulz collaborated in retina dissection and OCT recordings. The tensile testing was performed by Dr Mark Butlin and Dr Arthur Leloup. Retinal dissection, tissue preparation and microscopy, and OCT recordings were performed by the candidate. Prof Alberto Avolio provided essential intellectual contribution to the analysis. The manuscript was co-written by the candidate with Dr Mark Butlin.

Ethics approval

All procedures presented in this thesis were conducted under appropriate ethics approval. All animal experiments (Chapter 4Chapter 5) were conducted in accordance with the Australian Code for the care and use of animals for scientific purposes and were approved by the Macquarie University Animal Ethics Committee (Ethics committee reference number: 2014/055-2 and 2016/005 respectively). The human study presented in Chapter 6 was performed in accordance with the guidelines of the Tenants of Helsinki and approved by the Macquarie University Human Ethics Committee (reference number: 5201200786). Written informed consent was obtained from all participants.

Acknowledgements

I would like to acknowledge and thank my supervisors, Prof. Stuart Graham, and Dr Mojtaba Golzan for their encouragement, support and feedback during my candidature. I wish to express my heartfelt appreciation to Prof Alberto Avolio and Dr Mark Butlin for their generous and continuing help, guidance and insightful comments. This thesis would not be possible without their precious input.

I would like to take the opportunity to appreciate Dr Angela Schulz, Arthur Leloup, and Dana Georgevsky for their help with the experiments and Dr Mehdi Mirzaei, Dr Daneh Turner, and Dr Vivek Gupta for their kind support.

I would also like to thank my sweet friends Fatemeh Shirbani, Sara Alavi, Mojdeh Abbasi, Shila Shahbazian and Isabella Tan and all my lab mates for the great time we had together.

And I would like to extend my sincere gratitude to the blessings of my life, my parents and my lovely sister for their ongoing support and unconditional love.

Publications

Journal publications

1. **Rezaeian M**, Golzan SM, Graham SL, Avolio PA, Butlin M. Pressure dependency of retinal arterial pulse wave velocity in the rat. [manuscript in preparation].
2. **Rezaeian M**, Golzan SM, Avolio PA, Butlin M, Graham SL. The association between retinal and central pulse wave velocity in the elderly. [manuscript in preparation].
3. Butlin M, **Rezaeian M**, Schulz A, Leloup A, Golzan SM, Graham SL, Avolio PA. Calculation of retinal artery pulse wave velocity. *Experimental Eye Research*. 2019 [under review].
4. Mirzaei M, Gupta VB, Chick JM, Greco TM, Wu Y, Chitranshi N, Vander Wall R, Hone E, Deng L, Dheer Y, Abbasi M, **Rezaeian M**, Braidy N, You Y, Hosseini Salekdeh G, Haynes PA, Molloy M.P, Martins R, Cristea IM, Gygi SP, Graham SL, Gupta VK. Age-related neurodegenerative disease associated pathways identified in retinal and vitreous proteome from human glaucoma eyes. *Scientific Reports* 7.1 (2017): p.12685.
5. Shariflou S, Georgevsky D, Mansour H, **Rezaeian M**, Hosseini N, Gani F, Gupta V, Braidy N, Golzan SM. Diagnostic and prognostic potential of retinal biomarkers in early on-set Alzheimer`s disease. *Curr Alzheimer Res*. 14.9 (2017): 1000-1007.

Full-length, peer-reviewed conference proceedings

6. **Rezaeian M**, Butlin M, Golzan SM, Graham SL, Avolio P.A. A Novel Method for Retinal Vessel Segmentation and Diameter Measurement Using High Speed Video. *Conf Proc IEEE Eng Med Biol Soc*. 2019 July.
7. **Rezaeian M**, Georgevsky D, Golzan SM, Graham SL. High speed *in-vivo* imaging of retinal hemodynamics in a rodent model of hypertension. *Conf Proc IEEE Eng Med Biol Soc*. 2016 Aug; 2016:3243-3246.

Conference abstracts

8. **Rezaeian M**, Leloup A, Schulz A, Golzan SM, Graham SL, Avolio PA, Butlin M, Discrepancy between *in-vivo* measure and *ex-vivo* estimate of pulse wave velocity in retinal arteries. ARTERY 2018, Guimarães, Portugal, October 2018.
9. **Rezaeian M**, Georgevsky D, Golzan SM, Graham SL, Avolio PA, Butlin M. Novel Retinal Pulse Transit Time Measurement Shows Expected Blood Pressure Dependency in Rodents. EVER 2018, Nice, France, October 2018.
10. **Rezaeian M**, Oliver R, Butlin M, Avolio PA, Golzan SM, Graham SL, A Novel Method for Retinal Vessel Segmentation and Diameter Measurement in High Speed Fundus Videos. ICBES 2018, Madrid, Spain, August 2018.
11. **Rezaeian M**, Schulz A, Leloup A, Abbasi M, Golzan SM, Graham SL, Avolio PA, Butlin M. Arterial Stiffness and Pulse Wave Velocity Quantification in Bovine Retinal Arteries. ARVO 2018, Honolulu, Hawaii, May 2018.
12. **Rezaeian M**, Georgevsky D, Golzan SM, Graham SL. The Association between Retinal and Central Aortic Pulse Wave Velocity in the elderly. ARVO-Asia 2017, Brisbane, Australia, February 2018.

Awards arising during candidature

Macquarie University Postgraduate Research Fund 2018

Skipper-Jacobs Travel Grant 2017

Arvo-Asia Travel Grant 2017

Macquarie University Research Training Program (MQRTP) Scholarship 2015

Abstract

Arterial stiffness is an independent predictor of cardiovascular events. Cardiovascular diseases have been the leading causes of mortality across the globe over the past 15 years. There is a growing recognition of the links between small and large vessels impairment in arterial stiffness. However, fundamental aspects of small-artery stiffness are poorly understood and need further research.

Retinal microvasculature provides direct access to the microcirculation easily and non-invasively. Previous studies suggest microvascular remodelling occurs in association with arterial stiffness. Assuming retinal vessels display the same changes seen in other small resistance arteries, they should also undergo structural changes in response to arterial stiffness. The current research investigates whether dynamic characteristics of retinal vessels including pulsatility and arterial pulse transit time derived from diameter waveforms are associated with large artery stiffening.

This thesis presents a novel method for the measurement of pulsatile diameter changes both in the human and rat retinal vessels. Experimental studies in rats demonstrated retinal arteriolar narrowing and reduced arterial pulse amplitude in presence of hypertension. In addition, a strong positive correlation was found between pulse wave velocity in retinal arteries and increasing blood pressure. These observations are in accordance with known vasoconstriction-induced inward remodelling of resistance vessels and pressure dependence of arterial stiffness as suggested from previous studies in large arteries. Furthermore, a clinical study on a group of elderly volunteers showed a strong positive linear relationship between pulse wave velocity in retinal arteries and pulse wave velocity measured between carotid and femoral arteries as the gold-standard clinical marker of arterial stiffness, for the first time. Moreover, in the identification of the theoretical value of the pulse wave velocity in

retinal arteries, an *in-vitro* experiment was conducted to measure the elastic modulus of the retinal arteries for the first time and a wave speed in order of cm/s was estimated which is two orders of magnitude slower than pulse wave velocity in large arteries.

Investigation of dynamic characteristics of retinal vessels may help to provide insights into the pathophysiology and development of stiffness in small arteries. It can also help in possible therapeutic strategies not only in hypertension and arterial stiffness but also in a range of ocular and vascular-related pathogenesis.

Table of Contents

Declaration of originality	i
Declaration of contributions	ii
Ethics approval	iii
Acknowledgements	iv
Publications	v
Abstract	vii
Table of Contents	ix
List of Figures	xiv
List of Tables	xvii
List of Abbreviations	xviii
Chapter 1 Introduction	19
1.1 Background	19
1.2 Problem statement	20
1.3 Hypothesis	21
1.4 Research aims and objectives	21
1.5 Thesis outline	21
Chapter 2 Literature Review	23
2.1 Arterial stiffness	24
2.2 Mechanisms of arterial stiffness	26
2.2.1 Structural changes	27
Compositional changes	27
2.2.2 Functional changes	27
Blood pressure	27
Impaired smooth muscle function	28
2.2.3 Signaling Mechanisms	28
Nitric Oxide (NO)	28
2.3 Indices of arterial stiffness	29
2.4 Measurement of pulse wave velocity in large arteries	32
2.5 Arterial stiffness in the microcirculation	34

2.5.1	Microcirculatory imaging techniques	36
2.6	The Retina as a window to the microcirculation	37
2.6.1	Retinal circulation	40
2.6.2	Ocular imaging modalities	42
	Fluorescein Angiography	43
	Scanning Laser Ophthalmoscopy	43
	Optical Coherence Tomography	43
	Adaptive Optics	44
	Dynamic/Retinal Vessel Analyzer	45
2.6.3	Retinal vessels: a proxy for assessment of systemic blood pressure variations	46
2.7	Quantifying retinal vascular characteristics	48
2.7.1	Static indices	49
	Retinal vascular caliber	49
	Vascular tortuosity	51
	Vascular bifurcation angle	52
	Fractal dimension	52
2.7.2	Dynamic indices	53
	Pulsatility	53
	Retinal pulse wave velocity	53
2.8	Techniques for retinal vessel segmentation and diameter measurement	58
2.8.1	Vessel segmentation	58
2.8.2	Vessel diameter measurement	65
Chapter 3 Retinal PWV - method and modelling		68
3.1	High-speed imaging	69
3.2	Proposed method for retinal vessel analysis	69
3.3	Segmentation of retinal vessels	71
3.3.1	Intensity adjustment	71
3.3.2	Registration and alignment of image stack	72
3.3.3	ROI extraction	72
3.3.4	Anisotropic diffusion	73
3.3.5	Segmentation of the vessel boundaries	75

3.4	Measurement of vessel diameter	76
3.5	Pulse transit time calculation	80
3.6	Evaluation of Methods	82
3.6.1	Vessel segmentation	82
3.6.2	Diameter measurement	83
3.7	Comment and implications for the evaluation of PTT measurement	86
Chapter 4 Pulse diameters in normotensive and hypertensive rats		88
	Abstract	88
4.1	Introduction	89
4.2	Methods	91
4.2.1	Animal preparation and video acquisition	91
4.2.2	Video Analysis	91
	Contrast Limited Adaptive Histogram Equalization	92
	Eulerian Video Magnification	92
	Contrast Enhancement	94
	Diameter Measurement	94
	Pulse Amplitude	95
	Calibration	96
4.3	Results and discussion	96
4.3.1	Retinal arterial and venues diameter	97
4.3.2	Pulse amplitude	97
4.3.3	Limitations	98
4.4	Conclusion	99
	Acknowledgment	99
Chapter 5 Pressure dependency of retinal arterial pulse wave velocity in the rat		100
5.1	Introduction	101
5.2	Methods	102
5.2.1	Animal preparation	102
5.2.2	Measurement of retinal artery diameter and PWV	103
5.2.3	Alteration of BP	104
5.2.4	Measurement of aPWV	106

5.3	Results	106
5.4	Discussion	113
Chapter 6 Retinal vs central pulse wave velocity in the elderly		116
6.1	Introduction	117
6.2	Methods	118
6.2.1	Subjects and Instruments	118
6.2.2	cPWV measurement	119
6.2.3	Measurement of retinal pulse wave velocity (rPWV)	120
6.2.4	Statistical analysis	121
6.3	Results	121
6.4	Discussion	128
Chapter 7 Calculation of retinal artery pulse wave velocity		132
	Abstract	132
7.1	Introduction	133
7.2	Materials and methods	136
7.2.1	Geometry measurement	136
7.2.2	Tensile testing	137
7.2.3	Calculations	138
7.2.4	Statistics	141
7.3	Results	141
7.4	Discussion	143
7.5	Conclusions	147
	Acknowledgments	147
	Declaration of interest	147
Chapter 8 Discussion		148
8.1	Summary of contributions and findings	149
8.2	Limitations and future directions	152
8.3	Conclusions	153
References		154
Appendix		166

References	170
Ethics approvals	171

List of Figures

Figure 2.1. Elastic versus muscular artery	26
Figure 2.2. Compliant vs Stiff artery	30
Figure 2.3. Augmentation index	31
Figure 2.4. Central PWV measured between carotid and femoral arteries.....	33
Figure 2.5. Inward remodeling patterns in microvasculature	35
Figure 2.6. Schematic structure of the human eye.....	38
Figure 2.7. Cell layers of the human retina.....	39
Figure 2.8. DVA system	45
Figure 2.9. Measurement of CRAE and CRVE.....	50
Figure 2.10. An illustration of a retinal vessel in a fundus image	66
Figure 3.1. Block diagram of the proposed method for the measurement of PWV in retinal arteries.....	71
Figure 3.2. The original image (left) and the output of CLAHE (right).....	72
Figure 3.3. An example of ROI extraction.	73
Figure 3.4. Anisotropic diffusion filtering.....	75
Figure 3.5. Vessel boundaries segmentation	76
Figure 3.6. Left: vessel segmentation; right: same image after length filtering	76
Figure 3.7. Vessel borders are segregated using the medial line of the vessel.	77
Figure 3.8. Retinal arterial pulse obtained from diameter changes in the rat eye.	77
Figure 3.9. Finding the centerline of the vessel using inverse Hough transform..	79
Figure 3.10. Replacing missing values and outliers with cubic spline interpolation.....	80
Figure 3.11. Retinal arterial diameter changes in the rat eye.	81
Figure 3.12. Calculation of PTT	81
Figure 3.13. Representative segmentation results	82
Figure 3.14. ROC curve for segmentation results of 25 images.....	83

Figure 3.15. Bland-Altman plot	86
Figure 4.1. The block diagram of the proposed method for the measurement of retinal vessels pulsations.	91
Figure 4.2. The original image (left) and the result of CLAHE (right)..	92
Figure 4.3. Local contrast enhancement using ImageJ W/L plugin..	94
Figure 4.4. Baseline elimination..	95
Figure 4.5. Proximal and distal sites along artery and vein..	96
Figure 5.1. Illustration of BP manipulation procedure	105
Figure 5.1. Retinal arterial diameter waveform (A) have power at cardiac frequency (B). ..	106
Figure 5.2. Retinal arterial PWV increases exponentially with increasing blood pressure...107	
Figure 5.3. Comparison between rPWV sensitivity to DBP (A), SBP (B), MAP (C).....	108
Figure 5.4. Manipulation of MAP by infusion of PE, SNP and the use of VO	109
Figure 5.5. rPWV regression on DBP, SBP, and MAP at baseline, during vasoactive drug infusion, and venous return reduction.....	110
Figure 5.6. Linear regression of (A) rPWV on aPWV; (B) aPWV on MAP; and (C) rPWV on MAP.....	112
Figure 6.1. cPWV measurement.	120
Figure 6.2. Calculation of PTT	121
Figure 6.3. rPWV regression on cPWV.....	124
Figure 6.4. Regression model of rPWV based on cPWV.....	125
Figure 6.5. Estimation of the effect of IOP on rPWV with a linear regression	125
Figure 6.6. Regression model of rPWV based on cPWV after correction of confounding effect of IOP.....	126
Figure 6.7. Comparison of (A) BP values including DBP, SBP, and MAP, (B) rPWV, and (C) cPWV between deciles of age	127
Figure 6.8. Regression lines representing the effect of age on SBP, MAP, and DBP.....	130

Figure 7.1. An example of an optical coherence tomography image of the bovine retina. ...	137
Figure 7.2. Retinal artery segment mounted for tensile testing.....	138
Figure 7.3. The measured relationship between stress (σ) and strain (ϵ) for 9 tested bovine retinal arteries.. ..	142
Figure 7.4. Calculated retinal pulse wave velocity.....	142
Figure 7.5. Reported values of retinal pulse wave velocity (PWV) in the literature as measured <i>in-vivo</i> using imaging techniques.	144

List of Tables

Table 2.1. Comparison of reported values of rPWV in the literature.	57
Table 3.1. Specificity and sensitivity of the vessel segmentation over 25 vessel segments	84
Table 4.1. Results (measurements are in Micron).....	97
Table 5.1. Model summary and parameter estimates of rPWV as a function of MAP.....	107
Table 5.2. Coefficients of the exponential model: $rPWV = c \times e^{b \times \text{Variable}}$	108
Table 5.3. Tukey's Honest Significant Difference (HSD) test comparing pressure sensitivity of rPWV to blood pressure during each episode	108
Table 5.4. Coefficients for exponential regression $rPWV = c \times e^{b \times \text{Variable}}$	111
Table 5.5. Coefficients for the linear regression $y = c + b \times \text{Variable}$	112
Table 6.1. Demographics of the normotensive and hypertensive subjects	122
Table 6.2. Results of Levene's test for homoscedasticity and t test for comparing biometrics of normal and hypertensive subjects.....	123
Table 6.3. Correlation coefficients of rPWV with age, MAP, IOP, and cPWV in normal and hypertensive subjects obtained by a step-wise linear regression analysis	123
Table 6.4. Demographics of the subjects	127
Table 6.5. Correlation coefficients of rPWV adjusted to IOP with age, DBP, SBP, MAP, and cPWV in two deciles of age obtained by a step-wise linear regression analysis.....	128
Table 7.1. Bovine retinal artery segment measurement by microscopy (length) and optical coherence tomography (luminal diameter, wall thickness).	141

List of Abbreviations

aPWV	Aortic Pulse Wave Velocity
AVR	Arteriovenous Ratio
BP	Blood Pressure
CHD	Coronary Heart Disease
CLAHE	Contrast Limited Adaptive Histogram Equalization
cPWV	Central Pulse Wave Velocity
CRAE	Central Retinal Arteriolar Equivalent
CRVE	Central Retinal Venular Equivalent
CVD	Cardio-Vascular Disease
DBP	Diastolic Blood Pressure
DVA	Dynamic Vessel Analyzer
ECG	Electrocardiogram
IOP	Intra Ocular Pressure
MAP	Mean Arterial Pressure
NO	Nitric Oxide
OCT	Optical Coherence Tomography
PE	Phenylephrine
PEVO	Phenylephrine infusion and Venous Occlusion
PP	Pulse Pressure
PTT	Pulse Transit Time
PWV	Pulse Wave Velocity
ROC	Receiver Operating Characteristic
ROI	Region of Interest
rPWV	Retinal Pulse Wave Velocity
SBP	Systolic Blood Pressure
SD	Sprague Dawley
SHR	Spontaneously Hypertensive Rat
SNP	Sodium Nitroprusside
SNR	Signal to Noise Ratio
VO	Venous Occlusion
vRBC	Velocity of the Red Blood Cells
WKY	Wistar-Kyoto

Chapter 1

Introduction

1.1 Background

The retinal vasculature provides readily visible information about the state of the systemic circulation. Furthermore, the retinal vasculature can be directly and non-invasively visualized and photographed. These unique features make the retina an ideal window to study not only ocular but also vascular-specific pathophysiology.

Over the last decade, many studies have demonstrated retinal vascular changes associated with various diseases including hypertension (Wong et al. 2003; Wong 2004; Wong et al. 2004; Ding et al. 2014; Oluleye et al. 2016), diabetes (Nguyen et al. 2009)(Sabanayagam et al. 2015), sleep apnoea (Tong et al. 2017), glaucoma (Kawasaki et al. 2013; Chan et al. 2017) and dementia (Heringa et al. 2013; Cheung et al. 2014; Williams et al. 2015). This highlights the potential for using the retinal vasculature in the assessment of microvascular abnormalities with clear advantages due to non-invasive and direct access.

Retinal vascular alterations may manifest either as local or global morphological changes including branching angle, tortuosity, arterial and venous diameter, and fractal dimension, or

dynamic changes such as pulsatility and pulse wave velocity (PWV). Accordingly, vascular analysis methods are divided into two categories: 1) *static* methods based on a single image and 2) *dynamic* methods using a sequence of images. While static imaging of retinal vasculature can reveal information on vessel calibre, vascular tortuosity and fractal dimension, dynamic analysis of retinal vessels can be used to indicate time dependent indices such as pulsatility index, retinal vasodilation response, and PWV which are shown to be more diseases-specific by offering the possibility of the assessment of vascular function over time.

The current research, in particular, attempts to investigate dynamic characteristics of retinal vessels in association with arterial stiffness as a known risk factor of cardiovascular disease (CVD). The findings of this study may provide a research tool to improve the understanding of the association of the microcirculation in the pathogenesis of arterial stiffness and hypertension and finally, may be clinically useful for prediction and conventional risk stratification of CVD. Furthermore, analysis of dynamic characteristics of retinal vessels will provide a platform for future studies investigating dynamic properties of retinal vessels in association with a wide range of ocular and systemic abnormalities.

1.2 Problem statement

While the retina provides a platform to study the pathophysiology of a wide range of diseases, direct applicability of retinal vascular features in the clinical practice is yet to be established. This is likely due in part to lack of specificity and sensitivity of the proposed markers. For instance, while there is an agreement on retinal arteriolar narrowing in presence of hypertension, studies investigating retinal venular calibre have reported controversial results with one study showing retinal venular widening associated with hypertension (Ding et al. 2014) while the other has reported no significant difference in retinal venular diameter (Wang

et al. 2016). These contradictory reports necessitate studying retinal microvasculature from a dynamic perspective in search of more disease specific biomarkers.

Given the limited number of studies that have utilized dynamic imaging to characterize time-dependent alterations in the retinal vasculature, the first challenge will be to develop appropriate methods to quantify these characteristics.

1.3 Hypothesis

The current research has been conducted based on the hypothesis that dynamic characteristics of retinal vessels, including pulsatile diameter changes and pulse transit time (PTT), are regulated through systemic blood pressure (BP) and accordingly may provide a biological model to study manifestations and pathogenic mechanisms of small artery stiffness.

1.4 Research aims and objectives

Specific aims to address the abovementioned hypothesis include:

1. Develop means of quantifying PTT and PWV in retinal arteries.
2. Determine whether dynamic retinal vascular changes reflect systemic BP changes which arterial stiffness is known to depend on.
3. Determine if there is a direct correlation between PWV in retinal arteries and PWV in large arteries as a marker of arterial stiffness.

1.5 Thesis outline

This thesis has been organized in eight chapters. After a comprehensive review of the literature in Chapter 2, a novel method devised for measuring retinal vessel diameter changes

from fundus videos is presented in Chapter 3. Chapter 4 presents an experimental study comparing arterial and venular retinal diameter pulses between genetically hypertensive rats and controls. The feasibility of measuring PTT in retinal arteries of rats is investigated and results are presented in Chapter 5. To investigate pressure dependency of PWV in retinal arteries, retinal arterial PTT was measured across a physiological range of BP manipulated both through vasoactive substances and through a passive mechanism. Chapter 6 presents a clinical study performed on an elderly cohort to investigate the association between PWV in retinal arteries and PWV in large arteries. Chapter 7. reports the estimation of the theoretical value of PWV in retinal arteries based on the elastic modulus of retinal arteries measured in the bovine eye. Finally, collective findings are discussed and future directions on present research have been provided in Chapter 8.

Chapter 2

Literature Review

This chapter provides an overview on arterial stiffness as a risk factor for CVD. The clinical markers of arterial stiffness, and its manifestations in the retina are presented. A review of prior studies on cardiovascular related changes in retinal vessels has also been provided. In addition, current methods for the segmentation of retinal vessels and diameter measurements are reviewed.

2.1 Arterial stiffness

Arterial stiffness describes a condition of the arterial wall in which the extracellular matrix of elastic arteries loses its elasticity due to elastin degeneration or calcification which occurs with age and in certain diseases including hypertension, diabetes mellitus, and end-stage renal failure (Mitchell et al. 2007).

Arterial stiffness as a predictor of CVD particularly in the elderly (Palombo et al. 2016) has been receiving increasing interest in preventive health care. Cardiovascular disease is a collective term referring to a range of disorders that affect the heart or blood vessels. Common manifestations of CVD include high blood pressure, coronary artery disease, congestive heart failure, arrhythmias, cardiac arrest, peripheral artery disease and stroke. The underlying pathogenesis depends on the disease, but unhealthy diet, physical inactivity, obesity, alcohol, and smoking are among major contributors to CVDs. According to the World Health Organization (WHO), CVD is the leading cause of death around the world (31%) totaling 17.9 million people worldwide in 2016 (World Health Organization 2017). The huge health and economic burdens of CVD highlight the importance of its early screening in aging populations.

The association between CVD risk factors and measures of arterial stiffness has been investigated by several large-population studies. For example, the Framingham study cohort included 2,232 volunteers and presented evidence of arterial stiffness as an independent predictor of cardiovascular events (Laurent et al. 2001; Mitchell et al. 2010). Similar results obtained from the Rotterdam study with 2,835 participants demonstrated the role of arterial stiffness in coronary heart disease and stroke (Mattace-Raso 2006). Further to general population studies, arterial stiffness has been linked to vascular morbidity and mortality in

cohorts with hypertension (Niiranen et al. 2016; Boutouyrie et al. 2002), end-stage renal disease (Blacher et al. 2003), and type 2 diabetes mellitus (Cruickshank et al. 2002).

The arterial system has two major functions: the conduit function to supply blood to all tissues of the body, and the Windkessel function to dampen high pressure flow from the heart for delivery to the peripheral arterioles. This cushioning role has been realized by the structure of the arterial wall. The arterial wall is composed of three layers. The innermost layer, tunica intima also called tunica interna, is a squamous epithelium with elastic fibers. Tunica media, the middle layer, consists of muscle cells which help regulate the pressure. Tunica externa, the outmost layer, anchors the artery to the surrounding tissue. There are two types of arteries in the circulatory system, elastic and muscular arteries. Elastic arteries are located closer to the heart with a greater amount of elastin and collagen in their tunica media. These elastic arteries have the capacity to receive blood during systole and then eject it to the smaller downstream arteries in diastole. This way, they contribute to a consistent flow despite oscillatory pressure during the cardiac cycle. Muscular arteries, on the other hand, are involved in distribution and as such are lined with smoother muscles in their tunica media (**Figure 2.1**). This feature allows them to regulate blood flow in different tissues and modulate the velocity of the pressure wave which is critical to the blood flow considering wave reflection in the arteries. The reflected waves are important as they may impose additional load on the heart (Shirwany et al. 2010).

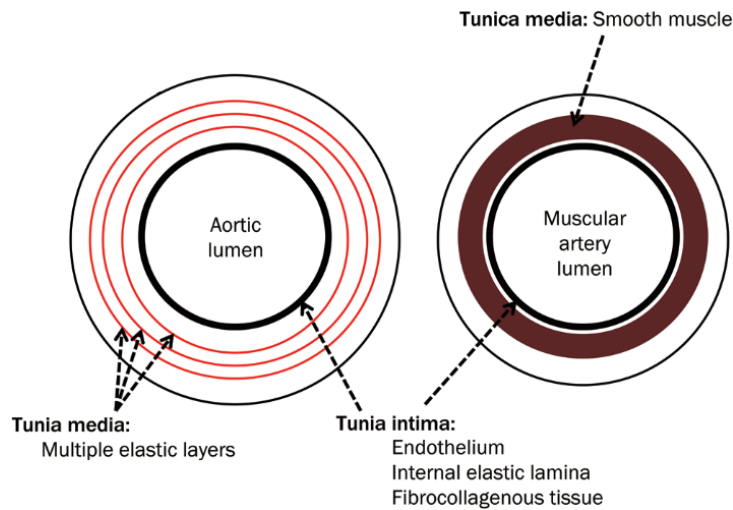


Figure 2.1. Elastic versus muscular artery (modified from (Shirwany et al. 2010))

In brief, elasticity of the arteries enables them to expand and recoil during systole and diastole. This feature helps in moving the blood flow in diastole as well as maintaining a relatively constant pressure in the arteries. The major consequence of increased arterial stiffness is impaired damping function which is followed by increased systolic blood pressure (SBP) and decreased diastolic blood pressure (DBP) and as a result, widened pulse pressure (PP; defined as the difference between SBP and DBP). This condition known as isolated systolic hypertension is a prevalent correlate of age-related arterial stiffening. The complications associated with arterial stiffness elucidate its key role in the pathogenesis and risk prediction of CVD.

2.2 Mechanisms of arterial stiffness

The pathophysiology of arterial stiffness is a consequence of a combination of structural and functional mechanisms following pathogenic cellular and molecular changes and different facets of the intricate process are not yet completely understood. This section presents several important mechanisms involved in arterial stiffening which are more relevant to the scope of the current research.

2.2.1 Structural changes

Compositional changes

The elasticity of the arterial wall is primarily determined by its composition. Collagen and elastin are the two core components of the vessel wall. The synthesis and degradation of each of these two proteins are closely dependent upon one another (Chen et al. 2017). Aging affects this regulatory equilibrium when overproduction of collagen undermines elastin generation leading to gradual replacement of elastin with collagen and consequently stiffening of the arterial wall (Shirwany et al. 2010). Vessel size is another determinant of arterial stiffness. Smaller arteries are generally stiffer than larger arteries (Steppan et al. 2011). This can also be explained by the composition of arterial wall.

2.2.2 Functional changes

Blood pressure

Arterial stiffness seems to be both a cause and a consequence of high BP. BP is a key mediator of arterial compliance. The elasticity of the arterial wall is not constant, but it is pressure-dependent (Wiinberg 2000). Arterial stiffness increases with pressure due to increased collagen recruitment (Steppan et al. 2011). While at lower pressure levels, elastin fibers support the wall stress, at higher levels of pressure, wall stress is supported by collagen fibers (Palombo et al. 2016). Again, elevated systolic or PP due to either hypertension or aging leads to wall structure remodeling by elastin breakdown which in turn results in arterial stiffening (Laurent et al. 2015). Beyond that, a study on hypertensive young adults (Harvey et al. 2015) suggested elevated BP is the main contributor to arterial stiffness early in life. On the other hand, epidemiological studies indicated that aortic stiffness precedes and predicts incident hypertension (Mitchell et al. 2010; Fleenor et al. 2015). The pressure dependence of arterial stiffness also implies that the mean arterial pressure must be reported along with arterial stiffness measurements. The effect of BP alterations on PWV in retinal arteries as a

measure of retinal artery stiffness has been particularly investigated in Chapter 5 of this thesis.

Impaired smooth muscle function

In addition to the extracellular proteins i.e. collagen and elastin which support the mechanical load, vascular smooth muscle cells play a functional role in arterial stiffness by regulating vasodilation and vasoconstriction (Montero et al. 2015). Smooth muscle function is controlled by the vascular endothelium through vasoactive factors and receptor-mediated signaling (Fleenor et al. 2015). The increased proliferation and migration of smooth muscle cells lead to hypertension and can potentiate arterial stiffening. Aging contributes to vascular smooth muscle dysfunction (Montero et al. 2015) and it has been estimated that almost fifty percent of age-related aortic stiffness is associated with either signaling or structural changes in smooth muscle cells (Fleenor et al. 2015). The role of smooth muscle cells in blood pressure regulation has been specifically targeted by intravenous phenylephrine injection in order to raise BP through vasoconstriction in Chapter 5.

2.2.3 Signaling Mechanisms

Nitric Oxide (NO)

Nitric oxide (NO) is a primary signaling molecule released by vascular endothelium to regulate vasoconstriction and affects both arterial function and structure. Reactive oxygen species (ROS) refers to radical and non-radical oxygen species which are intrinsic by-products of oxygen metabolism. Abnormal increased levels of ROS which may occur under environmental stress and with advancing age is known as oxidative stress and results in reduced NO bioavailability and impaired dilating capacity, and endothelial dysfunction (Fleenor et al. 2015). Temporal NO boosting intervention has been utilized in Chapter 5 in order to induce vasodilation and reduce BP.

Arterial stiffness is also attributable to endothelial dysfunction, neuroendocrine signaling, and genetics (Zieman et al. 2005; Shirwany et al. 2010). The effect of matrix metalloproteases (Payne et al. 2010), non-enzymatic glycation (in type 2 diabetes), insulin resistance and high insulin concentrations (Sethi et al. 2014), glucose, salt intake, and diet (Shirwany et al. 2010) on arterial stiffness has also been discussed in prior studies which are beyond the scope of this chapter.

2.3 Indices of arterial stiffness

Several noninvasive techniques have been developed to quantify arterial (central/aortic or peripheral) stiffness *in-vivo*. Amplitude of pressure wave, compliance index, augmentation index, and PWV are the most commonly used clinical markers of arterial stiffness (Riggio et al. 2010; Shirwany et al. 2010).

With every heartbeat, when the heart is in systole, the elastic fibers in the wall of arteries distend to accommodate an increased volume of blood. Then, they recoil during diastole. These dilation and constriction produce a pulsatile pressure wave in the arteries travelling from the heart to the microcirculation. The arterial pressure waveform reflects pressure changes during the cardiac cycle. The arterial pressure pulse is composed of a forward-travelling component induced by ventricular ejection. As this wave propagates in the arterial tree, the inherent resistance due to tapering, or branching, and changes in wall properties and size of the downstream arteries forms a backward wave travelling toward the heart at the end of systole and early diastole. This reflected wave, by virtue of its timing favorably augments both systolic and PP of the arterial pulse as it travels distal to the heart (Nichols 2005). The shape of the pressure pulse varies due to arterial structure, position of the measurement site in the arterial tree, and its distance from reflection sites (where impedance changes) which determines the temporal characteristics of the reflected wave (Steppan et al. 2011). The

amplitude and waveform of the pressure pulse are explicable based on the phase shift between the incident and reflected waves. Analysis of this pressure pulse reveals information about arterial stiffness.

First, the speed at which the pressure pulse propagates along the arterial tree, conventionally named *pulse wave velocity* (PWV), is a measure of arterial stiffness. The pressure wave travels faster in stiffer arteries. PWV measured between the carotid and the femoral arteries is the gold-standard non-invasive measure of arterial stiffness (Willum Hansen 2006) and part of clinical investigation of cardiovascular risk.

Increased PWV promotes earlier arrival of the reflected wave during systole which results in an amplified augmentation in systolic peak and consequently wider PP. The *amplitude of the pressure pulse* can also represent arterial stiffness (Safar 2003). The effect of reduced distensibility on the pressure wave has been schematically demonstrated in Figure 2.2.

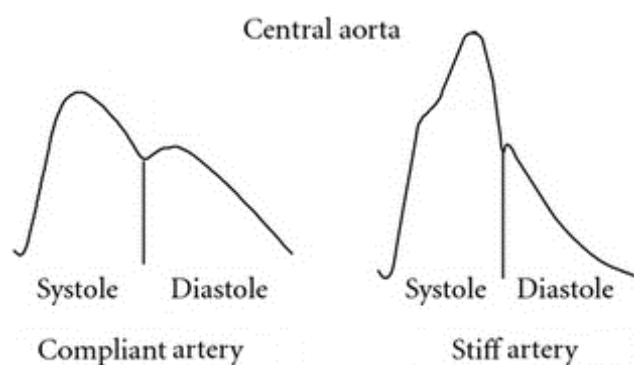


Figure 2.2. Compliant vs Stiff artery. The pressure wave is a superposition of a forward traveling wave induced by ventricle ejection and a backward traveling reflected wave created by impedance mismatch. As stiffness increases, the reflected wave arrives earlier and amplifies the systolic pressure. (modified from (Steppan et al. 2011))

Augmentation index is associated with wave reflection and enhanced central aortic pressure which can indirectly be used to assess arterial stiffness (Weber et al. 2004; Hughes et al. 2013). It is calculated by subtracting the first and the second systolic peak and dividing by PP (Figure 2.3).

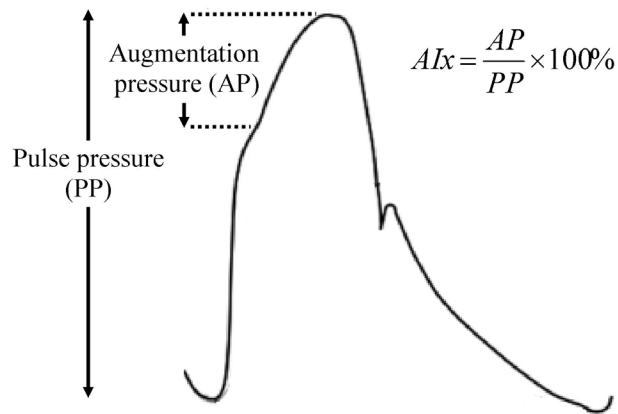


Figure 2.3. Augmentation index

Another quantitative measure of arterial stiffness is *compliance index*. Compliance is classically defined as the ratio of volume change to the changes in inducing transmural pressure. Since vessel axial movement is negligible compared to diameter changes, cross-sectional compliance defined as the ratio of arterial cross-sectional area changes to pressure variations is conventionally used in clinical practice (Tozzi et al. 2000).

As mentioned above, as the pressure wave travels distally, the cumulative reflections due to impedance mismatch along the arterial tree generates a returning waveform toward the heart. The first shoulder of the pressure waveform corresponds to the arrival of this reflected wave. The superposition of the two forward and backward (incident and reflected) waves creates an augmented peak beyond the first shoulder. The closure of the aortic valve results in a small transient increase in the pressure representing as the second shoulder in the pressure pulse wave. This peak rises gradually with age to merge with the first peak. However, in the radial pulse, the expansion will not reach the initial peak. It is worth noting that since reflection sites are closer in peripheral arteries, the amplitude of the pressure pulse is greater in these arteries. Arterial stiffness occurring due to aging, hypertension or diabetes, amplifies central pulse pressure to almost equal to peripheral pulse (Steppan et al. 2011).

2.4 Measurement of pulse wave velocity in large arteries

Elevated PWV as a measure of arterial stiffness predicts the risk of cardiovascular mortality, coronary heart disease and stroke as evidenced by the Health ABC study on 2,488 generally healthy older adults (Sutton-Tyrrell 2005). The prognostic value of PWV was demonstrated in the MONICA study over 1,678 adults, aged between 40 and 70 years, from a Danish population showing its significance above and beyond other cardiovascular risk factors in relation to incidence of fatal and nonfatal cardiovascular and coronary heart disease (Willum Hansen 2006). A meta-analysis of prospective observational data from 17,635 subjects showed PWV improves CVD risk stratification (Wang et al. 2013). A systematic meta-analysis on 15,877 patients from 17 longitudinal studies concluded that there is an even stronger correlation between PWV and future CVD events in high-risk subjects (with hypertension, diabetes, renal or coronary artery diseases) compared with normal subjects (Vlachopoulos et al. 2010).

PWV is a measure of the speed of propagation of the pulse wave along the arterial tree, and it is faster in stiffer arteries. It is calculated by dividing the distance between two sites along the arterial tree by the time taken for a pressure pulse to travel between them. Carotid and femoral arteries are the two most common arteries for PWV calculation. In addition to accessibility and ease of measurement, these arteries represent highest age-related stiffening (Cecelja et al. 2012). Furthermore, the distance between these arteries is comparable to the length of aorta, hence the obtained value represents a more accurate estimate of the aortic stiffness (Shirwany et al. 2010). Pressure pulse propagates in human arteries at a speed of several meters per second (increases from 4 m/s in highly elastic aorta to 10 m/s in smaller peripheral arteries) (McDonald 1968).

The arterial pulse wave can be sensed using cuff-based pressure transducers, tonometry, and doppler ultrasound. Carotid and femoral pulses are conventionally measured using a tonometer and an inflatable pneumatic cuff. The distance can be measured directly from the carotid artery to the top edge of the femoral cuff over the body surface or by subtracting the distance between the carotid artery and the sterna notch from the distance between the sternal notch and the top of the femoral cuff (**Figure 2.4**). The transit time can be measured either by calculating the time delay between the two pulses or by finding the arrival time of each pulse with reference to the R-wave of the electrocardiogram (ECG).

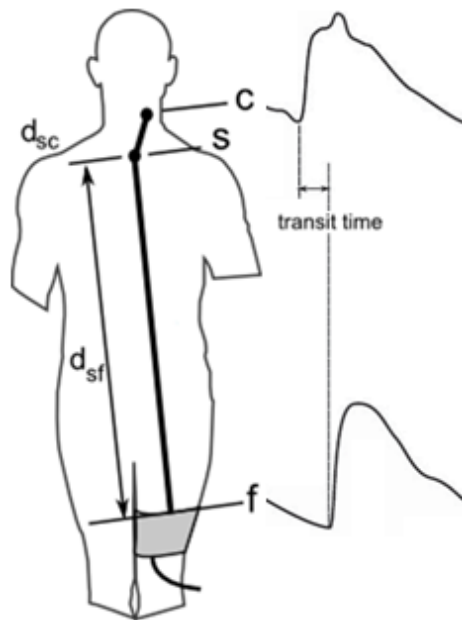


Figure 2.4. Central PWV measured between carotid and femoral arteries as $PWV = \frac{d_{sf}-d_{sc}}{\text{transit time}}$ (modified from (Butlin et al. 2017))

The Moens-Korteweg equation (Vlachopoulos et al. 2011) relates PWV to stiffness (E) with dependency on vessel wall thickness (h), vessel radius (r), and density of blood ($\rho = 1050$ kg/m³):

$$PWV = \sqrt{\frac{Eh}{2r\rho}}$$

Equation 2-1

In this formula, E known as the Young's modulus, modulus of elasticity, elastic modulus or tensile modulus is a measure of stiffness of an isotropic sample of a material. It is defined as the gradient of changes in stress with strain (for small strains). In practice, it can be quantified as the slope of the linear portion of the stress-strain curve obtained from tensile testing.

2.5 Arterial stiffness in the microcirculation

Microcirculation refers to the distal part of the circulatory system composed of arterioles, capillaries and venules with diameter less than 150 μm in the human. It is a dense network distributed throughout all organs with a pivotal role in oxygen and nutrients delivery and metabolic waste removal.

There is increasing recognition that the interrelations between arterial stiffness and cardiovascular events are mediated by microvascular remodelling and obliteration (Cooper et al. 2016; Safar et al. 2018). Human and animal studies have evidenced arteriolar remodelling and capillary rarefaction in early stages of hypertension (Struijker-Boudier et al. 2012). The possibility that the microcirculatory impairment may occur early in the onset of arterial stiffness or may promote large artery stiffness underlines the importance of monitoring microcirculation for more effective preventive and therapeutic measures (Lim et al. 2013).

The elasticity of large arteries allows them to store a portion of the blood during systole and eject it during diastole. This capacitance or damping function known as Windkessel effect provides steady flow in the microvasculature despite notable pressure fluctuations during the cardiac cycle. Reduced distensibility impairs the ability of the arterial tree to cushion the pressure change. As a result, undamped pulsatile flow and excessive pressure in the microvasculature especially low resistance capillaries form shearing forces and can cause irreversible damage. The consequences will be particularly significant in richly perfused

organs like brain and kidney with high flow demand and vulnerable microcirculation. According to the law of Laplace for a thin wall tube (Mayet et al. 2003), increased pressure exerts increased load and tension on the arterial wall:

$$T = P \times r \quad \text{Equation 2-2}$$

$$\sigma = \frac{T}{h} \quad \text{Equation 2-3}$$

where T is tension, P is pressure, r is lumen radius, and σ is stress defined as the force divided by the effective cross-sectional area over which the force acts, and h is wall thickness.

The arterial tree adapts its structure to support the extra load imposed by increased wall stress. Wall thickening and loss in luminal diameter are two compensatory remodelling mechanisms prompted by chronic elevated pressure. Extra wall stress can be supported by either or both processes (Mayet et al. 2003). Park and Schiffrin (Park et al. 2001) suggested that reduced lumen diameter is the most common and maybe the first alteration in microvascular level in hypertension. It can be caused by either inward eutrophic or hypertrophic remodelling (Figure 2.5). Reduction in capillary density (Rizzoni et al. 2018) and vasodilator reserve (mostly in coronary arteries) (Mayet et al. 2003) have also been observed in hypertension.

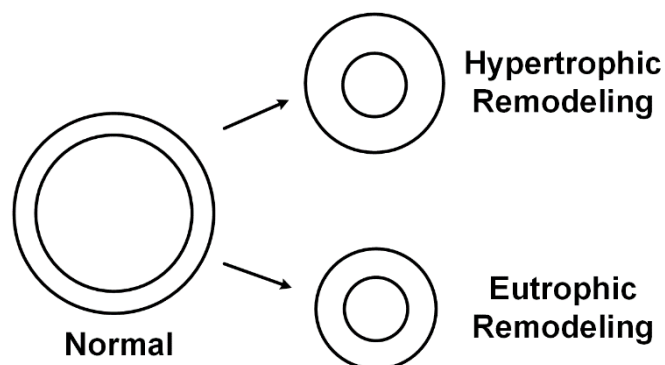


Figure 2.5. Inward remodeling patterns in microvasculature

2.5.1 Microcirculatory imaging techniques

Large artery hemodynamics can be assessed using standard, magneto resonance, or X-ray cine angiography, Doppler Ultrasound (DUS), Laser Doppler Velocimetry (LDV), Particle Imaging Velocimetry (PIV), Magnetic Resonance Imaging (MRI), and Positron Emission Tomography (PET) (Steinman et al. 2005). However, *in-vivo* assessment of the microcirculation is challenging. Perfusion, defined as the volume of blood per unit time (blood flow) per unit tissue mass is a measure of flow in the capillary. There are both invasive and non-invasive methods for the assessment of perfusion. These techniques can be further divided into thermal and imaging methods. Thermal Diffusion Probe (TDP) is an invasive perfusion probing method which requires insertion of a thermal probe into the tissue. In addition to the disturbance caused by the probe, there is a risk of infection in this method.

There are several techniques specifically developed for imaging of the microcirculation. Video-microscopic techniques such as Orthogonal Polarization Spectral (OPS) imaging (Cerný et al. 2007), Sidestream Dark-Field (SDF) (Goedhart et al. 2007), and Incident Dark-Field (IDF) imaging (Hutchings et al. 2016) provide information about vessel diameter, capillary density, flow dynamics and red blood cells velocity. Long processing time, sensitivity to motion, and pressure disturbance induced to the tissue are some of the drawbacks of these methods. Contactless methods including Laser Doppler Flowmetry (LDF) (Abularrage et al. 2005), Laser Speckle Contrast Analysis (LASCA) (Boas et al. 2010), Diffuse Laser Doppler Velocimetry (DLDV) (Snabre et al. 2001) on the other hand, do not affect the tissue directly but are more affected by motion artefacts. Eriksson *et al.* (Eriksson et al. 2014) have outlined the advantages and disadvantages of microcirculation imaging techniques. The properties of the tissue and depth of measurement have to be considered when selecting an appropriate technique for a specific organ. Capillaroscopy (Cutolo et al. 2005), Optical Doppler tomography (ODT) (Haindl et al. 2016) and colour Doppler Optical

Coherence Tomography (CD OCT) (Yazdanfar et al. 2000) allow qualitative and quantitative assessment of the microcirculation in small vessels ($> 50 \mu\text{m}$). More recently, techniques such as laser-scanning confocal microscopy, and Doppler Swept Source OCT (SS OCT) have emerged for imaging red blood cells in vessels (Meglinski et al. 2010).

2.6 The Retina as a window to the microcirculation

The eye fundus has been traditionally used for identification of vascular changes. The advent of emerging ophthalmic imaging techniques in recent years has been translated into a more advanced investigation of disease phenotype through the eyes. The microcirculation can be directly and noninvasively monitored and imaged via the retina.

The human eye is composed of three layers. The fibrous tunic, the outer layer consisting of cornea and sclera serves as a protective layer. The sclera is the white portion of the eye while the cornea is a transparent structure that provides the main refractive power of the eye and forms the anterior chamber in front of the iris and its central opening – the pupil. The iris controls the amount of light entering the eye via the pupil. The intermediate layer of the eye is called the uveal tract and includes iris and ciliary body anteriorly and the choroid posteriorly. The ciliary body connects the choroid to the iris. It produces the aqueous humor which circulates in the eye maintaining pressure and thus shape of the eye as well as providing nutrients for avascular structures. The ciliary body includes the ciliary muscle which alters the lens shape via tension on the lens zonules to help form a focused image of the visual scene on the retina. The inner layer of the eye in the posterior section is the retina, the neural layer, which contains rod and cone photoreceptors, bipolar cells and ganglion cells, as well as several other interneurons and support cells (Willoughby et al. 2010). **Figure 2.6** shows a cross-sectional view of the human eye.

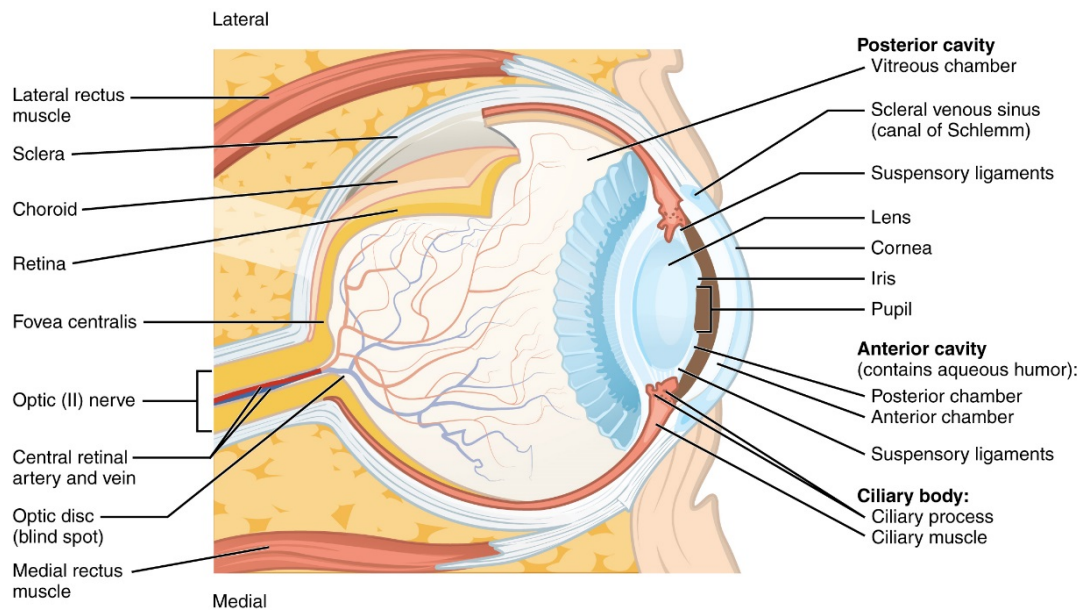


Figure 2.6. Schematic structure of the human eye (reprint from https://commons.wikimedia.org/wiki/File:1413_Structure_of_the_Eye.jpg with permission under creative commons)

The retina is the light sensitive part of the eye where an image of the perceived scene is formed. In the center of the retina the cones are more densely concentrated at the macula, which is responsible for central vision allowing us to read or recognize details. On the nasal side of the macula the optic nerve and major blood vessels enter the eye at the optic disc (so called because of its appearance as a flat yellow circle when viewed with a direct ophthalmoscope). It is also the point where ganglion cell axons leave the eye and as there are no photosensitive cells overlying the optic disc, it produces the physiological blind spot.

The retina comprises 10 layers of cells namely the internal limiting membrane (ILM), nerve fiber layer (NFL), ganglion cell layer (GCL), inner plexiform layer (IPL), inner nuclear layer (INL), outer plexiform layer (OPL), outer nuclear layer (ONL), external limiting membrane (ELM), rod and cone inner and outer segments (IS/OS), and retinal pigment epithelium (RPE) proceeding from the vitreous to the choroid (Willoughby et al. 2010). Several cell layers of the retina are schematically depicted in Figure 2.7.

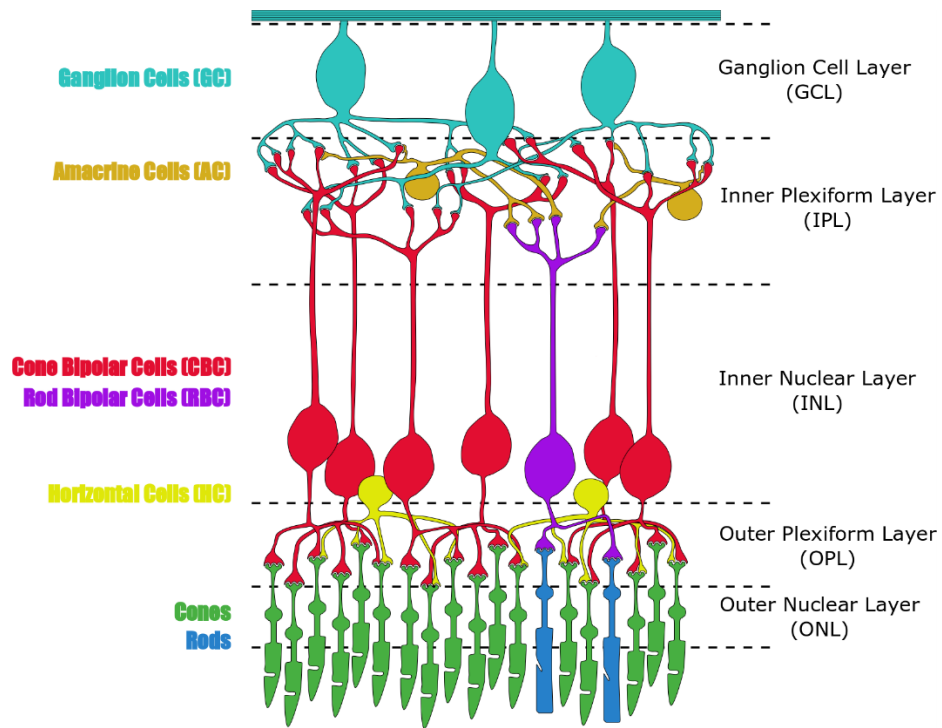


Figure 2.7. Cell layers of the human retina (reprint from https://commons.wikimedia.org/wiki/File:Rods_Cones_Synapse.svg with permission under creative commons)

Since the cornea and lens in the anterior segment of the eye are transparent and avascular, and the vitreous in the posterior segment also, retinal circulation can be easily and non-invasively visualized and imaged. The retina has a rich vascular network which shares the same embryological origin and common histological, anatomical, and physiological characteristics with the heart and brain (Rizzoni et al. 2018). Moreover, retinal vessels and cardiovascular are impacted by the same intrinsic and environmental factors (Flammer et al. 2013). Therefore, retinal vascular changes are clinically highly relevant to cardio- and cerebrovascular pathologies. These advantageous characteristics make the retina an ideal window to study not only ocular but also vascular related pathogenesis. Prior studies have provided strong evidence for retinal vascular changes in association with different types of disease including stroke (Wong et al. 2013), dementia (Heringa et al. 2013), Alzheimer disease (Cheung et al. 2014), hypertension (Ding et al. 2014), aortic stiffness (De Silva et al. 2012), diabetes (Lim et al. 2014), glaucoma (Chan et al. 2017), and sleep apnea (Tong et al. 2017). In particular, retinal arteriolar narrowing, widening of retinal veins, and arteriovenous

nipping are hypertensive retinopathy signs which have been evidenced to correlate with cardiovascular events (Wong et al. 2005; J. Wang et al. 2007; Flammer et al. 2013).

2.6.1 Retinal circulation

The ophthalmic artery, a branch of the carotid artery, is located close to the optic nerve and is the main blood supply of the eye. The eye has a dual blood circulation system with a retinal and choroidal circulation. Although both vascular systems are branches of the ophthalmic artery, they are functionally and morphologically different (Pournaras et al. 2008). While retinal blood flow is low, the choroid is highly perfused. The outer retina receives the main part of the flow (65-85%) through choroidal vessels while the inner and mid retinal layers are fed by the central retinal artery (a branch of the ophthalmic artery which travels inside the optic nerve to the retina). In this study, retinal vessels refer to retinal arteries and veins branching from the central retinal artery at the optic disc and branching to supply the peripheral retina. The choroidal vessels cannot be directly visualised as they are beneath the RPE but can be seen with fluorescein or indocyanine angiography.

Ocular perfusion and retinal blood flow are essential in normal retinal function and performance. Flow (F) is the volume of a fluid passing through a given cross-sectional area per unit of time (blood flow is often expressed in the units of ml/min). Retinal blood flow is regulated through perfusion pressure driving blood into the retinal vascular system and vascular resistance determined by blood viscosity. The average blood flow rate for the entire retina has been reported between 30-80 μ l/min in the human (Dorner et al. 2002; Choi et al. 2012) and between 2-12 μ l/min in the rat (Liu et al. 2015; Kornfield et al. 2015). The measurement technique has a significant effect on the blood flow. Anesthesia in rats also impact the measurements (Moult et al. 2017).

Velocity (V) is the distance an object moves per unit time. Blood flow in a vessel is related to the mean blood velocity (V) by the following equation:

$$F = V \cdot A \quad \text{Equation 2-4}$$

where A is cross-sectional area of the vessel (πr^2 for circular cross-section with radius r). Therefore, the relationship between flow and velocity can be expressed as:

$$F \propto V \cdot r^2 \quad \text{Equation 2-5}$$

This relation indicates that at a constant vessel radius, flow is proportionate to velocity, and vice versa; and at constant flow, velocity is inversely proportional to the radius squared ($V \propto 1/r^2$).

The average retinal arterial outer diameter in human is 50-200 μm (Patton et al. 2005). It has been shown that mean retinal arteriolar diameter decreases by 2.1 μm for each decade increase in age, and by 4.4 μm for each 10 mmHg increase in mean arterial blood pressure (Wong et al. 2003). The equivalent diameter is 110-180 μm for retinal veins. Mean luminal arterial and venous diameter are 95 μm and 130 μm respectively (Rim et al. 2016). Mean wall thickness, calculated from outer and inner vessel diameter, is 20 μm (range: 10 – 25 μm) in arteries and 15 μm in veins (Rim et al. 2016). Studies have shown that age does not significantly change mean venular outer and inner and mean arterial luminal diameters. However, arterial outer diameter and wall thickness increase with age (Muraoka et al. 2013). Retinal capillaries are 5-6 μm in diameter.

The reported blood flow velocity in the human retinal arteries with a diameter between 40 and 130 μm ranges from 4 to 35 mm/s in healthy subjects (Landa et al. 2012; Pournaras et al. 2013; Seidel et al. 2016). Kornfield & Keornfield (Kornfield et al. 2015) measured blood flow

velocity profile across the width of vessels in the rat retina and as expected, the velocity is maximal at the centre. The reported blood flow velocity values in the rat eye range between 10-40 mm/s based on the vessel size and the technique (Zhi et al. 2011; Choi et al. 2012; Kornfield et al. 2015). In normal volunteers, mean arterial blood plasma velocity (MVD) in retinal arterioles with a diameter between 70 and 160 μm has been reported between 6.4 to 7.4 mm/s (Pournaras et al. 2008). Retinal arterial blood velocity during peak systolic arterial blood pressure is around 6 to 20 cm/s in healthy subjects. This is between 1.7 to 10 cm/s for end diastolic arterial pressure (Pournaras et al. 2008). Retinal blood flow can be derived from the centreline velocity of the red blood cells (vRBC) measured using bidirectional laser doppler velocimetry. vRBC increases linearly with diameter. In arteries with diameter between 40 and 130 μm , vRBC is between 7 and 35 mm/s. It ranges between 5 to 25 mm/s for veins with a diameter between 60 to 180 μm (Pournaras et al. 2008). There is no a gold standard technique for retinal flowmetry in humans or animals.

2.6.2 Ocular imaging modalities

The transparency of the anterior segment and vitreous of the eye, with direct access and low light scattering as unique features of the eye makes ophthalmic imaging much more readily accessible and achievable compared with imaging other organs. In recent years, new imaging techniques have revolutionized the visualization and investigation of ocular status, vasculature, and hemodynamics. Most common causes of blindness or irreversible visual loss relate to the pathologies in the posterior part of the eye. Retinal imaging is important not only in screening and diagnosis but also in the monitoring of disease progression and treatment response assessment – for example in glaucoma (Chan et al. 2017), macular degeneration or diabetic retinopathy (Sabanayagam et al. 2015). While Fluorescein Angiography (FA) has been available for many years to visualize the retinal circulation in real time, recent advanced retinal imaging tools such as Optical Coherence Tomography (OCT), the Dynamic Vessel

Analyzer (DVA), Adaptive Optics (AO), and Doppler and Swept-Source OCT have enabled quantitative and reproducible assessment of retinal vascular characteristics. This section briefly covers the recent advancements in fundus and ophthalmic imaging.

Fluorescein Angiography

Fluorescein angiography (FA) is the gold standard in imaging and evaluation of capillary bed (Chan et al. 2017). The technique is invasive as it demands intravenous injection of fluorescein dye (sodium fluorescein or indocyanine green). Emission of photons from the fluorescein dye illuminated with blue light at a wavelength of 490 nm while circulating through capillaries forms grayscale images indicating capillary network. The clinical utility of FA is limited because it is invasive, time-consuming and confounded by superimposition of capillaries from different retinal layers (Chan et al. 2017).

Scanning Laser Ophthalmoscopy

Scanning Laser Ophthalmoscopy (SLO) is a technique based on confocal laser microscopy in which a laser beam scans the fundus and reflected light forms the output. SLO allows estimation of retinal blood flow velocity by means of measuring the time injected dye appears at two sites with known distance along an artery (Pournaras et al. 2013). This method can also be used for measuring the velocity of leukocytes by tracking dye-labelled cells.

Optical Coherence Tomography

Optical Coherence Tomography (OCT) is now a routine technique to assess ocular structure and morphology in clinical practice (Ilginis et al. 2014). In the original time domain OCT, a low coherence light beam, usually infrared light, is shone onto the tissue. The cross-correlation between the reflected light and a split of the original light as a reference creates a

reflectivity profile known as A-scan. A two-dimensional cross-sectional tomograph (B-scan) can be constructed by obtaining a series of A-scans along a line.

The more recent advance of spectral domain (or Fourier-domain) OCT has improved the frame rate, resolution and sensitivity of OCT imaging. In spectral OCT the acquired interferometric frequencies are separated spectrally through Fourier transform (Bouma et al. 2009). OCT has rapidly progressed with more recent advances to allow visualisation of vessels and approximation of blood flow. Doppler OCT enables measuring of the retinal blood flow velocity component parallel to the optical beam (Huang et al. 2016). To compute total blood flow, the angle between flow and probe beam (Doppler angle) is required which is unknown. Doppler angle can be estimated using bi-directional OCT (Blatter et al. 2013), or by capturing double concentric scans with different radii simultaneously (Dai et al. 2013). En-face Doppler OCT is another alternative which obviates the need for angle estimation (Srinivasan et al. 2010; Baumann et al. 2011). OCT angiography (OCT-A) has thus evolved to visualize retinal vasculature without need for a contrast media injection, by measuring the difference in OCT signals due to the blood flow.

Using Dye Dilution Technique (DDT), mean circulation time (MCT) which is the time taken for injected dye molecules like fluorescein to travel through a vessel segment can be measured. Once dye passage path is recorded, it is illuminated with light at a wavelength corresponding to the excitation spectrum of the staining agent to calculate MCT.

Adaptive Optics

Adaptive optics is an advanced technique for removing optical aberrations from an imaging system and was developed for astronomical telescopes. It has become commercially available in some fundus imaging systems with enhanced performance and capabilities. It can be combined with OCT, and the aberrations of the reflected light are sensed and corrected. A

stack of 40 fundus images is acquired at a frequency of 10 Hz and the outcome image is the average of the sequence (Koch et al. 2014). The instrument provides spatial resolution of the order of 1 μm (Rizzoni et al. 2018) and can resolve individual cones. It is yet to be adapted to measure retinal blood flow, but its high resolution has great potential.

Dynamic/Retinal Vessel Analyzer

The Dynamic/Retinal Vessel Analyzer (DVA/RVA) allows continuous measurement of the diameter changes of retinal vessels. The system consists of a fundus camera, a video camera, and a computer system with software that tracks ocular movement and maintains a steady image for analysis. Scans are obtained at a frame rate of 25 fps. After user identification of a particular vessel of interest, a built-in algorithm calculates the diameter of the selected vessel based on hemoglobin transmittance profile. One limitation is that opaque optical media, and lack of fixation can affect the measurements considerably. Furthermore, assuming no refractive error, diameters are measured in relative units (RU). Each RU correspond to 1 μm in the Gullstrand's eye. The DVA is the main device used in this project (Figure 2.8).



Figure 2.8. Left: DVA system, right: a representative fundus photo obtained by DVA

2.6.3 Retinal vessels: a proxy for assessment of systemic blood pressure variations

The retina provides an easily accessible window to monitor microcirculation and it mirrors the status of the systemic circulation. Retinal vasculature undergoes pathogenic changes in a range of CVDs including hypertension and arterial stiffness. However, the interrelation between macro- and micro- vasculature changes in systemic vascular diseases are yet to be fully understood.

The retinal vasculature undergoes both functional and structural alterations in response to raised blood pressure. Cheung *et al.* categorized hypertension-related changes in the retinal vasculature into hypertensive retinopathy, vascular caliber changes and retinal vascular geometrical changes (Cheung, Ikram, et al. 2012).

Hypertension-related pathological changes in the retinal vessels are referred to as hypertensive retinopathy (Wong et al. 2004). These changes can occur locally or may involve the whole retinal vasculature. Generally, a higher level of generalized retinal signs is associated with more severe vascular damage. Based on the underpinning pathogenic factors, hypertensive retinopathy signs manifest in four overlapping stages. The initial signs are seen as generalized retinal arteriolar narrowing due to increased vasospasm and vasomotor tone. In the second phase, intimal thickening, hyaline degeneration, and media wall hyperplasia reveal as diffuse and focal arteriolar narrowing, arteriolar wall opacification (known as silver wiring), and arteriovenous crossing changes. In more pronounced levels of hypertension, blood-retinal barrier breakdown leads to blot, dot, or flame-shaped hemorrhage, hard exudates, cotton-wool spots and microaneurysms. Finally, malignant hypertensive retinopathy signs present as optic disc swelling (papilledema) and macular edema in extremely high blood pressure (Wong 2006). Endothelial dysfunction, inflammation, and angiogenesis may also

contribute to the retinal vascular changes in presence of elevated blood pressure (Wong et al. 2007).

Change in retinal vascular caliber, specifically retinal arteriolar narrowing has been well established in large population-based studies (Wong et al. 2007; Ding et al. 2014; Wang et al. 2016). Although retinal venular caliber has not attracted much attention, recent studies suggest that, like arterioles, venules also respond to microcirculation changes dynamically. In fact, having a much thinner vessel wall, venules are supposed to be more responsive to the variations in the systemic circulation compared with arterioles. However, the link remains inconclusive due to conflicting observations. While one study has reported retinal venular dilatation (Ding et al. 2014), another study showed no significant difference in retinal venular caliber in presence of hypertension (Wang et al. 2016). The physiological mechanisms relating retinal venular diameter changes with blood pressure are not fully elucidated as well.

Traditionally, studies investigating retinal vascular abnormalities focused on vascular diameter changes. Emerging imaging technologies have heralded new possibilities for assessment and quantification of more complex geometric features of retinal vessels such as tortuosity, branching angle and fractal dimension. Vascular morphological malformations are speculated to impair the efficacy of the microcirculation and capillary exchange which in turn can lead to serious vascular damage. Retinal vascular optimality score obtained combining fractals and calibre has shown to be associated significantly with higher mean arterial blood pressure (Cheung, Thomas, et al. 2012).

Some of the pathological mechanisms underlying arterial stiffness such as endothelial dysfunction and elastin/collagen remodeling occur in small arteries in parallel with large arteries (Safar et al. 2018). A study in 197 hypertensive patients (Katsi 2012) demonstrated an association between arterial stiffness measured by carotid-femoral PWV (cPWV) and the

severity of hypertensive retinopathy signs graded by Scheie's scale. In subjects with hypertension, deterioration of hypertensive retinopathy signs was coincident with progressive stiffening of the aorta. A similar investigation in a Type 1 diabetes cohort comprising 676 Caucasian patients revealed progression in retinopathy with increased cPWV (Theilade et al. 2013). Another study among 145 patients of Asian descent with ischemic stroke showed retinal arteriolar luminal narrowing and arteriovenous nicking in association with increased cPWV as an indicator of aortic stiffening (De Silva et al. 2012). In a comparative study between 137 early-stage hypertensive and 86 normotensive subjects, a significant inverse association was evidenced between cPWV and central retinal artery equivalent (CRAE) concluding that CRAE is an independent predictor of arterial stiffness as assessed by both cPWV and augmentation index (Triantafyllou et al. 2014). The Nagahama study in 6720 participants with Japanese ethnicity followed longitudinal changes in retinal vessel caliber in parallel with arterial stiffness (Kawashima-Kumagai et al. 2018). Arterial stiffness measured by brachial-to-ankle pulse wave velocity (baPWV) was significantly increased in subjects with narrower CRAE. Central retinal vein equivalent (CRVE) was not changed significantly though.

2.7 Quantifying retinal vascular characteristics

Vessel analysis techniques can be subdivided into two groups. Static methods based on a single still image and dynamic methods based on a sequence of images offering the possibility of the assessment of changes over time. While static methods only reveal morphological information such as diameter, spread, branching and curvature of vessels, using a video sequence the velocity of the wave propagation and pulsatility index can be extracted. It is worth noting that dynamic retinal vessel analysis in the literature often refers to the analysis of the response of the retinal vessels to diffuse luminance flicker light stimulation. The expected response in a healthy subject is dilatation of retinal vessels in response to light

stimulation mediated by NO. Hypertension, endothelial dysfunction and other systemic or ocular aetiologies may alter this flicker response (Cheung, Ikram, et al. 2012). Throughout this document dynamic analysis means the assessment of time-dependent retinal vascular alterations by continuous measurements from a video sequence (rather than the specific flicker response).

Following the recent growth in retinal imaging, several computer platforms have been developed for more accurate and objective quantification of the retinal vascular changes. All these platforms have been established for static analysis. IVAN (Hao 2014) and Optimate both developed at the Department of Ophthalmology and Visual Sciences of University of Wisconsin were designed for vessel diameter measurement (Kirin et al. 2017). VAMPIRE by the Universities of Dundee and Edinburgh (Perez-Rovira et al. 2011) and SIVA from the National University of Singapore (Cheung et al. 2010; Hao 2014) enable quantification of more advanced geometrical and architectural features including tortuosity, branching angle, and fractal dimension. These indices are explained in the following paragraphs.

2.7.1 Static indices

Retinal vascular caliber

CRAE, CRVE (Figure 2.9) and their dimensionless quotient, arteriovenous ratio (AVR) are the three standard indices summarizing retinal vascular calibre. CRAE is measured according to the Parr-Hubbard formula as the diameter of all arterioles coursing through in a concentric ring of 0.5-1 disc diameter surrounding the optic disc. The same formula applies to the veins of the same region for calculating CRVE. Age, hypertension, diabetes mellitus, obesity, lipids and physical activity, atherosclerosis, inflammation and endothelial function, genetics, and birth weight are all factors that can determine retinal vascular caliber (Ikram, Ong, et al.

2013). Retinal vascular caliber has been widely studied in a range of diseases including brain, coronary heart disease (CHD), kidney, and ocular diseases.

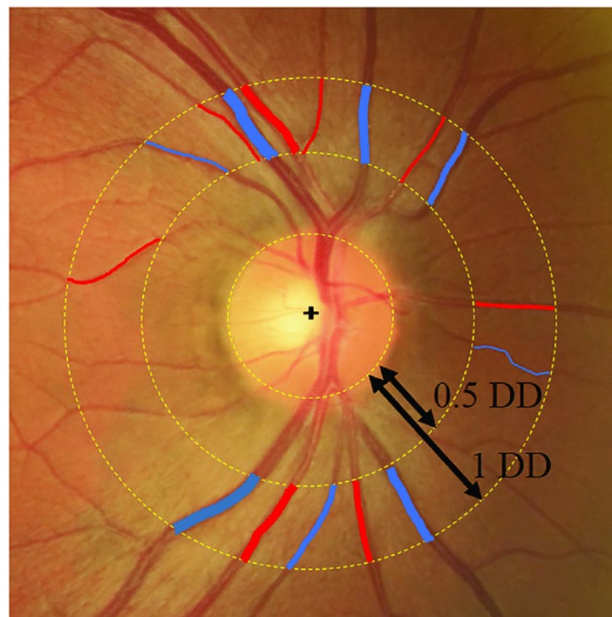


Figure 2.9. Measurement of CRAE and CRVE as the diameter of the retinal arteries (red) and veins (blue) located within an annulus bounded by 0.5 and one disc diameter from the rim of the optic disc (Image taken directly from (Takai et al. 2017))

There is a direct neural connection between the eyes and the brain, as the cerebrospinal fluid is directly contiguous with the optic nerve sheath to the posterior eye. Furthermore, retinal and cerebral vasculatures share the same embryological origin, similar histological, anatomical and physiological features, and vascular regulatory processes. It is therefore no surprise that there is a strong association between stroke-related changes in the cerebrovascular system and retinal vasculature. In the ARIC study of 10,358 participants, smaller retinal AVR was shown to be an indicator of higher risk of stroke (Wong et al. 2001). Retinal venular dilatation is predictive of stroke and cerebral infarction, as reported in the Rotterdam study (Ikram, de Jong, et al. 2006) and in a meta-analysis of 20,798 subjects (McGeechan et al. 2009). Retinal arteriolar caliber, however, does not register any correlation in either case. While venular widening has been observed in association with higher risk of

vascular dementia in Rotterdam study, the link remains inconclusive as it is not supported by vascular etiology of Alzheimer's disease (Ikram, Ong, et al. 2013).

Retinal vascular changes in CHD has been reported more in women than in men (Ikram, Ong, et al. 2013). This can be explained by the fact that in women, the microvasculature (vascular characteristics of microcirculation) contributes more to CHD in comparison with men (McClintic et al. 2010). Increased risk of CHD and acute myocardial infarction was observed in women with reduced AVR in the ARIC study (Wong et al. 2002). A meta-analysis of 22,159 subjects found retinal arteriolar thinning and venular thickening were linked to higher risk of CHD in women but not men (McGeechan et al. 2009). Studies investigating retinal vascular abnormalities in renal diseases suggest common pathogenesis in both retinopathy and nephropathy (Ikram, Ong, et al. 2013). In MESA study of 4,594 adults, reduced retinal arteriolar caliber was associated with a higher risk of chronic kidney disease in white participants (Yau et al. 2011). In a study among 10,890 subjects, reduced retinal arteriolar and venular diameter were observed in people with retinal vein occlusion (Ikram, Ong, et al. 2013). Narrowing of central retinal vein is also common in glaucoma. Studies investigating retinal vascular caliber in age-related macular degeneration (AMD) and open-angle glaucoma reported controversial results though (Ikram, Ong, et al. 2013) with one study reporting retinal venular widening associated with AMD (Jeganathan et al. 2008) while the other has reported no significant difference in retinal venular diameter (Yang et al. 2012).

Vascular tortuosity

Tortuosity is a dimensionless index defined as the ratio of the actual distance between two given points along a vessel to the length of the shortest straight line connecting them. Larger tortuosity reflects greater vascular curvature and twisting of vessels. This can be experimentally determined from the integral of the curvature squares along a vessel segment

(Cheung et al. 2011). A study among a total of 2,915 participants investigating cardiovascular risk factors in retinal vascular tortuosity (Cheung et al. 2011) showed that retinal arteriolar tortuosity decreases with age, body mass index (BMI), elevated BP, and narrower retinal arteriolar caliber. Greater retinal venular tortuosity was reported in the same study in young subjects, subjects with higher blood pressure, higher cholesterol level, wider retinal venular caliber, or lower high-density lipoprotein (HDL). Venular tortuosity has been also shown to correlate negatively with ocular axial length and positively with myocardial health (Kirin et al. 2017).

Vascular bifurcation angle

Bifurcation angle is the angle subtended between two dichotomous off-springs at a vascular junction. History of high cholesterol is shown to be associated with both wider arteriole bifurcation angle and increased smaller-child branching angle (Habib et al. 2014).

Fractal dimension

Fractal dimension also known as Minkowski-Bouligand dimension or Kolmogorov dimension quantifies the complexity of retinal vasculature branching pattern showing how thoroughly it covers the membrane. It is calculated by applying box counting method on the vessel skeleton (Thomas et al. 2014). Age, blood pressure, refractive error, and lens opacity impact retinal vascular fractal dimension (Cheung, Thomas, et al. 2012). Severe diabetes increases retinal vascular fractal dimension (Bernardes et al. 2011). Studies show retinal vascular fractal dimension is also associated with hypertension, chronic kidney disease, stroke, coronary heart disease mortality and leukoencephalopathy (Cheung, Thomas, et al. 2012).

Whereas existing methods in the literature mostly focus on the assessment of retinal vessels in static images, the clinical applicability of retinal static vascular markers remains speculative due to contradictory results in many studies and overlap between disease processes and

characteristic changes. The advent of new ocular video imaging techniques along with emerging advancements in processing power has paved the way for the introduction of dynamic markers of retinal vessels. Dynamic assessment of retinal vessels by reflecting cardiac changes may offer more relevant and specific information on prediction and pathogenesis of cardiovascular-related disorders.

2.7.2 Dynamic indices

Pulsatility

Pulsatility index defined as the ratio of pulse amplitude to mean flow over the cardiac cycle reflects an association with vascular impedance. Investigation of spontaneous retinal venous pulse (SRVP) is useful as it depends on translaminal cribrosa pressure, defined as the pressure gradient between intraocular pressure (IOP) and intracranial pressure (ICP). The clinical utility of this dependency is non-invasive detection of intracranial hypertension, intraocular hypotension or retinal venous occlusion. ICP can be estimated by IOP by lowering IOP to the point that venous pulsations cease. Disappearance of SRVP is also speculated to be associated with progressive glaucoma (Golzan 2012; Morgan et al. 2004). Tong *et al.* reported attenuation of the retinal vascular pulse amplitude is associated with obstructive sleep apnoea progression (Tong et al. 2017).

Retinal pulse wave velocity

As explained earlier in Section 2.2.3 2.4 , the velocity at which pressure waves propagate along the arterial tree is commonly used in the clinical setting to investigate the risk of cardiovascular events. Given that endothelial dysfunction as a major cause of vascular diseases (Lim et al. 2013) impacts mainly smaller arteries at the microvascular level, measurement of PWV in microvasculature may provide a better predictor for early screening of vascular related diseases.

While PWV in large arteries is a long-recognised marker of arterial stiffness, the measurement of PWV in retinal arteries is a new field of research dating back to 2000 when fluorescein angiography was used to measure retinal PWV (rPWV) for the first time (Otto 2000; This study was performed in form of a PhD dissertation in German language). The values of rPWV obtained using this method were between 24 and 174 mm/s in healthy adults and between 32 and 300 mm/s in hypertensive subjects (Spahr et al. 2017).

A further study on rPWV was published 11 years later (Kotliar et al. 2011). Retinal pulsations were detected at two points with a known distance along an artery by measuring diameter changes in a normal cohort using DVA. Signals were filtered using band-pass filters in two steps. Cross-correlation was then used to compute the time delay between the two signals. The median rPWV of 21.5 mm/s in young subjects and 243.8 mm/s in the elderly showed significant age-dependency of rPWV relatively similar to what had been previously observed in large arteries (Kelly et al. 1989). Given that the pressure pulse travels from the heart to the ophthalmic artery at a speed of 4 m/s in a healthy human, their results were 200 times slower than PWV in large arteries.

In 2013 Kotliar *et al.* (Kotliar et al. 2013) further investigated the pressure dependency of pulse wave velocity in human retinal arteries. However, the results were a factor of 50 slower than what they had reported previously. This time, they reported average rPWV of 442 ± 148 RU/s in normotensives accelerating to 786 ± 486 RU/s in subjects with high-normal blood pressure and 1243 ± 694 RU/s in mildly hypertensive patients (RU correspond to 1 μ m in emmetropic eyes). They compared three different methods to find the time delay between proximal and distal signals. In the first method, the time delay was computed from the phase delay between the sinusoidal components of the two diameter waveforms at the heart rate frequency. As an alternative, the phase delay of higher harmonics (9th and 10th harmonics) of

the heart rate was also calculated. Finally, time delay was determined as the slope of the regression line of distance on phase shift obtained from higher harmonics of the heart rate. rPWV measurements from higher multiples of the heart rate showed strong association with brachial and central systolic blood pressure.

In the next study published in 2014, Golzan *et al.* measured the amplitude of the arterial and venous pulses and arterial rPWV in two strains of rats, Wistar-Kyoto (WKY) and Sprague–Dawley (SD) (Golzan, Butlin, et al. 2014). Retinal recordings were captured using a high-speed camera (250 fps) mounted on a fundus camera. They used the same software as the one employed by Kotliar *et al.* provided by Imedos (Jena, Germany) to extract retinal diameter changes. Signals were low-pass filtered with a cut-off frequency at the cardiac frequency (almost 5 Hz). The heart rate was calculated from the simultaneous ECG. The time shift between proximal and distal signals was calculated using the foot-to-foot method at a fiducial point at 20% of the signal amplitude. The average rPWV was 11.4 and 9.8 cm/s in WKY and SD rats respectively. The rPWV was not significantly different between the two groups of rats. The average arterial and venous pulse amplitude were 7.9 and 9.0 μm in WKYs and 5.4 and 6.2 μm in SDs. The average venous diameter was significantly larger than arterial diameter in both animals. However, the venous and arterial average pulse amplitude did not register any significant difference in either group. They also reported a positive correlation between rPWV and HR. Both arterial and venous pulse amplitude were positively correlated with the vessel size in both strains.

In 2015, Spahr *et al.* challenged prior studies stating that the devices used by the previous studies did not meet the requirements of rPWV measurement in terms of temporal and spatial resolution and signal-to-noise ratio (SNR). They proposed a novel technique using full-field swept-source OCT to measure retinal pulses from the motion induced in the tissue

surrounding retinal vessels by vessel contraction and expansion (Spahr et al. 2015). The high spatial and temporal resolution of the OCT machine they developed (10 nm and 0.5 ms respectively) enabled obtaining the shape of the retinal pulses. Using the foot-to-foot method to quantify temporal delays, they reported a speed of 600 mm/s in retinal arteries which was much closer to the PWV expected from measurements outside the retina and from Moens-Korteweg equation.

Song and colleagues (Song et al. 2016) proposed their ultra-high-speed imaging technique based on swept-source OCT to record retinal pulsations in the mouse eye with a rate of 16 kHz and spatial sensitivity of 20 nm. Their measurements showed pulse wave propagation at a speed of more than 1 m/s in the mouse retina.

In 2017, another group reported an rPWV of 30 mm/s in a normotensive and 50 mm/s in a pre-hypertensive volunteer (Qian Li et al. 2018). To improve the accuracy of the measurements without increase in the volume imaging rate, they proposed a technique using spectral domain OCT for measuring PWV in retinal arteries. Instead of simultaneous recording at two sites, the transit time was calculated by jump-scanning. In this method, retinal arterial pulsations are recorded separately by repeated OCT B-scans at two points along an artery. This way, rather than volume imaging rate, the accuracy depends on the frame rate which is less costly to increase. However, one limitation of this method is that since the proximal and distal pulses are not measured simultaneously, there is a possibility that rather than tracking a single pulse, pulses are derived from consecutive cardiac cycles. In addition, the method is extremely sensitive to inherent heart rate variations. **Table 2.1** summarises a comparison between the published studies on rPWV.

Table 2.1. Comparison of reported values of rPWV in the literature.

Reference	Reported values	Cohort	Technique
(Otto 2000)	0.024-0.026 m/s	A healthy 30-year-old adult	Fluorescein Angiography
	0.240 m/s	A healthy 63-year-old adult	
	>0.300 m/s	Hypertensive 45-year-old subject	
(Kotliar et al. 2011)	0.022 m/s	10 young adults (median age: 26)	DVA
	0.244 m/s	10 old subjects (median age: 67)	
(Kotliar et al. 2013)	0.0004 m/s	19 young normotensive men	DVA
	0.0008 m/s	27 young pre-hypertensive men	
	0.0012 m/s	19 young hypertensive men	
(Golzan, Orr, et al. 2014)	0.114 m/s	Wistar-Kyoto rats	High speed fundus recording
	0.098 m/s	Sprague–Dawley rats	
(Spahr et al. 2015)	0.6 m/s	A normal young adult	Swept-source OCT
(Song et al. 2016)	>1 m/s	mice	Swept-source OCT
(Qian Li et al. 2018)	0.029-0.031 m/s	A young normotensive adult	Jump-scan Spectral - domain OCT
	0.050 m/s	A young pre-hypertensive adult	

Despite the limited number of studies that have been performed so far, there is a vast discrepancy between the reported values of PWV in retinal arteries. Accordingly, the exact nature of PWV in retinal arteries is yet to be established, and its relationship with vascular function elsewhere.

To investigate whether dynamic characteristic of retinal vessels, particularly, retinal arterial PWV correlates with arterial stiffness, the first challenge was to develop an appropriate methodology to quantify diameter changes from retinal recordings. The following sections provide a brief review on current methods for the segmentation and diameter measurement of retinal vessels in the literature.

2.8 Techniques for retinal vessel segmentation and diameter measurement

The concave shape of the retina results in non-uniform background and foreground illumination in retinal images. In addition to uneven intensity, the variability of vessel width and length, shape, and orientation, the presence of staggered, occluded, branched, crossed and twisted vessels as well as retinal abnormalities like drusen, exudates, microaneurysms and other artefacts pose challenges to the accurate and robust segmentation of retinal vessels and may result in miss-segmentation of the microvessels. Furthermore, the segmentation of retinal vessels is significantly impacted by contrast variations due to varying width of blood vessels, respiratory and eye movements. Strong reflection along the vessel centreline especially in the arteries and in retinal images acquired from young subjects also complicates the segmentation of retinal vessels. Poor illumination due to short exposure time especially in high frame rate videos makes the segmentation task even more complex and challenging. Consequently, despite extensive progress in measurement and evaluation of the characteristics of retinal vessels, as a challenging and problematic topic, it still remains a focus for ongoing research.

2.8.1 Vessel segmentation

Techniques of vessel segmentation can be classified in different (overlapping) ways such as edge- vs region-based, pattern-recognition-based techniques either supervised or unsupervised, integral- vs derivative-based approaches, parametric (including curve fitting and snakes) vs non-parametric models (such as multi-scale methods), kernel-based profile modelling including matched-filtering and edge detections, vessel tracking, and morphological methods. In most cases, a combination of different techniques is applied to achieve a precise segmentation.

Several surveys have reviewed techniques for vessel segmentation specifically in retinal images. Qian *et al.* categorized vessel segmentation methods into two main groups: Integral and derivative based techniques (Qian et al. 2009). Integral based methods including matched filters and model-based methods are among the most frequently-used vessel segmentation techniques which are particularly efficient in finding the skeleton of the vascular tree. However, these methods do not provide accurate measurement of the vessel diameter. On the other hand, derivative-based methods such as Hessian-based operators as a popular example in this category rely on the assumption that the vessel is single oriented. Consequently, they cannot properly segment highly tortuous vessels or vessel crossing and branching which are very common in retinal images.

In a recent review by Almotiri *et al.* (Almotiri et al. 2018), means of retinal vessel segmentation has been divided into seven main categories including kernel-based, vessel tracking/tracing, mathematical morphological processing, adaptive local thresholding, multi-scale, model-based, and pattern recognition methods which have been briefly explained in the following paragraphs.

Kernel-based techniques also known as matched filtering are among the most popular vessel segmentation methods which model a feature of the vessels under consideration to create two dimensional kernels for detecting the vessels in the images. The presence of the vessel is then examined by the response to the matched filter kernel. The algorithm typically is followed by a thresholding step to create a binarized map of the vessel tree. The intensity distribution of the vessels can be used as a feature to detect vessels in an image. Commonly used kernels for retinal vessels can be generally divided into Gaussian (including mixture of Gaussian and/or its derivatives) and non-Gaussian shaped kernels (such as cubic spline, Laplacian, or Hermite polynomial). Because of lower reflectance of blood vessels in comparison to the surrounding

tissue, they appear darker in fundus images. The intensity profile of the blood vessels can be derived by an inverted Gaussian distribution (Kar et al. 2017). To extract the whole retinal vascular tree map, the input image is filtered by a bank of filters or kernels of different sizes and orientations. Singh *et al.* (Singh et al. 2016) could improve the performance of the segmentation of the retinal vessels by using the Gumbel probability distribution as a kernel instead of Gaussian function.

Vessel tracking/tracing methods initiate with a selection of seed points and a tracing criterion derived from local information of the image to track the centreline or ridges of vessels. The initial seed points can be selected either interactively or automatically. Tracing vessel ridges may be obtained through a variety of methods including but not limited to the detection of the gradient and curvature zero-crossings (Jeyasri et al. 2013), Kalman filter (Yedidya et al. 2008), Hessian filter (Abdallah et al. 2015), Bayesian (Zhang et al. 2014), or graph theory (Rattathanapad et al. 2011). Vessel tracking techniques are found to be particularly beneficial for precise measurement of vessel width and detection of vessel structure like connectivity and branching (Fraz et al. 2012).

Mathematical morphology is a division of set theory and has been extensively used in image processing to extract or manipulate spatial structures in an image. Morphological operators use structuring elements to probe the input image which can be binary, grey-scale or even coloured. Dilation and erosion are the two main morphological operations. Dilation boosts and expands the objects in the image, connects gaps and fills holes. On the contrary, erosion, as a dual operation of dilation, shrinks and lessens image components (Gonzalez et al. 2007). Hassan *et al.* proposed a method for retinal vessel segmentation using mathematical morphology followed with K-means clustering (Boutsidis et al. 2015). The application of a rotating linear structuring element with a varying length at different angles and across

multiple scales was also successfully tested to extract the retinal vessel tree (Kundu et al. 2012).

Multi-scale segmentation approaches are useful when the objects of interest are presented at variable sizes and dimensions. Given that the calibre of retinal vessels decreases gradually as they leave the optic disc, the basic idea behind multi-scale methods is to detect vessels of different width in several steps through scale-space decomposition of the image (Wink et al. 2004). Again, Gaussian function and its derivatives are amongst most popular scalable kernels used in multi-scale vessel segmentation (Zhang et al. 2015). Sofka and associates presented a combination of matched filter responses derived in scale-space to extract varying width vessels with a likelihood test measuring the so-called “vesselness” at each pixel (Sofka et al. 2006). Fraz *et al.* outlined more examples of the application of multi-scale analysis in the segmentation of retinal vessels (Fraz et al. 2012).

Apart from kernel-based methods which model vessel profile, shape modelling methods can be divided into parametric and geometric deformable models. This subgroup of segmentation techniques refers to flexible curves (in 2D or surfaces in 3D) which deform to match vessels in the retina. Deformation or evolution is controlled by either an energy minimization or a curve evolution criterion. Parametric deformable models, also known as snakes (Espona et al. 2007) or active contours, represent a parametric curve which initializes in a proximity of a vessel and iteratively evolves to the vessel boundaries. One shortcoming of snake-based models is that being controlled by parameters, the contour is not generally flexible enough to fit complex structures. Furthermore, the segmentation is degraded dramatically in the presence of noise and in low contrast images. On the other hand, geometric deformable models such as level sets (Guc et al. 2015) are represented as a set of an auxiliary distance function which may flexibly join or split without the need of reparameterization.

The core idea behind adaptive thresholding is to find the intensity levels (in case of grey-scale images) which represent different objects in an image. The applicability of thresholding methods in segmentation of retinal images is however challenged by non-uniform illumination, image artefacts induced by camera or abnormalities like lesions, exudates, haemorrhage, or drusen, unstable contrast and unclear boundaries due to smooth transition between intensity levels. Accordingly, to address the limitations of ordinary thresholding techniques, several knowledge- and region-based thresholding methods have been proposed for the segmentation of retinal vessels. Local relative entropy thresholding (Kande et al. 2008), adaptive thresholding based on grey-level co-occurrence matrix (GLCM) energy (Mapayi et al. 2015), C-means thresholding (Dash et al. 2017), and Otsu thresholding (Gonzalez et al. 2007) with principle component analysis (Dash et al. 2018) are some examples of the application of thresholding in the segmentation of retinal vessels.

Pattern recognition implicitly needs some sort of machine learning procedure. Machine learning algorithms can be subdivided into three major categories namely supervised, unsupervised and reinforcement learning. While supervised methods use a subset of data labelled by observed output as a training set to classify unseen data, unsupervised learning explores similarity to cluster unlabelled data. In reinforcement learning, on the other hand, training is achieved through trial-and-error targeting maximum long-term reward (Mnih et al. 2015). Generally, superior performance has reported by algorithms incorporating *a priori* knowledge at the cost of higher computation, and labour-intensive, time-consuming process of collecting the training set which is prone to inter- and intra- examiner inconsistency. On the other hand, although unsupervised clustering methods are faster, they are more often tailored for specific settings in a way that their application to a new data set does not provide expected result unless after significant modifications. There are many examples of the application of machine learning in retinal vessels segmentation. For example, Soares *et al.* proposed an

automated method for the segmentation of retinal vessels using 2D Gabor wavelet transform and a Bayesian classifier with class-conditional probability density likelihoods described as Gaussian mixtures (Soares et al. 2006). Ricci and Perfetti proposed two orthogonal line detectors in conjunction with a support vector machine (SVM) for pixel-wise classification of vessels in retinal images (Ricci et al. 2007). The training set was randomly selected from test images. Marín *et al.* presented a supervised method for the segmentation of retinal vessels using grey-level and moment invariants features (Marín et al. 2011).

Mudassar *et al.* implemented and compared four segmentation techniques for the extraction of the entire vessel tree using image line cross-section (ILCS), modified matched filter (MMF), continuation algorithm (CA), and a method using edge enhancement and edge detection (EEED) (Mudassar et al. 2013). These techniques were exclusively designed for segmentation of retinal vessels in poor-quality images with low-contrast and/or distortions like drusen or other abnormalities.

The ILCS method first applies a homomorphic filter on the input image to compensate inhomogeneous illumination in the retinal images. In the next step, the intensity profiles of the resultant image along a set of horizontal lines are computed with adaptive thresholds by statistically computed thresholds derived from local intensities. The output binary lines are then combined to generate a binary map of the vessel tree of the input image.

MMF method uses a set of Gaussians filters of the same size but rotated from 0° to 180° by 9° steps to enhance the vessels in retinal images. The output image of matched filtering then is binarized by Otsu thresholding to obtain a binary map of blood vessel tree.

The third method using CA is developed to address discontinuity of the vessel tree as the main drawback of the matched filtering and similar segmentation method. The obtained

vascular tree is often broken and incomplete especially at thin vessels due to low contrast (Fraz et al. 2012). Considering that most segmentation methods are followed by a noise removal or length filtering step for eliminating small isolated artefacts, an effective merging procedure is important to ensure accurate segmentation of thin vessels. For this purpose, two binary images from the vessel tree are generated with one depicting only thick vessels (called as reference image) and the second image containing both thick and thin vessels and naturally noise (referred to as test image). Binary images may obtain using any segmentation method including matched filter. CA extends the tree in the reference image by replacing background pixels where there is at least one foreground pixel in a small sliding window around the corresponding pixel in the test image. This way, the vessel tree in the reference image is extended only at pixels where the corresponding pixel in the test image is a vessel but not noise or isolated artefact. The procedure iterates until the condition does not meet anymore. This process is applied consecutively on the vertically- and horizontally-flipped versions of the extended tree.

Segmentation of retinal vessels based on EEED is robust and fast. In order to both smooth the uneven background and enhance the boundaries of the vessels at the same time, EEED applies a Laplacian of Gaussian (LOG) filter (Ding et al. 2017) on the image. While matched filtering enhances vessels using kernels at different angles, LOG is an isotropic filter. EEED first, extracts the illumination pattern of the background using a large blurring LOG filter. The minimum of the original and blurred image presents retinal vessels enhanced and more contrasted against the background. The ensuing image is then blurred using a small Gaussian kernel to keep broken pieces of vessel tree connected. The algorithm follows by the application of a smaller LOG filter to obtain better contrast of vessel tree. Next step is binarization by Otsu thresholding followed by a length filtering to clear small isolated unwanted blobs from the image.

Comparison of the four techniques over 30 poor quality and 105 normal images showed while it is computationally simple and cheap, the CA technique outperforms the remaining three techniques (Mudassar et al. 2013). In addition, it does not need any sort of filtering at any stage which helps obtaining more accurate segmentation of the blood vessels with less risk of missing part of the tree. EEED method was the second best in terms of both performance and simplicity.

2.8.2 Vessel diameter measurement

Unlike numerous studies on vessel segmentation in general and retinal vessel segmentation in particular, little has been published on direct measurement of vessel diameter. Existing methods for the measurement of vessel diameter can be classified as parametric and non-parametric methods. Non-parametric methods mainly measure the diameter of the vessel from the vessel contour which demands the segmentation of vessels from the background as a primary step. The accuracy of the measurement can therefore be substantially degraded by unclear contrast between vessel boundaries and the background and in the presence of abnormalities and artefacts. Furthermore, the result may be influenced by the thresholds or morphological structuring elements which are used in most of the segmentation algorithm at some stage. In parametric methods such as curve fitting and profile modelling the diameter is estimated by parameters representing the model which best fits the cross-sectional intensity profile of the vessel (Araújo et al. 2018). This parameter may be the area under a curve in curve fitting methods, or for example the standard deviation or more accurately the spreading factor (in case of mixture models) of the best Gaussian fit in profile modelling methods.

As mentioned earlier, the cross-sectional profile of the vessel is commonly estimated by an inverse Gaussian shape. The assumption, however, does not hold in the presence of image artefacts and central light reflex also known as specular reflection. Central light reflex distorts

the bell-shaped Gaussian curve by creating a peak in the middle of the profile. Figure 2.10 illustrates the cross-sectional intensity profile of a vessel in presence of central light reflex.

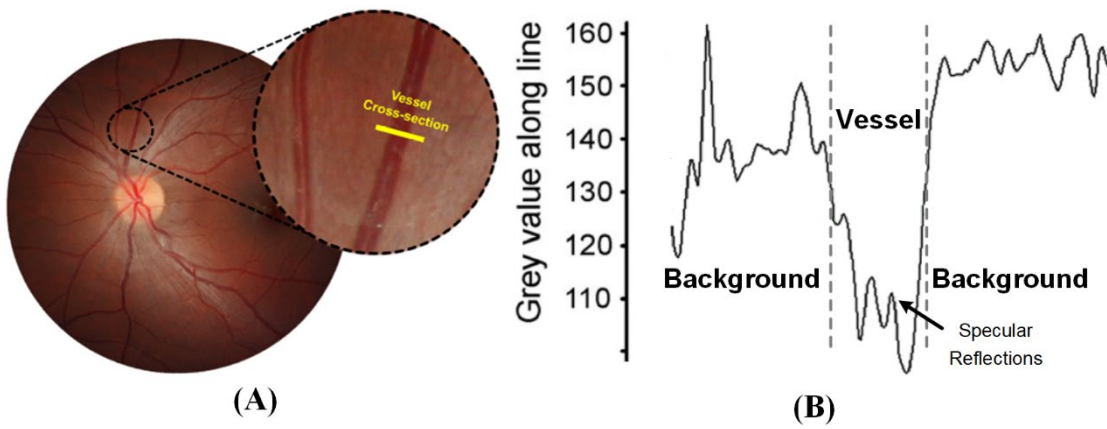


Figure 2.10. An illustration of a retinal vessel in a fundus image (A) and its cross-sectional intensity profile in the presence of specular reflection (modified from (Aliahmad 2014))

The precision of diameter measurements based on parametric model fitting is dependent on the model selection. Therefore, several models have been suggested to better match the actual profile of the vessels. Piece-wise Gaussian models (Li et al. n.d.) and difference-of-Gaussian-based models (Gao et al. 2001; Araújo et al. 2018) are some of the modifications proposed to introduce central light reflex to the model. However, vessel profile may present an asymmetrical or skewed shape. Hermite model (L. Wang et al. 2007) considers both central light reflex and vessel asymmetry.

Alternatively, some approaches measure the calibre at points of interest. The ImageJ DIAMETER plugin (Fischer et al. 2010) for example initiates with an interactive selection of a vessel. The user draws a line crossing the vessel of interest at both sides perpendicularly. After the intensity of the image at the pixels belonging to the line is derived, the algorithm primarily estimates the vessel boundaries by finding the maximum intensity changes along the line. The algorithm approximates the intensity profile of the vessel along the line by an inverted Gaussian function. Having the two intensity values estimating the intensity level at

the vessel border at each side, the inverse bell-shaped profile is divided into three regions by two reference values representing lightest area outside the vessel and one intensity level corresponding to the darkest intensity inside the vessel. Taking a pair-wise average of the lowest (darkest) reference and each of bright references for each side provides two intensity thresholds. The intersection of each threshold with the line passing through the two initial boundary estimates determines the vessel boundaries and ultimately the diameter. For the sake of accuracy, measurements are repeated along four lines parallel to the input line shifted by one and two pixels at each side.

Chapter 3

Retinal PWV - method and modelling

The methods described have been submitted for publication as:

Rezaeian M, Butlin M, Golzan SM, Graham SL, Avolio P.A. A Novel Method for Retinal Vessel Segmentation and Diameter Measurement Using High Speed Video. *Conf Proc IEEE Eng Med Biol Soc*. 2019 July.

This chapter describes the general video analysis method used in *in-vivo* experiments. A novel method developed for the quantification of vessel diameter changes over time and measurement of pulse transit time for the purpose of PWV calculation in retinal arteries is presented. Detailed and specific explanations of material and methods for each individual experiment has been provided in the corresponding chapters.

3.1 High-speed imaging

A Zeiss ff450 plus fundus camera (Zeiss, Oberkochen, Germany) with a resolution of 768×576 (pixel size $0.68\text{mm} \times 0.68\text{mm}$) was used to record retinal vascular changes in humans. A 60D lens was placed on the original fundus lens for more detailed and magnified imaging in rats. Since the heart rate in rats is almost up to 500 beats per minute, a high-speed camera (Optronis, Kehl, Germany) was mounted on top of the Zeiss fundus camera to capture fast retinal pulsations at a rate of 125 frames per second (fps). The final spatial resolution of the whole optical imaging system was $6.06 \mu\text{m}$.

To facilitate exposure to high levels of light required for high-speed imaging and to record high quality images while animals remain immobilized, animals were anesthetised with a single dose intraperitoneal injection of Urethane (1.3g/kg). Pupils were dilated by administration of tropicamide 1% ((Mydriacyl, Alcon)). To prevent the corneal surface from drying, an ophthalmic lubricant gel was applied throughout the experiment as necessary. A 0.9% physiological saline solution was also used to avoid dehydration of the eyes as required.

3.2 Proposed method for retinal vessel analysis

The algorithm for the assessment of time-dependent characteristics of retinal vessels specifically PWV in retinal arteries is composed of three modules: vessel segmentation, diameter measurement and calculation of pulse transit time. The proposed vessel segmentation method starts with an adaptive contrast adjustment procedure to enhance the intensity of the vessels against the background in the video stream. Next, the entire sequence of images is registered to align the frames and compensate for motion artefacts produced by the eye and the respiratory displacements. To achieve more accurate diameter measurements at a faster speed and less computational cost, an artery is selected interactively by the user. Given the length of the vessel segment to be analysed, the algorithm, automatically crops the

vessel segment of interest from all frames. The rest of the algorithm operates on this region of interest (ROI) cropped from the image sequence rather than whole frames. For a precise segmentation of the vessels' boundaries, image artefacts are first removed by an anisotropic diffusion filter. Using an edge detection algorithm, the boundaries of the vessel segment are segmented.

The diameter of the vessel is measured as the Euclidean distance between the intersection pairs of the input line with the vessel boundaries at each side. To obtain more robust and accurate measurements, the algorithm measures the diameter along four parallel shifts of the input line. After computing the intersections, missing values and outliers are replaced by a spline interpolation.

To obtain PWV in retinal arteries, diameter waveforms at proximal and distal cross-sections along an individual artery are extracted using the above techniques. PWV is then calculated as the ratio of the distance between two set points to the time taken for a pulse to travel this distance. The time delay is measured from the slope of the regression line of the phase differences between the Fourier components of proximal and distal diameter waveforms ranged around the cardiac frequency on angular frequencies in that range.

Figure 3.1 shows a block diagram of the proposed method programmed in MATLAB® (The MathWorks Inc., Natick, MA, USA). Each step has been described in more detail in the following sections.

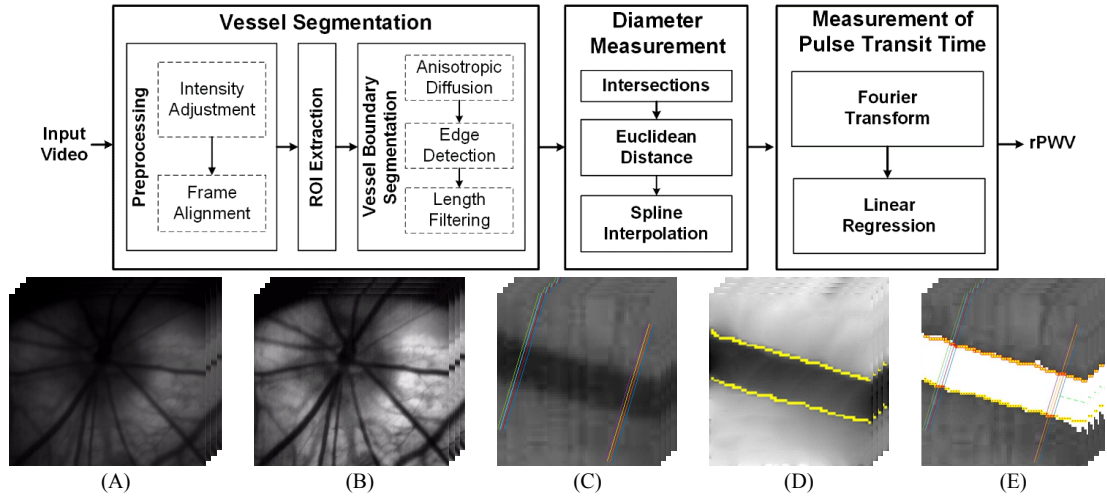


Figure 3.1. Top panel shows a block diagram of the proposed method for the measurement of PWV in retinal arteries. Bottom panel shows (A) the input fundus video, (B) the output of the intensity adjustment followed by frame alignment, (C) the ROI extracted from the video sequence, (D) vessel boundary segmentation, and (E) the intersections of the vessel boundaries with the input and four parallel lines at proximal and distal sites.

3.3 Segmentation of retinal vessels

3.3.1 Intensity adjustment

Contrast limited adaptive histogram equalization (CLAHE) (Reza 2004) is used to improve the contrast between vessels and the rest of the image. Unlike ordinary static histogram equalization techniques which operate on the entire image, CLAHE partitions the image into non-overlapping tiles of identical size to tackle global noise in the image by redistributing the intensity values to match to the histogram indicated by the distribution parameter. The histograms of the tiles are clipped at a predefined contrast value to limit the overamplification of noise in homogeneous regions. To eliminate artificially induced edges generated by tiles and simultaneously improve computational efficiency, adjacent tiles are combined by means of interpolation. Figure 3.2 demonstrates the result of the application of the CLAHE algorithm on a representative image from the rat retina.

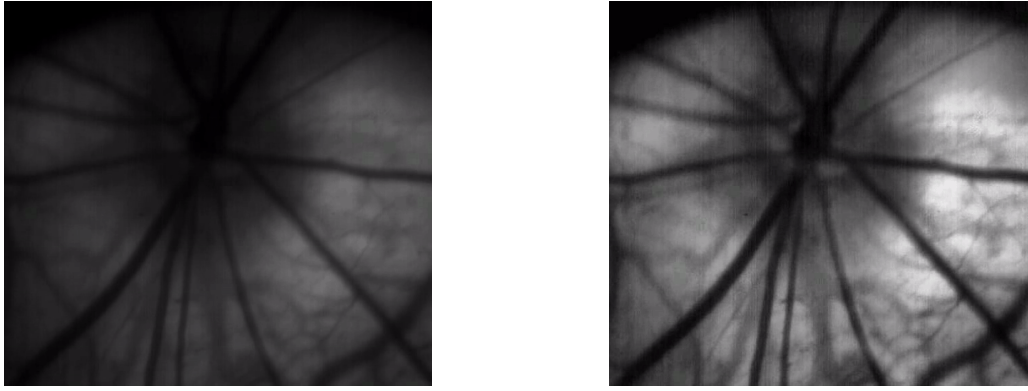


Figure 3.2. The original image (left) and the output of CLAHE (right)

3.3.2 Registration and alignment of image stack

Even in anaesthetised rats, fundus videos demonstrate noticeable misalignment between frames which is a major problem in video analysis. Using the translation function of the StackReg plugin (Thevenaz et al. 1998) of the ImageJ (Schneider et al. 2012) the entire image stack is aligned and corrected for translational shifts induced by respiration. The registration algorithm uses subpixel methods to detect subtle changes between images. Marquardt–Levenberg nonlinear optimization (Marquardt 1963) is applied on intensity differences to find least-squares. The search strategy exploits a coarse-to-fine iterative pyramid approach based on a spline representation of the images. Multiresolution search provides robustness against local minima and spline interpolation minimises blurring of images. The alignment procedure propagates by using each frame as a reference for the succeeding frame.

3.3.3 ROI extraction

As mentioned earlier, uneven background illumination and varying vessel intensity make accurate segmentation of the whole vascular tree challenging. Furthermore, even a one-second video captured at 125 fps with frame dimensions of 1280×1024 pixels, requires massive memory storage (470 Mb) and processing. Therefore, it is necessary to devise a way to reduce computational costs by avoiding unnecessary and redundant calculations. For this purpose, a segment of the vessel of interest is cropped throughout the image stack for further analysis.

The user draws an orthogonal line traversing both ends of the vessel's borders. To crop the ROI, the algorithm needs the length of the vessel segment to be analyzed and a direction to find the endpoints of the ROI. Since retinal vessels in the rat eye are arranged in a spoke-like radial configuration (Figure 3.3), assuming the user-drawn line to be proximal to the optic disc, the algorithm only requires a non-precise location of the optic disc relative to the input line to calculate the distal cross-section at a given distance. Therefore, rather than automatically localizing the optic disc using edge detection techniques like circular Hough transform, Radon transform, or SUSAN operator (Gui et al. 2018) for extra unnecessary computations, the algorithm proceeds with a single input from the user anywhere on the image on the same side of the input line where the optic disc is located. The coordinates of the endpoints of the line at the distal cross-section is then automatically computed according to the given distance between proximal and distal sites.

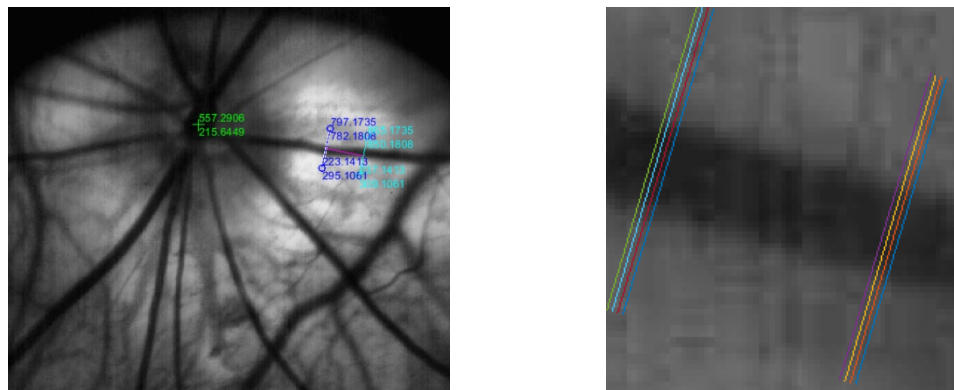


Figure 3.3. An example of ROI extraction and the calculation of the distal site in a fundus image from the rat eye. The line in blue in the left panel shows the input line drawn by the user. Optic disc is located on the nasal side of the input line. Given a relative location of the optic disc (green) and the distance between proximal and distal sites, the distal line (cyan in the left panel) is calculated.

3.3.4 Anisotropic diffusion

As mentioned earlier, inhomogeneous background poses a major difficulty to vessel segmentation in fundus images. Prior to any further analysis, the intensity clutters must be suppressed from the images. Anisotropic diffusion, first introduced by Perona-Malik (Perona et al. 1990), is an effective noise removal technique which preserves image edges. While

conventional noise removal techniques degrade sharp edges, inspiring from the heat diffusion equation, anisotropic diffusion filtering uses an adaptive weighting strategy to control diffusivity in homogeneous areas and near edges of the image. The basic idea can be formulated by Equation 3-1

$$\frac{\partial I}{\partial t} = \text{div}(c(\|\nabla I\|) \cdot \nabla I_{x,y}(t)) \quad \text{Equation 3-1}$$

For a given image I , the divergence operator measures density changes and $\nabla I_{x,y}(t)$ is image gradient representing local changes in the image intensity in different directions. For pixels belonging to a flat homogenous area, the gradient $\|\nabla I\|$ is close to zero. A selection of a constant diffusivity (c), regardless of local changes, results in a linear diffusion equation and smoothing and blurring of the image edges accordingly. Choosing the diffusivity to be a function of image local changes such as image derivatives enables suppressing image artefacts while remaining sharp edges. Here the diffusivity is selected according to Equation 3-2:

$$c(\|\nabla I\|) = \frac{1}{(1 + \frac{\|\nabla I\|}{k})^{\alpha+1}} \quad \text{Equation 3-2}$$

where constants k and α control the smoothing level and are chosen experimentally. However, once they are set, they remain fixed. That means the parameter selection is general and robust enough that it can be applied to all the videos captured by the same device and under the same setting with no need for reparameterization. Figure 3.4 shows an illustration of the result of applying anisotropic diffusion filter on a representative image.

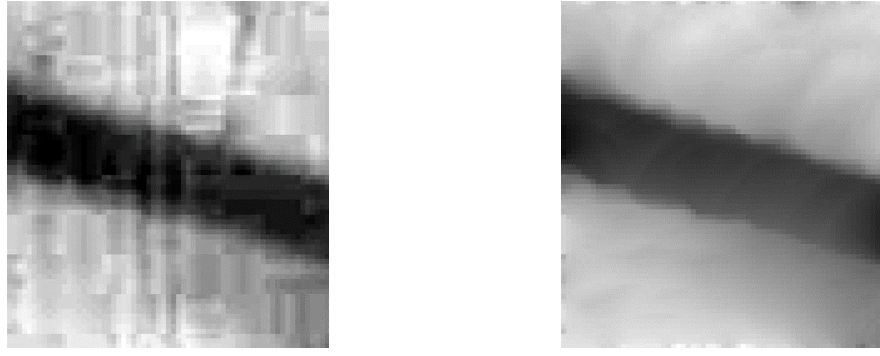


Figure 3.4. Left column shows the input image and the right column shows the result of anisotropic diffusion filtering.

3.3.5 Segmentation of the vessel boundaries

The next step of the vessel segmentation algorithm uses the enhanced image to segment the boundaries of the vessel. An edge pixel demonstrates sharp changes in image intensity. Many differential edge detection techniques such as Robert, Prewitt, Sobel, Canny, Laplace, and Laplacian of Gaussian (LOG) have been developed based on finding the maxima of first derivatives or zero-crossing of the second derivatives of the image to localise edges. This further highlights the importance of artefact removal and noise suppression phase prior to edge detection as image artefacts are amplified in gradient images.

The Canny edge detection is applied to extract pixels belonging to the vessel boundaries as it outperforms other edge detectors. The Canny algorithm is a multi-step procedure starting with a smoothing Gaussian filter for noise cancellation. The gradient of the image is then calculated within a sliding window of size 2 using $G_x = \begin{bmatrix} -1 & 1 \\ -1 & 1 \end{bmatrix}$ and $G_y = \begin{bmatrix} 1 & 1 \\ -1 & -1 \end{bmatrix}$ as horizontal and vertical gradient operators respectively. To assure that each edge is one-pixel in width, only pixels with gradient magnitude greater than their two neighbours along the gradient direction will be kept. The candidate edge pixels from non-maximum suppression phase, then pass a connectivity check through a double thresholding process. If the gradient magnitude is above the high-threshold the corresponding pixel is marked as edge pixels and if it is less than the low-threshold the pixel, it will be eliminated from the edge map. Among

candidate edge pixels with the gradient magnitude between the low and high thresholds, those which are connected to the edge pixels will be kept. The algorithm ends with filling the gaps between edge segments using the two binary images from each threshold. **Figure 3.5** shows the vessel's boundaries segmented using the Canny edge detector.

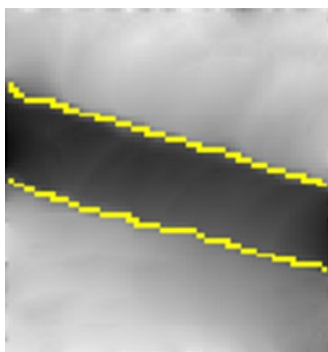


Figure 3.5. Vessel boundaries segmentation

Some of the images may present unwanted isolated or false edges. This can be handled by the application of a length filtering posterior to the edge detection (Figure 3.6).

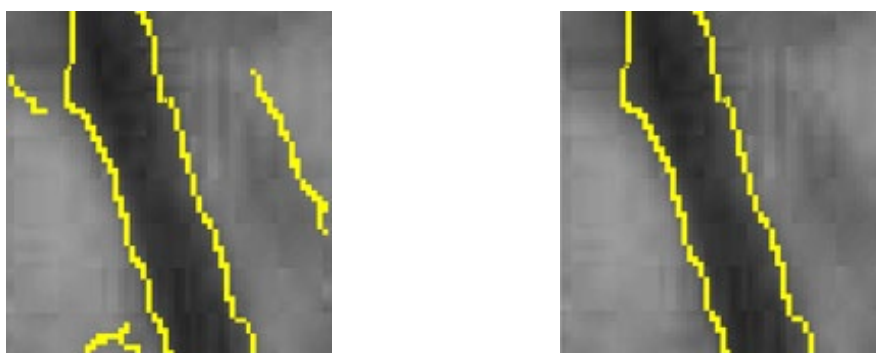


Figure 3.6. Left: vessel segmentation; right: same image after length filtering

3.4 Measurement of vessel diameter

Vessel diameter was measured as the Euclidean distance between the intersections of the vessel boundaries at each side with the input line. To obtain more accurate measurements, in addition to the line drawn by the user, the algorithm takes four extra measurements along parallel lines shifted one and two pixels at each side of the input line. For the measurement of the PWV, five measurements of the diameter at a distal intersection of the selected artery with

a given distance from the proximal site are taken as well (Figure 3.7). After eliminating possible outliers (if any), the average of the remaining measurements at each site is taken as diameter.

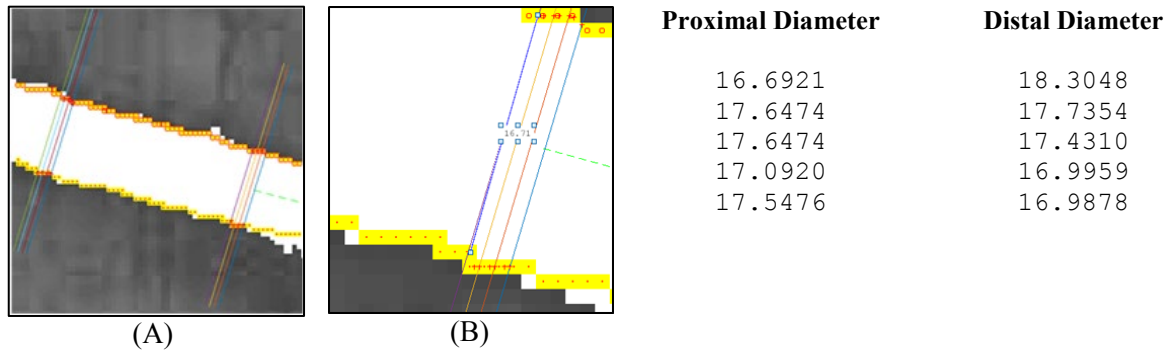


Figure 3.7. (A) vessel borders are segregated using the medial line of the vessel and the diameter is measured at the proximal and distal sites. (B) For each cross-section, the algorithm takes five measurements along orthogonal shifts.

Applying the algorithm on the full image stack returns the changes of the vessel diameter over time. A representative retinal arterial diameter waveform from the rat eye is shown in **Figure 3.8**

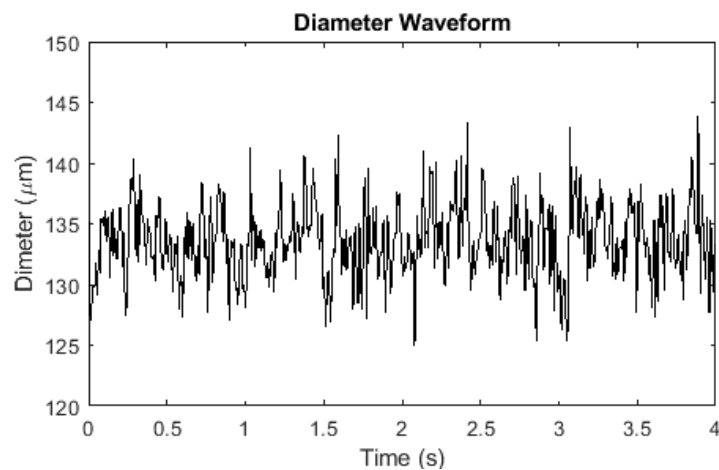


Figure 3.8. Retinal arterial pulse obtained from diameter changes in the rat eye.

One limitation of the proposed method is that it is not robust to self-intersections which may occur in poor-contrast images or in presence of buckled vessels especially in the human retina. One possible solution is using the centreline of the vessel to separate pixels belonging

to vessels boundaries at each side. The Hough transform (Mukhopadhyay et al. 2015) can be used for centreline extraction. First, the intensity of the ROI is adjusted to enhance the contrast of the vessel against the background. The histogram of the resultant image presents two peaks. The first peak on the left (low-intensity) side of the histogram represents the vessel which appears darker since light is mostly absorbed while passing through the blood vessels. The right peak corresponds to the bright background pixels. The Otsu algorithm (Dash et al. 2018) is then used to automatically select an optimum threshold between the two peaks minimising the intra-class variance and maximising the inter-class variance for the foreground (vessel) and the background classes. This threshold outputs a binary image representing non-precise segmentation of the vessel region.

The Hough transform of a binary image maps each foreground pixel (x, y) in the image to a sinusoid of the form $\rho = x\cos\theta + y\sin\theta$, where ρ is the radial distance from the origin and θ is the azimuth angle with horizontal axis in the counter clockwise direction. Given that the ROI ideally contains most of the vessel pixels oriented in a specific direction, the vessel region in the binary image generates several sinusoids intersecting in a single point. The inverse Hough transform of this point represents the centreline of the vessel (**Figure 3.9**).

Using the centreline of the vessel, pixels belonging to the vessel boundaries obtained using edge detection are separated. Again, the Euclidean distance between the two points at which the input line crosses each of the vessel boundaries is equal to the vessel diameter.

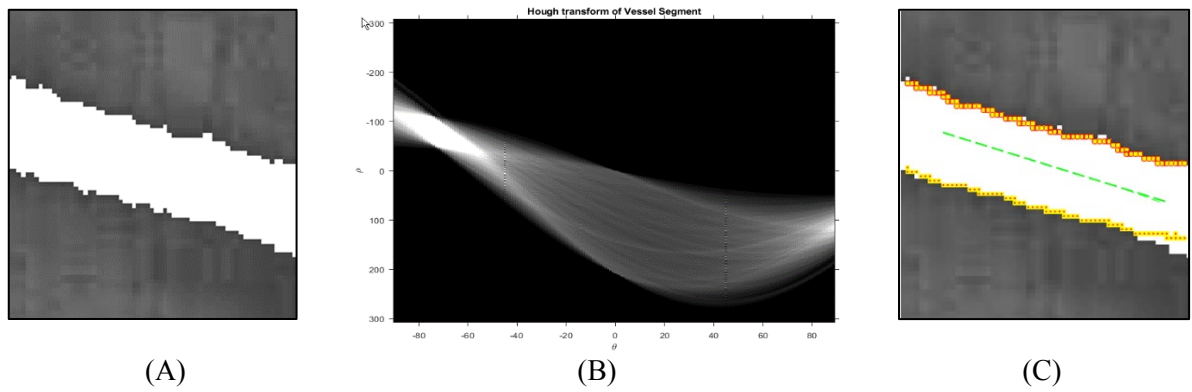


Figure 3.9. Finding the centerline of the vessel using inverse Hough transform. (A) binarized region of vessel overlaid on the gray image. (B) The Hough transform of the binarized ROI. The first intersection in the left side of the plot corresponds to the pixels aligned along the vessel length and the second congestion on the right side resembles the foreground pixels aligned along the vessel width. (C) The centerline (green dash line) in the left panel is generated using the invert Hough transform of the left intersection in (B). Vessel boundaries are segregated using the centerline.

The efficacy of the centreline solution was tested and confirmed by several images of twisted vessel segments. However, since retinal vessels in the rat eye are arranged in a spoke-like radial configuration, the self-intersection problem was unlikely to happen. Furthermore, even in humans, to avoid the effect of tortuosity on PWV, straight segments were selected away from bifurcations or crossings. Accordingly, the extraction of the vessel medial line using Hough transform was skipped as it was not useful but imposed unnecessary extra calculations.

Poor contrast and inaccuracy or failure in vessel boundary segmentation may result in outliers or missing values in diameter measurements. Hence, the resulting retinal pulse is fitted using a cubic spline interpolation to fill the temporal gaps and replace the outliers. Data points with values larger than three scaled standard deviations from the mean are considered as outliers (Figure 3.10).

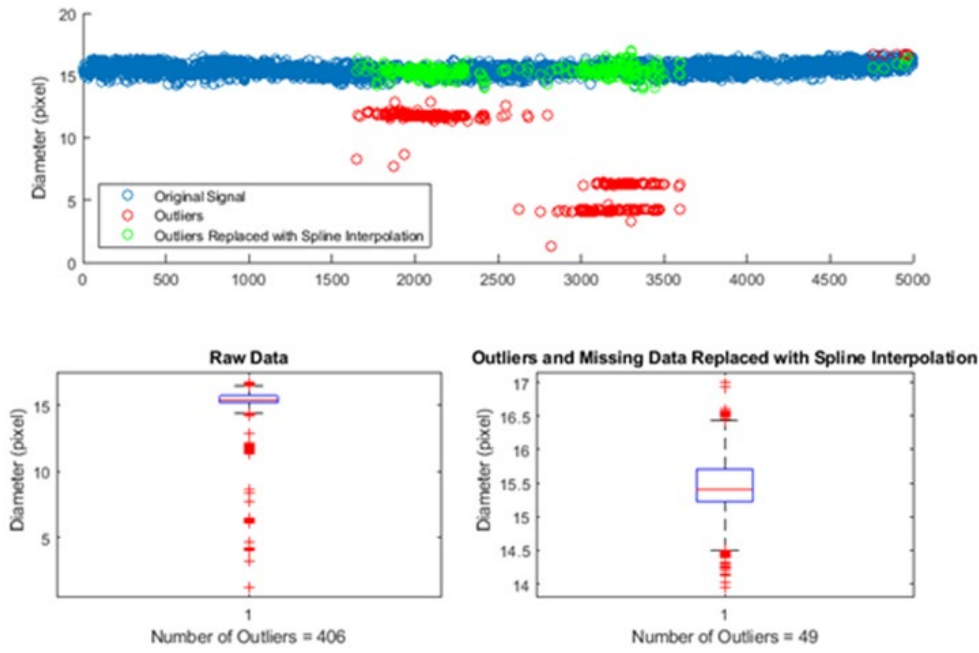


Figure 3.10. Replacing missing values and outliers with cubic spline interpolation

3.5 Pulse transit time calculation

Measurement of PWV requires determining the time taken for a pulse to travel between two set points. Time delay between two signals can be quantified through cross-correlation, the phase shift between filtered harmonics of the two signals or foot-to-foot methods. Since the signal-to-noise (SNR) ratio of the retinal pulses was not adequate for performing correlation or foot-to-foot distance calculations, the phase difference between cardiac harmonics was exploited to compute the temporal shift between proximal and distal pulses.

As demonstrated in Figure 3.11, Fourier analysis of retinal arterial diameter time series exhibits a dominant component at the heart rate frequency.

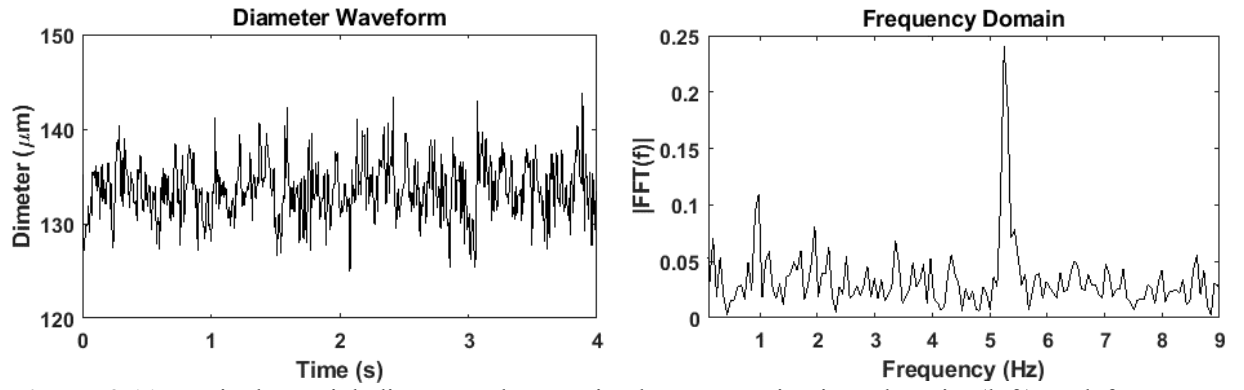


Figure 3.11. Retinal arterial diameter changes in the rat eye in time domain (left) and frequency domain (Right). The frequency spectrum has power at the cardiac frequency (4.7 Hz for the rat).

The Fourier transform of the retinal arterial diameter waveforms at the proximal and distal cross-sections were computed. Then, the phase differences between the two at the frequency components around the cardiac frequency (0.66-3 Hz in human and 4-6 Hz in rat) were calculated. The time delay is related to the phase shifts according to the following formula:

$$\Delta t = \frac{\varphi}{2\pi \times f_{HR}} \quad \text{Equation 3-3}$$

Accordingly, the pulse transit time (PTT) between the proximal and distal sinusoidal components was computed as the slope of the regression line of phase differences on angular frequencies as depicted in **Figure 3.12**.

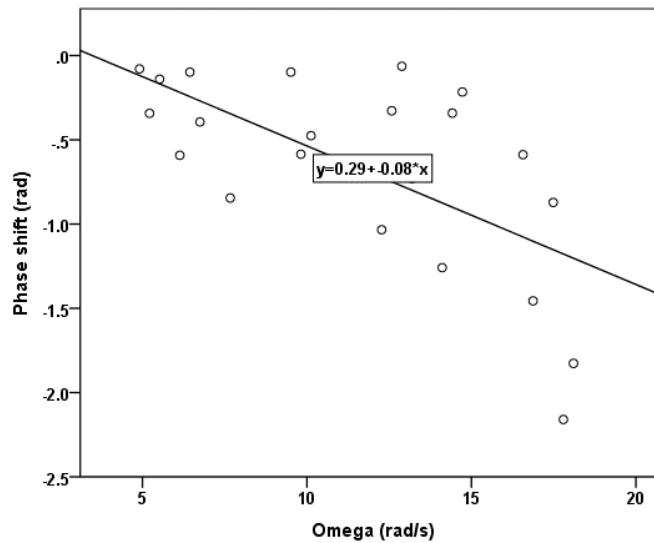


Figure 3.12. Calculation of PTT as the slope of the regression line of phase shifts computed by Fourier transform on the angular frequencies

3.6 Evaluation of Methods

3.6.1 Vessel segmentation

Figure 3.13 shows illustrative results of vessel segmentation for a sequence of images.

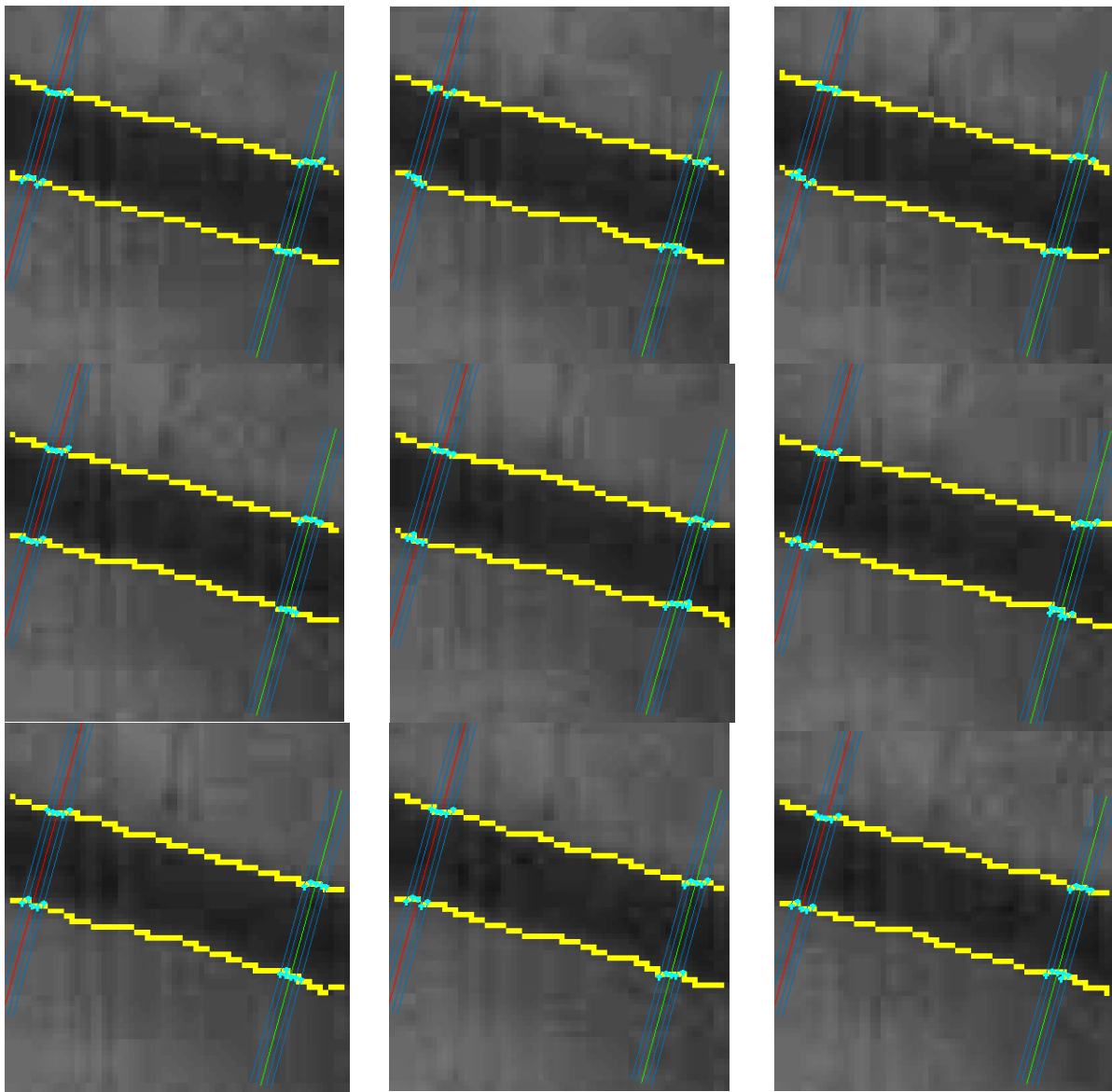


Figure 3.13. Representative segmentation results for 9 consecutive frames

Considering vessel segmentation as a binary classification task to segregate vessel and non-vessel pixels, the area under the receiver operating characteristic (ROC) curve is used to evaluate the segmentation performance over 25 images from vessel segments. A ROC graph

plots sensitivity (true positive rate) as a function of specificity (1 - false positive rate). The spontaneous compromise between specificity and sensitivity makes the ROC curve to start from bottom left and end at the top right. Hence, for an ideal classifier with 100% specificity and sensitivity, the ROC curve passes through the upper left corner with an area under curve (AUC) equal to 1. The closer a ROC curve is to the top left corner, the better is the segmentation performance.

The number of mis-classified pixels were counted categorised as false vessel or false non-vessel visually to calculate specificity and sensitivity in each image. It is worth noting that in most cases, deciding whether the pixel belongs to the vessel boundary or not is not straightforward due to poor contrast and ambiguous vessel borders in the images. **Figure 3.14** shows the obtained ROC with an AUC of 0.987.

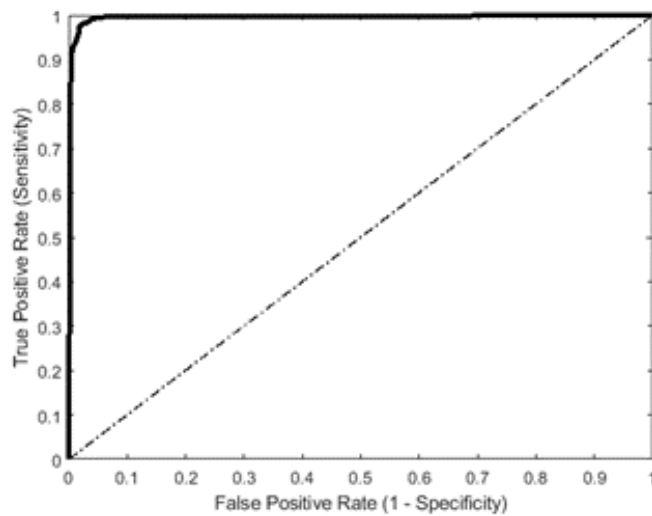


Figure 3.14. ROC curve for segmentation results of 25 images

3.6.2 Diameter measurement

For the purpose of either PWV or pulsatility index calculation, the precision (low error variance) of the segmentation is more favourable than the accuracy (low mean error). The performance of the proposed diameter measurement method has hence been evaluated by the standard deviation of the diameter errors. For this, diameter residuals were calculated by

Table 3.1. Specificity and sensitivity of the vessel segmentation over 25 vessel segments

	Specificity	Sensitivity
Vessel 1	0.9965	0.8987
Vessel 2	0.9965	0.9068
Vessel 3	0.9945	0.9169
Vessel 4	0.9924	0.9291
Vessel 5	0.9883	0.9392
Vessel 6	0.9863	0.9474
Vessel 7	0.9843	0.9555
Vessel 8	0.9822	0.9636
Vessel 9	0.9822	0.9737
Vessel 10	0.9781	0.9778
Vessel 11	0.9741	0.9818
Vessel 12	0.9679	0.9839
Vessel 13	0.9618	0.9899
Vessel 14	0.9557	0.992
Vessel 15	0.9496	0.994
Vessel 16	0.9394	0.996
Vessel 17	0.9333	0.996
Vessel 18	0.9272	0.998
Vessel 19	0.917	0.996
Vessel 20	0.9129	0.996
Vessel 21	0.9047	0.9959
Vessel 22	0.8986	0.9959
Vessel 23	0.8884	0.9959
Vessel 24	0.8843	0.9959
Vessel 25	0.8782	0.9959

subtracting the 100 diameter measurements obtained from the 10 test vessel segments (five measurements at the proximal and five at the distal cross-sections) from ground truth diameters at the same sites. The residual at a given cross-section i is given by $\chi_i = \omega_i - \psi_i$, where ω_i is the diameter measured by the proposed method and ψ_i is the user benchmark. The standard deviation of residuals calculated as per Equation 3-4 gives the spread of diameter errors.

$$\sigma_{error} = \sqrt{\frac{1}{n-1} \sum_{i=1}^n (\chi_i - \mu_{error})^2} \quad \text{Equation 3-4}$$

where μ_{error} is the mean of residuals: $\frac{1}{n} \sum_{i=1}^n \chi_i$.

The 100 width estimates returned by the diameter measurement algorithm were subtracted from 100 corresponding user benchmark widths exactly at the same spots. Using width differences, the standard deviation of the width differences was then taken. The standard deviation of the errors was 0.41 pixels. **Figure 3.15** shows the Bland-Altman plot of the measured and manual diameters from 10 consecutive frames. 10 measurements were taken from each frame, 5 at the proximal and 5 at the distal cross-sections. The mean and standard deviation of the errors were -0.147 and 0.41 pixels respectively.

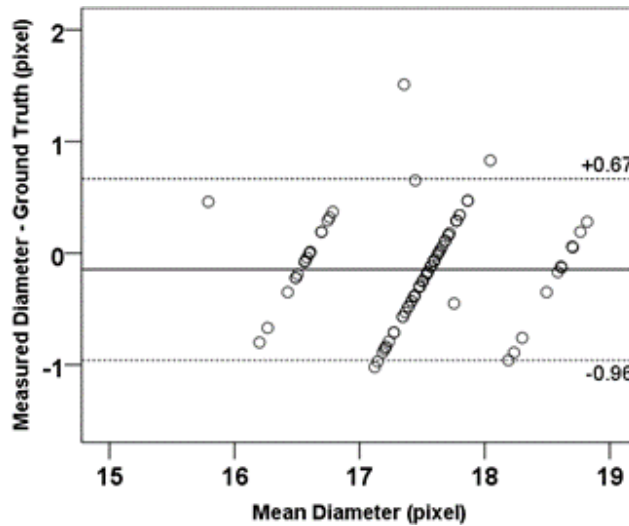


Figure 3.15. Bland-Altman plot of the automated and manual diameter measurements for 20 consecutive frames; Solid line gives the mean difference. Dashed lines give mean $\pm 1.96 \times$ standard deviation.

3.7 Comment and implications for the evaluation of PTT measurement

Validating PTT measurements is not straightforward as there is substantial inconsistency between the reported values in the literature. Only six studies have measured PTT in retinal arteries, and it is a very new field. The reported values for rPWV differ by orders of magnitude as described in section 2.7.2 . Kotliar *et al.* (Kotliar et al. 2011) measured rPWV in healthy humans for the first time, reporting values of 21.5 mm/s in young and 243.8 mm/s in old people. Two years later, they demonstrated rPWV in hypertensive subjects (1.2 mm/s) was higher than high-normals (0.8 mm/s) and normotensive subjects (0.4 mm/s) (Kotliar et al. 2013). The two studies show a difference of a factor of up to 100 in values of rPWV. Golzan *et al.* (Golzan, Butlin, et al. 2014) measured rPWV in the rat eye at a value of 114 mm/s. Spahr *et al.* (Spahr et al. 2015) used swept-source optical coherence tomography (OCT) to capture retinal pulsations from surrounding tissue motions and reported rPWV as 620 mm/s in a healthy subject. The most recent study using spectral-domain OCT in 2017 quantified rPWV in a young normotensive subject in the order of 20-30 mm/s. The large difference among the reported rPWV values implies that current measurements of PTT in retinal arteries are not equivalent and results depend on the imaging modalities used. As a means to predict

rPWV, by measuring elastic modulus and vessel geometry (wall thickness and vessel diameter) the order of magnitude of rPWV can be determined using the Moens-Korteweg equation. This requires *ex-vivo* analysis of the retinal arteries and this has been attempted in Chapter 7 of this thesis. Furthermore, PTT measurements were validated by investigating their pressure dependency as presented in Chapter 5 of this thesis.

Chapter 4

Pulse diameters in normotensive and hypertensive rats

Published as:

Rezaeian M, Georgevsky D, Golzan SM, Graham SL. High speed *in-vivo* imaging of retinal hemodynamics in a rodent model of hypertension. *Conf Proc IEEE Eng Med Biol Soc.* 2016 Aug; 2016:3243-3246.

Abstract

The eye is the only organ through which micro-circulation can be visualized non-invasively. This unique feature makes the eye and specifically retinal vasculature an excellent target area to monitor and study micro-vascular damage in systemic diseases. Dynamic (real-time) changes of retinal vessels have been shown to be more specific to the disease in comparison with static measurements. The hypothesis of the present study is that hypertension causes changes in retinal vessels and we can non-invasively quantify these changes. In this study we utilize high speed imaging (i.e. 125 fps) to study and derive dynamic changes of retinal

vessels in a rat model of hypertension. The Eulerian video magnification algorithm was used to extract retinal arterial and venous pulse amplitude from five Spontaneously Hypertensive Rats (SHR) and five Wister Kyoto (WKY) rats were used as the control group. Results showed that retinal arterial diameter and pulse amplitude are significantly lower in the SHRs compared with WKYs. Dynamic biomarkers of retinal micro-vasculature may be used as a diagnostic tool for systemic diseases.

4.1 Introduction

Techniques for *in-vivo* measurement of microcirculation changes in cardiovascular disease (CVD) are not well established. This is mainly due to the fact that most of the current investigation techniques are invasive and consequently their application is limited to acute conditions. Non-invasive *in-vivo* monitoring of microcirculation is possible through retinal imaging. This unique accessibility allows direct, repeatable and reproducible measurements by means of advanced imaging techniques. Several studies have established links between retinal microcirculation measures and different diseases including hypertension (Cheung, Ikram, et al. 2012), glaucoma (Okuno et al. 2004), diabetes (Sabanayagam et al. 2015) and dementia (Chang et al. 2014).

Hypertension is one of the most prevalent risk factors for cardiovascular disease. It mainly affects small arteries and its impact has recently become discernible in retinal artery pulse wave characteristics (Kotliar et al. 2013). Ocular manifestations of hypertension include clinical hypertensive retinopathy (Wong et al. 2005) with retinal vascular narrowing (Ding et al. 2014), haemorrhages and other morphological changes (Wong et al. 2007). In comparison to other risk factors, retinal vessel diameter changes provides additional pathogenesis and prognosis information (Lim et al. 2013). Furthermore, it correlates with other aetiologies like

Alzheimer's disease (Frost et al. 2013; Feki et al. 2015) and diabetes (Ikram, Cheung, et al. 2013).

Assessment of retinal vessel diameter changes requires accurate fundus imaging. Vessel analysis approaches are divided into two categories: static methods are based on a single image while dynamic methods analyse an image sequence. Dynamic analysis offers the possibility of vascular function assessment over time which may provide additional information about the state of the vasculature in disease (Kotliar et al. 2008; Kotliar et al. 2013; Kotliar et al. 2011). The majority of previous studies on *in-vivo* retinal vascular changes have been performed in humans using the Dynamic Vessel Analyzer (DVA). Cheung *et al.* (Cheung, Ikram, et al. 2012) have summarized different retinal microvascular indices relating to hypertension. Lim *et al.* (Lim et al. 2013) have reviewed different research applications of DVA to assess endothelial dysfunction as a key contributor to CVD.

This study hypothesizes hypertension is associated with changes in retinal vessels. In the present study, we focus on retinal arterial and venous diameter and pulse amplitude in a rodent model of hypertension. Due to a higher heart rate in rodents and to avoid aliasing, a high-speed imaging device was used to capture real time retinal micro-circulation. Our lab has previously reported on the methodology used to extract retinal arterial and venous pulse amplitude and arterial pulse wave velocity in normal WKY rats (Golzan, Butlin, et al. 2014). Here, we present a more precise approach to extract such information and also to study these biomarkers in hypertension. These measurements will pave the way for further studies on utilizing retinal microcirculation for assessing changes in systemic diseases.

4.2 Methods

4.2.1 Animal preparation and video acquisition

A total of 10 male rats; (5 SHRs, 20 weeks and 5 WKYs, 20 weeks) were included in the study. All animals had a single dose injection of Urethane (1.3g/kg) for anaesthetics. Animals were placed in front of a Zeiss ff450 fundus camera at a distance of 13 mm. A high-speed camera (Optronis, Germany) was mounted on top of the Zeiss fundus camera. The left pupil of the animals was dilated using 1% Tropicamide. A 10-second recording of the retina at 125 frames per second (10 fps) with a 20° field of view at a resolution of 1024×768 pixels was captured. Electrocardiogram (ECG) signal was also recorded simultaneously. The study was approved by Macquarie University's Animal Ethics committee.

4.2.2 Video Analysis

Figure 4.1 depicts the block diagram for video analysis. It includes three pre-processing steps to improve the quality of the images before the measurement of vessel diameters. A total of six separate steps have been applied to each video with details of each step described in the following.

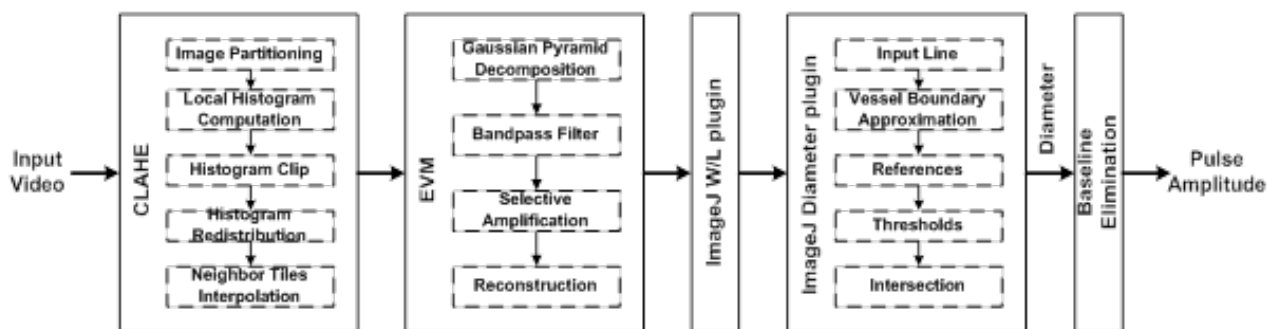


Figure 4.1. The block diagram of the proposed method for the measurement of retinal vessels pulsations. The algorithm is composed of intensity enhancement using CLAHE followed by EVM for motion magnification. Next, a small window around the vessel of interest is binarized using ImageJ W/L plugin and using ImageJ diameter plugin the diameter at a given cross-section of the vessel is measured in the full stack. This gives a signal representing diameter changes over time. Finally, the linear trend of the signal is removed.

Contrast Limited Adaptive Histogram Equalization

One challenge associated with high speed imaging is illumination. The obtained videos are dark and dim. In the first step of the image enhancement procedure, an adaptive intensity adjustment algorithm is applied to the videos. The algorithm works based on a localized histogram equalization. Unlike ordinary static histogram equalization techniques, which operate on the entire image, adaptive algorithms function on small regions or tiles to redistribute the intensity values of the image. To eliminate artificially induced edges and simultaneously improve computational efficiency, adjacent tiles are combined by means of interpolation. In addition, a contrast limit is set to prevent the over-amplification of noise in homogeneous regions. A representative result of CLAHE is illustrated in **Figure 4.2**.

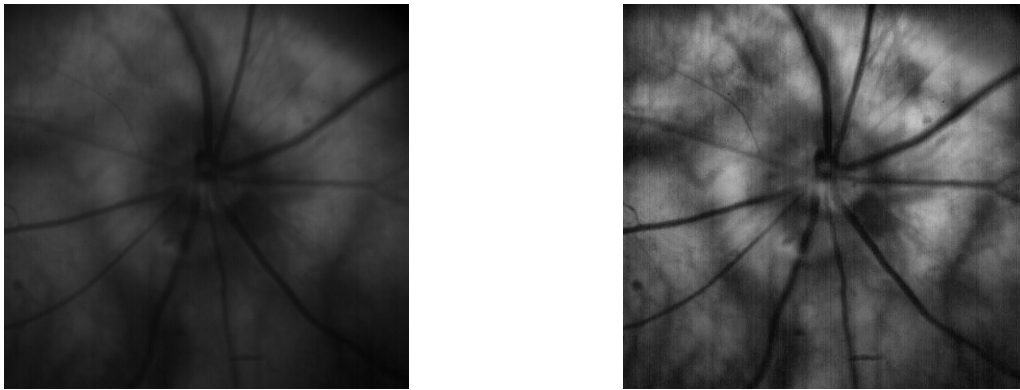


Figure 4.2. The original image (left) and the result of CLAHE (right). The contrast between the vessels boundaries and the background has been enhanced by CLAHE.

Eulerian Video Magnification

In order to magnify subtle vessel pulsations, Eulerian Video Magnification (EVM) algorithm (Wu et al. 2012) was applied to the video sequences. It decomposes every frame of the input video to several spatial frequency bands using Gaussian pyramid and then applies an ideal bandpass filter with a passband from 0.1 to 10 Hz to all bands. The cut-off frequencies are selected based on typical beat-rate of rats which is almost 5 Hz. The filtered bands are then amplified to boost vessel pulsations. Different frequency bands may be amplified differently based on an initial amplification factor, α , and a spatial cutoff frequency, λ_c , set by the user.

Frequency components beyond λ_c are set to zero. The amplified bands are then added to the original image to reconstruct the magnified output. The following shows the mathematical basis of the process in 1D. The generalization to 2D is straightforward.

If $I(x, t)$ denotes the input signal at spatial position x and time t it can be expressed in terms of a displacement function $\delta(t)$ as:

$$I(x, t) = f(x + \delta(t)) \quad \text{Equation 4-1}$$

According to the first-order Taylor series expansion about x , $I(x, t)$ can be approximated as:

$$I(x, t) = f(x) + \delta(t) \frac{\partial f(x)}{\partial x} \quad \text{Equation 4-2}$$

Let $\delta_k(t)$ denote k th temporal spectral component of $\delta(t)$. Then

$$\delta(t) = \sum_k \delta_k(t) \quad \text{Equation 4-3}$$

The filter passes all components of $I(x, t)$ except $f(x)$ in Equation 4-2 and applies an attenuation factor γ_k to each sub-band $\delta_k(t)$. So, the output of the filter is:

$$B(x, t) = \sum_k \gamma_k \delta_k(t) \frac{\partial f(x)}{\partial x} \quad \text{Equation 4-4}$$

After boosting by α and adding the original signal,

$$\tilde{I}(x, t) = I(x, t) + \alpha \sum_k \gamma_k \delta_k(t) \frac{\partial f(x)}{\partial x} \quad \text{Equation 4-5}$$

Combining Equation 4-2, Equation 4-3, and Equation 4-5 we have

$$\tilde{I}(x, t) = f(x) + \sum_k (1 + \alpha \gamma_k) \delta_k(t) \frac{\partial f(x)}{\partial x} \quad \text{Equation 4-6}$$

Let $\alpha_k = \alpha\gamma_k$ then,

$$\tilde{I}(x, t) = f(x) + \sum_k (1 + \alpha_k) \delta_k(t) \frac{\partial f(x)}{\partial x} \quad \text{Equation 4-7}$$

According to the first-order Taylor series expansion

$$\tilde{I}(x, t) = f(x + \sum_k (1 + \alpha_k) \delta_k(t)) \quad \text{Equation 4-8}$$

This reflects a frequency-dependent motion magnification. More details about the algorithm can be found in the study by Wu *et al* (Wu et al. 2012).

Contrast Enhancement

In the final step of the pre-processing, we used ImageJ Window/Level (W/L) adjustment plugin to enhance the contrast of the vessels against the background. This plugin allows the user to change the maximum and minimum intensity of the whole image or only a region of interest. A sample result has been shown in **Figure 4.3**.

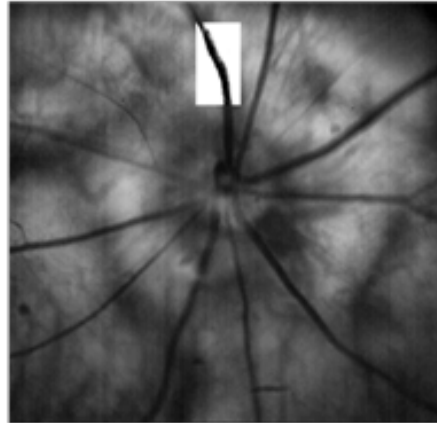


Figure 4.3. Local contrast enhancement using ImageJ W/L plugin. The vessel segment is binarized for further diameter measurement.

Diameter Measurement

We used ImageJ Diameter plugin (Fischer et al. 2010) to measure retinal vessels diameter changes. The algorithm initiates with an input line drawn by the user crossing the vessel. It

extracts the intensity profile of the image along the line. Based on the maximum intensity difference along the line, a primary estimation of the vessel boundary is computed. Using the two boundary estimates on each side, the intensity profile is divided into three areas: two reference intensities representing the lightest areas outside the vessel at each side and one intensity reference for the darkest area within the vessel. The average of the successive reference pairs gives two thresholds. Finally, the intersection of the line crossing pixels next to the boundary estimates with the resulting thresholds determines the vessel boundary and consequently vessel diameter. The algorithm repeats the measurements for two parallel lines shifted by one or two pixels on each side of the line drawn by the user. We averaged the measurements over five trials.

Pulse Amplitude

Applying the procedure to every consecutive frame gives vessel diameter changes over time. The amplitude of the pulsations is then computed as peak minus trough after filtering the baseline of the diameter waveform (**Figure 4.4**).

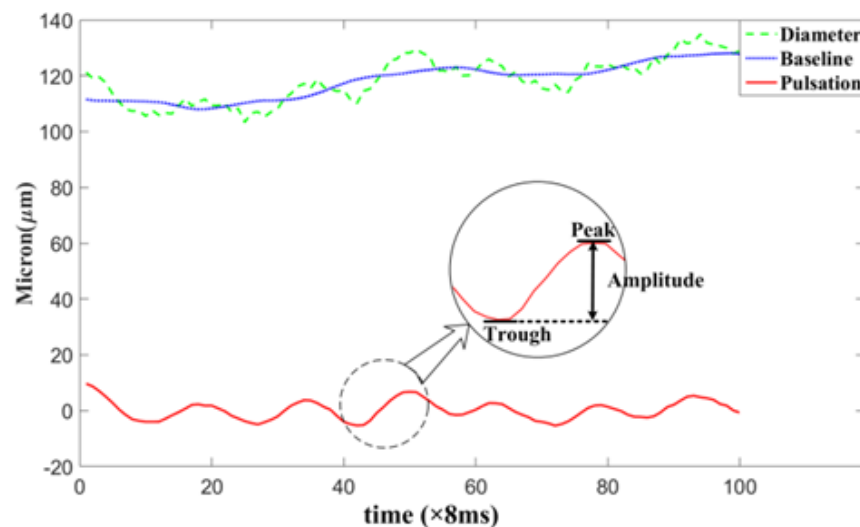


Figure 4.4. Baseline elimination. The linear trend of the diameter waveform displayed with dashed green line is shown in blue. The output signal after detrending is shown in red.

Calibration

To calibrate pixels to metric dimension, a graticule was placed at a distance of 13 mm in front of the Zeiss fundus camera (i.e. same location of animal eyes). The recorded image was then used to calibrate the number of pixels in 1mm. We observed that 165 pixels equalled to 1mm.

4.3 Results and discussion

For each rat, venular and arterial diameters were measured each at two sites. The proximal and distal sites were selected approximately one and three optic disk diameter away from the disk margin (Figure 4.5).

Table 4.1 summarizes the results of diameter and pulse amplitude measurements in hypertensive and normotensive rats. In addition, pulse amplitude drop ratio along both vein and artery is presented. It is computed as the pulse amplitude drop between proximal and distal points normalized by distance.

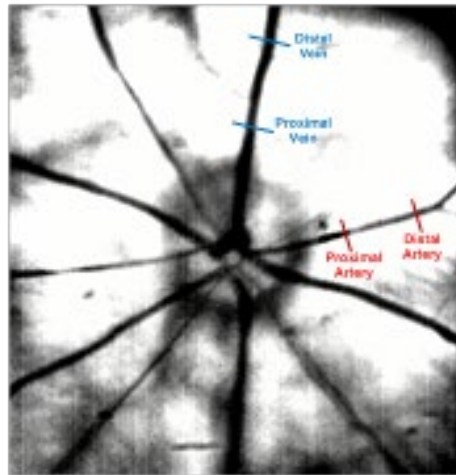


Figure 4.5. Proximal and distal sites along artery and vein. For the purpose of drop ratio measurement, both arterial and venular diameter are measured at two sites with a given distance along the vessel.

Table 4.1. Results (measurements are in Micron). Venous and arterial diameter at two sites, one and three optic disc diameter away from the optic disc rim are compared between SHR and WKY rats. Pulse amplitude and drop ratio are presented as well.

Rat	Vein					Artery				
	Diameter Prox ^a (μm)	PA Prox (μm)	Diameter Dist (μm)	PA Dist (μm)	Drop Ratio ^b	Diameter Prox (μm)	PA Prox (μm)	Diameter Dist (μm)	PA Dist (μm)	Drop Ratio
SHR	94.5 \pm 7.5	9.0 \pm 1.3	81.0 \pm 11.9	9.0 \pm 1.3	0	61.9 \pm 9.5	10.0 \pm 0.62	56.8 \pm 10.3	6.0 \pm 1.3	-0.010
WKY	123.7 \pm 12.4	21.2 \pm 5.9	113.9 \pm 11.7	21.2 \pm 5.9	0	108.7 \pm 13.8	32.4 \pm 9.2	100.5 \pm 9.9	16.7 \pm 5.2	-0.037
P value ^c	0.07	0.08	0.08	0.08		<0.05	<0.05	<0.05	0.08	

a. Abbreviations: Prox, Proximal; Dist, Distal; PA, Pulse Amplitude.

b. Drop Ratio = $\frac{PA_{Dist} - PA_{Prox}}{Distance}$

c. P value obtained from a 2-tailed t-test

4.3.1 Retinal arterial and venous diameter

Although the average venous diameter was smaller in SHR rats, the difference did not register as statistically significant ($p = 0.08$). However, the average arterial diameter was significantly narrower in hypertensive rats ($p < 0.05$). Retinal arteriolar narrowing in hypertension has been evidenced in previous studies (McGowan et al. 2015; Wong et al. 2007; Mayet et al. 2003). This is consistent with increased vascular resistance due to vasoconstriction in response to high blood pressure. Moreover, this phenomenon can also be explained by reduced ocular perfusion in hypertension (Wong et al. 2007).

4.3.2 Pulse amplitude

The average venous pulse amplitude was non-significantly lower in SHR rats ($p = 0.08$). To check whether this non-significant result was due to a lack of statistical power, we conducted post hoc power analysis with alpha error level set at 0.05, two tailed. This showed us that the sample size would have to increase up to $N = 13$ in order for group differences to reach statistical significance at the 0.5 level. Thus, it is likely that our negative findings can be attributed to a limited sample size. The average arterial pulse amplitude was significantly smaller in this group ($p < 0.05$). Additionally, the venous diameter was larger than arterial diameter measured in the same distance from optic disc in each group ($p < 0.05$ in SHR group). However, this was not the case for pulse amplitude. As expected, we also observed

pulse amplitude attenuation along arteries. The pulse amplitude in the proximal site was larger compared with that in the distal site. In contrast, the amplitude of pulsation did not change along veins. One explanation for this is that unlike arteries in which the pulse initiates at one end, the venous flow feeds from several venules along the vein. The average arterial amplitude drop does not differ significantly between the two groups ($p = 0.92$).

4.3.3 Limitations

Limitations of this study include the small sample size and within-group variations. The latter can be attributed to blood pressure variation. However, blood pressure was assumed to stay relatively constant during the short recordings. In addition, amplifying retinal pulsations is an arbitrary procedure. Nevertheless, since we are only comparing the means of each group, this would have less effect on our results. SHRs truly develop hypertension from 10-12 weeks. Retinal recordings were taken at week 20th. We do not know if the retinal changes are due to acute blood pressure elevation or chronic hypertension.

This study shows the potential of dynamic analysis of retinal vessel characteristics as a non-invasive and potential biomarker that may be used in different systemic and ocular diseases. Due to a small sample size and cross-sectional nature of the experiments and also the interspecies variations, it is not possible to extract a cut-off value differentiating between the two groups. However, it would be our future scope. We are currently investigating pulse wave velocity (a marker for arterial stiffness) in retinal arteries in association with systemic cardiovascular abnormalities. Effects of blood pressure changes on retinal vasculature will also be considered in future studies and any association will be corrected for.

4.4 Conclusion

In this study we developed a novel method utilizing high speed imaging to extract dynamic properties of retinal hemodynamics *in-vivo* in a rodent model. We specifically derived retinal vessels diameter and pulse amplitude changes. We then applied the algorithm to examine the manifestations of hypertension in the rat eye. The results show significant reduction in arterial diameter and arterial pulse amplitude in hypertensive rats. Quantification of dynamic characteristics of retinal vessels pulsations would open new avenue for further research in a wide range of diseases. In our future study, we will investigate pulse wave velocity (a marker for arterial stiffness) as another potential biomarker for arterial stiffness.

Acknowledgment

This study was supported by grants from the Ophthalmic Research Institute of Australia (ORIA), Perpetual (Hillcrest Foundation) and Rebecca L Cooper medical foundation. M.Rezaiean is a recipient of a Macquarie Research Excellence Scholarship (MQRES).

Chapter 5

Pressure dependency of retinal arterial pulse wave velocity in the rat

Pulse wave velocity (PWV) in large arteries is a marker of arterial stiffness. Since arterial stiffness is pressure dependent, the experiment presented in this current chapter was directed with the aim of characterizing changes in retinal PWV with the alterations of blood pressure (BP) through active (vasoactive drugs) and passive (venous occlusion) means, the hypothesis being that retinal PWV measurement if accurate should change with BP. The results show retinal artery PWV increases with increasing BP as expected with changes in retinal artery stiffness.

5.1 Introduction

PWV is defined as the ratio of the length of a vessel segment (L) to the time taken for a pressure pulse to travel that length (called pulse transit time, PTT). According to the Water-Hammer equation (Vennin et al. 2015), in early systole when the effect of wave reflections is negligible, PWV is directly related to pressure with inverse proportion to the flow velocity (v) as per Equation 5-1.

$$PWV = \frac{P}{v\rho} \quad \text{Equation 5-1}$$

where $\rho = 1050 \text{ kg/m}^3$ is the density of blood. The basic Water-Hammer formula in Equation 5-1 results in relationships between wall parameters and PWV expressed as the Moens-Korteweg equation and pressure dependency of elastic modulus. The Moens-Korteweg equation relates PWV to the elastic properties of the vessel (assumed to be uniform and thin-walled) with dependency on vessel geometry and blood density as per follows:

$$PWV = \sqrt{\frac{Eh}{2r\rho}} \quad \text{Equation 5-2}$$

where E is the elastic modulus of vessel, h is vessel wall thickness, and r is vessel's radius. The elastic modulus E has been found to fit an exponential function of blood pressure (Wang et al. 2014):

$$E = E_0 e^{\alpha p} \quad \text{Equation 5-3}$$

where α is a constant, E_0 is elastic modulus at zero pressure, and p is blood pressure. Combining the two equations shows PTT is related to BP exponentially:

$$PWV = \sqrt{\frac{E_0 e^{\alpha p} h}{2r\rho}} \quad \text{Equation 5-4}$$

With advancing age, the arterial tree gets stiffer due to calcification and elastin degeneration with the aortic vessel stiffening more with age than more distal arteries like the brachial or femoral artery (Avolio et al. 1983; Avolio et al. 1985). With stiffer vessels, the pressure wave propagates faster along the vessel which in turn causes the reflected wave to return faster. The early-arriving reflected wave augments the systolic peak of the pressure wave and is a contributor to the phenomena of isolated systolic hypertension (Nichols et al. 2008).

Butlin et al. (2015) showed that BP in rats can be changed using vasoactive substances (phenylephrine (PE) and sodium nitroprusside (SNP)) with an expected decrease in large artery (aortic) PTT and little to no direct drug effect on the aortic PWV. This current study replicates the same methodological procedure to investigate whether changes in BP reflect any changes in PTT in retinal arteries. Such a change would provide evidence that the measurement of retinal artery PTT is reflective of retinal artery stiffness as a representative of the stiffness of microvessels. BP was manipulated using SNP as a vasodilator and PE as a vasoconstrictor. To assure the effect is merely a result of the pressure change and drug-independent, BP was also decreased by reducing venous return through partial obstruction of the inferior vena cava.

5.2 Methods

5.2.1 Animal preparation

Experiments were performed on eight Sprague-Dawley rats (5 females, 3 males) aged twelve weeks with a total of eleven eyes analysed amongst the eight rats. Animals arrived at the age of 11 weeks and were allowed to adapt to the laboratory conditions for at least 1 week before commencement of the experiment. All experiments were conducted in accordance with the

Australian Code for the care and use of animals for scientific purposes and were approved by the Macquarie University Animal Ethics Committee.

Rats were anesthetized throughout the experiment with urethane (ethyl carbamate, 1.3 g/kg) administered intraperitoneally at the beginning of the experiment and intravenous urethane top-ups were administered as required. Rats were placed in a supine position on a heat mat regulated via a rectal temperature probe. Two femoral veins were cannulated for intravenous infusion of anaesthetic and vasoactive drugs. For the purpose of aortic PWV (aPWV) measurement, two 1.2-F solid state pressure catheters (Transonic Scisense) were placed in left carotid and femoral arteries after calibration. The tips of the catheters were advanced into the descending aorta. Pressure waveforms were monitored to ascertain proper location of transducers. Catheters and cannulas were fixed in place using sutures. The animal was then moved to the prone position. To obtain passive, drug-independent BP alteration, a suture was placed loosely around the inferior vena cava accessed via a right flank incision. The electrocardiogram (ECG) was monitored using lead II of a three-lead electrode configuration throughout the experiments. BP variations for each rat were compared to their own baseline which means the increase and decrease in levels were specified based on the baseline pressure for each rat. A 10-second retinal video recording at resting (90–110 mmHg) was taken as baseline in the beginning of each experiment.

5.2.2 Measurement of retinal artery diameter and PWV

The animal was placed prone on the microscope stage for eye imaging. The pupil was dilated by a single drop of 0.5% tropicamide (Alcon, Fort Worth, Texas, USA). Gen Teal moisturizing eye gel (0.3% Hypromellose ophthalmic gel) was also applied to moisten and clarify the surface of the cornea. 0.9% saline (sodium chloride) solution was used as required during the experiment to hydrate and lubricate the eye.

Retinal images were recorded for further offline analysis using a high-speed camera (Optronis, Kehl, Germany) mounted on a Zeiss ff450^{Plus} fundus camera (Zeiss, Oberkochen, Germany) at a rate of 125 fps with a 30° field of view at a resolution of 1280×1024 pixels. Retinal artery diameter waveforms at proximal and distal sites were obtained using an in-house algorithm written in MATLAB® (The MathWorks Inc., Natick, MA, USA). Details about the method are provided in Chapter 3. Proximal and distal sites were selected along a straight segment of an artery approximately 420 µm apart. Where possible, for consistency, the measurements across animals were made on the same vessel location. In eight out of eleven eyes, vessel diameter changes were taken in the superior nasal quadrant of the fundus and within one to three optic disc diameter from the optic disc rim. In the remaining three eyes, measurements were made in the superior temporal part. PTT was calculated as the slope of the regression line of phase delays on angular frequencies obtained from the Fourier components of the diameter signal. Fourier analysis was performed on the whole duration of diameter waveforms (i.e. 10 seconds for the baseline and 40 seconds for each episode of BP manipulation) to obtain a higher frequency resolution and consequently more precise time delay measurements. The regression was calculated only for the frequency components between 4 to 6 Hz representing the heart rate of rats.

5.2.3 Alteration of BP

Retinal recordings were acquired across a physiological range of BP by changing it both through vasoactive substances and through a passive mechanism. 40-second-long retinal recordings were obtained during the time of BP return to the baseline at each of the following episodes:

- 130 mmHg to baseline following systemic PE infusion;

- 130 mmHg to baseline during PE infusion with simultaneous inferior vena cava occlusion (this episode is referred as PEVO from now);
- 70 mmHg to baseline following systemic SNP;
- and 70 mmHg to baseline following venous occlusion (VO).

BP was increased by intravenous infusion of PE (30 $\mu\text{g/kg/min}$). PE is a α_1 -adrenoceptor agonist which binds to α -receptors on vascular smooth muscle and increases blood pressure by inducing vasoconstriction. Active reduction in BP was obtained by infusion of SNP (30 $\mu\text{g/kg/min}$) which mediates vasodilation by releasing nitric oxide (NO). Partial occlusion of the inferior vena cava was also adopted to lower BP passively through reducing venous return. Figure 5.1 shows examples of the BP and aortic PWV (aPWV) changes with vasoactive drug infusion and VO.

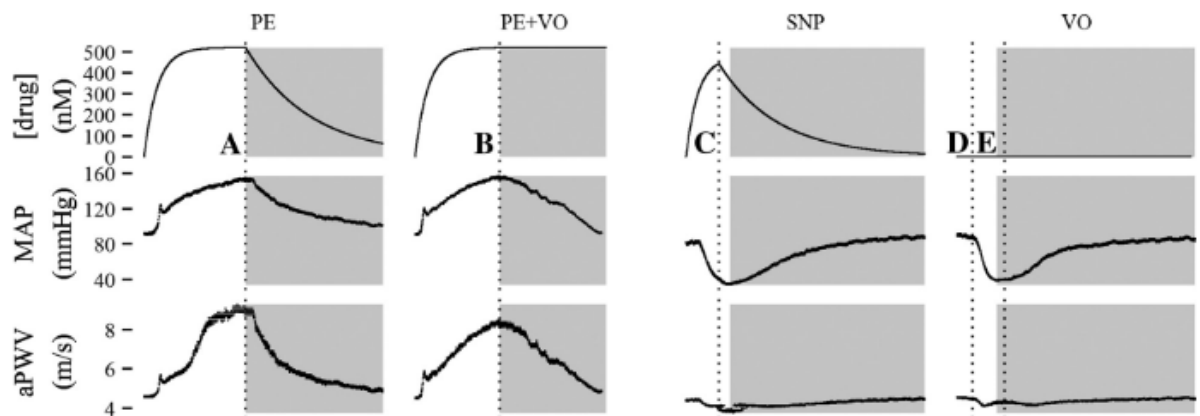


Figure 5.1. Illustration of BP manipulation procedure. An example of MAP and aPWV alterations with infusion of the vasoactive drugs (PE/SNP) and the use of venous occlusion (VO) for a passive reduction in arterial blood pressure. The shaded region indicates when retinal recordings were taken (peak or trough of MAP returning to the baseline). The top row gives the calculated in vivo concentration of vasoactive drug. A: end of PE infusion. B: venous occlusion while continuing to infuse PE. C: end of infusion of SNP. D: start of venous occlusion. E: start of gradual decrease in venous occlusion. (modified from (Butlin et al. 2015)).

5.2.4 Measurement of aPWV

Mean arterial pressure (MAP), systolic blood pressure (SBP), diastolic blood pressure (DBP), heart rate (HR), and aortic PWV (aPWV) were extracted from ECG, thoracic, and abdominal pressure waveform using a custom Spike2 (Version 7.09, CED) script. PTT was calculated as the foot-to-foot time interval between the thoracic and abdominal pressure waves. The foot of the signals was located using the peak of the second derivative of the pressure waveforms. The distance between the sensors was measured at autopsy directly along the aorta.

5.3 Results

Blood pressure was raised from baseline to 130 mmHg through infusion of PE and dropped to 70 mmHg with either SNP infusion or VO. Figure 5.2 shows a representative retinal arterial diameter waveform. The diameter signal exhibits power at the cardiac frequency.

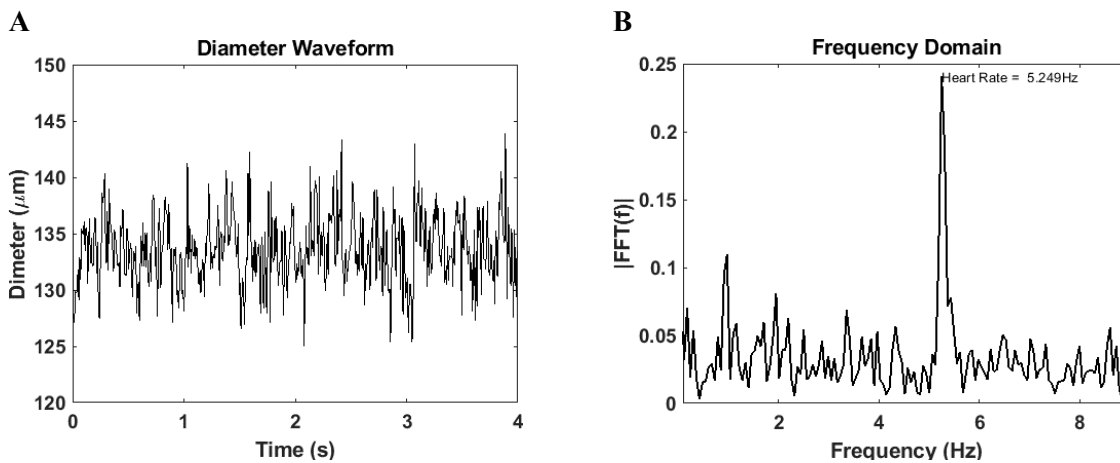


Figure 5.2. Retinal arterial diameter waveform (A) have power at cardiac frequency (B).

Figure 5.3 gives the relationship between aortic MAP and rPWV. Linear, quadratic, and exponential regression curve fits were calculated. rPWV increased with increasing pressure. The relationship follows an exponential trend (**Table 5.1**).

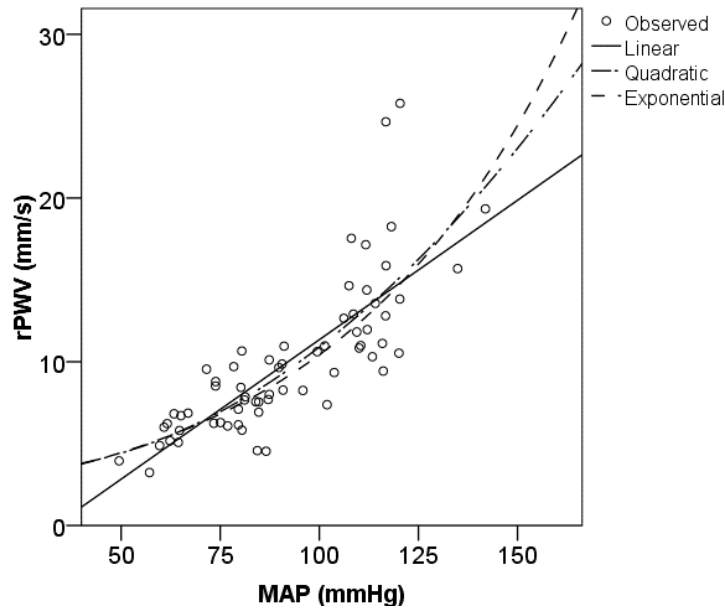


Figure 5.3. Retinal arterial PWV increases exponentially with increasing blood pressure as $rPWV = 0.002 \times e^{0.018 \times MAP}$.

Table 5.1. Model summary and parameter estimates of rPWV as a function of MAP.

Dependent Variable: rPWV, Predictor: MAP

Equation	Model Summary			Parameter Estimates		
	R Square	F	Sig.	c	b1	b2
Linear	.625	104.927	<0.001	-5.687	.170	
Quadratic	.639	54.770	<0.001	3.595	-.040	.001
Exponential	.706	150.973	<0.001	1.899	.017	

Although there was a slight increase in rPWV sensitivity to SBP compared with DBP (indicated as the exponent of the exponential model; Figure 5.4, Table 5.2), there was no statistically significant difference among DBP, SBP and MAP as determined by one-way ANOVA test on the exponents of the exponential fits ($F = 0.376$, $p = 0.694$). The normality of each variable was evaluated and determined to be satisfied by Shapiro-Wilk test and as the z-score for both the skewness and kurtosis of the distributions were within ± 1.96 .

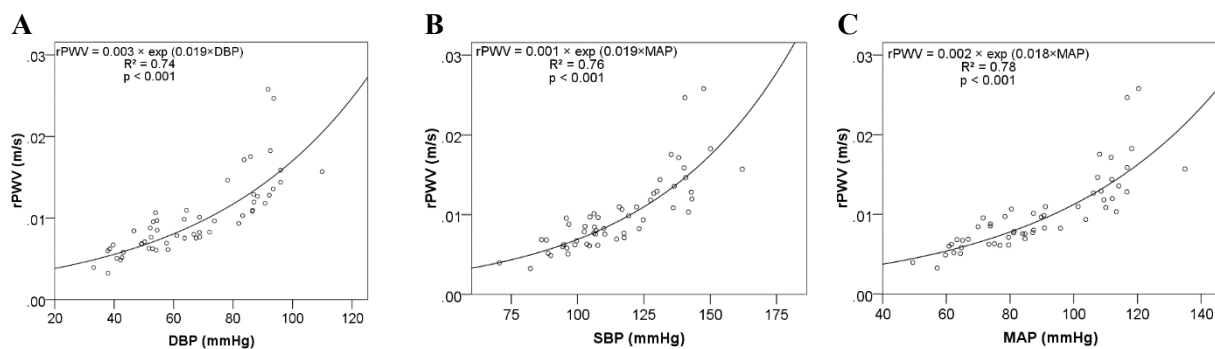


Figure 5.4. Comparison between rPWV sensitivity to DBP (A), SBP (B), MAP (C)

Table 5.2. Coefficients of the exponential model: $rPWV = c \times e^{b \times \text{Variable}}$

Variable	c	b	R ²	p	N
DBP	0.003	0.019	0.743	< 0.001	54
SBP	0.001	0.019	0.758	< 0.001	54
MAP	0.002	0.018	0.782	< 0.001	54

ANOVA analysis of rPWV pressure sensitivity yielded significant variation among the mode of pressure manipulation, i.e. type of drug infusion or VO ($F = 13.579$, $p = 0.002$). The pressure sensitivity of rPWV showed an increase with increasing blood pressure. A post hoc Tukey test (Table 5.3) showed that pressure sensitivity of rPWV during PE infusion and PE infusion with VO differed significantly from that during vasoactive pressure drop with SNP infusion. rPWV was higher at higher blood pressure, as shown by results during PE infusion (12.7 mm/s, 105 mmHg) differing from results during SNP infusion (7.33 mm/s, 76 mmHg).

Table 5.3. Tukey's Honest Significant Difference (HSD) test comparing pressure sensitivity of rPWV to blood pressure during each episode

(I) group	(J) group	Mean Difference (I-J)	Std. Error	Sig.	95% Confidence Interval	
					Lower Bound	Upper Bound
PE	PEVO	.000	.002	1.000	-.00658	.00658
	SNP	.011*	.002	.003	.00442	.01758
	VO	.006	.002	.059	-.00025	.01291
PEVO	PE	.000	.002	1.000	-.00658	.00658
	SNP	.011*	.002	.003	.00442	.01758
	VO	.006	.002	.059	-.00025	.01291
SNP	PE	-.011*	.002	.003	-.01758	-.00442
	PEVO	-.011*	.002	.003	-.01758	-.00442
	VO	-.005	.002	.184	-.01125	.00191
VO	PE	-.006	.002	.059	-.01291	.00025
	PEVO	-.006	.002	.059	-.01291	.00025
	SNP	.005	.002	.184	-.00191	.01125

*. The mean difference is significant at the 0.05 level.

However, there was no difference between PE and VO, nor PEVO and VO ($p = 0.059$). This can be explained considering that MAP levels were higher ($+12 \pm 10$ mmHg) as reduced with inferior vena cava occlusion (88 ± 17 mmHg) compared to SNP infusion (75.18 ± 10.65 mmHg) ($p < 0.0005$). MAP increased significantly following intravenous PE infusion (109 ± 21 mmHg) compared with SNP ($p < 0.0001$) and VO ($p < 0.022$). MAP rise ensuing PE infusion with vena cava occlusion (102 ± 20 mmHg) was also significant in comparison with SNP ($p < 0.003$). Although the average MAP during SNP infusion was greater than VO, the difference did not register as statistically significant ($p = 0.22$). There was no significant difference between either rPWV ($p = 1.000$) or MAP ($p = 0.737$) during PE and PEVO episodes. Figure 5.5 compares MAP levels obtained by either of the four methods.

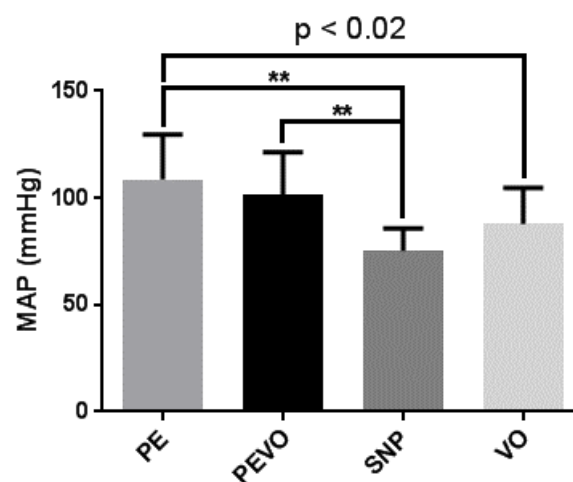


Figure 5.5. Manipulation of MAP by infusion of PE, SNP and the use of VO; ** $P < 0.01$

There were no statistically significant differences in either of MAP or rPWV between the SNP infusion and inferior vena cava occlusion. Comparison between rPWV in SNP and VO groups with univariate general linear model adjusted to MAP showed that there was no significant difference between the two groups ($-0.723 [-2.294 \ 0.848]$, $p = 0.350$, Partial Eta squared = 0.042). rPWV curves as a function of DBP, SBP, and MAP for each of the episodes are depicted in Figure 5.6. The coefficients for the exponential regression of rPWV on DBP, SBP and MAP ranges changed by PE, PEVO, SNP, and VO are listed in Table 5.4.

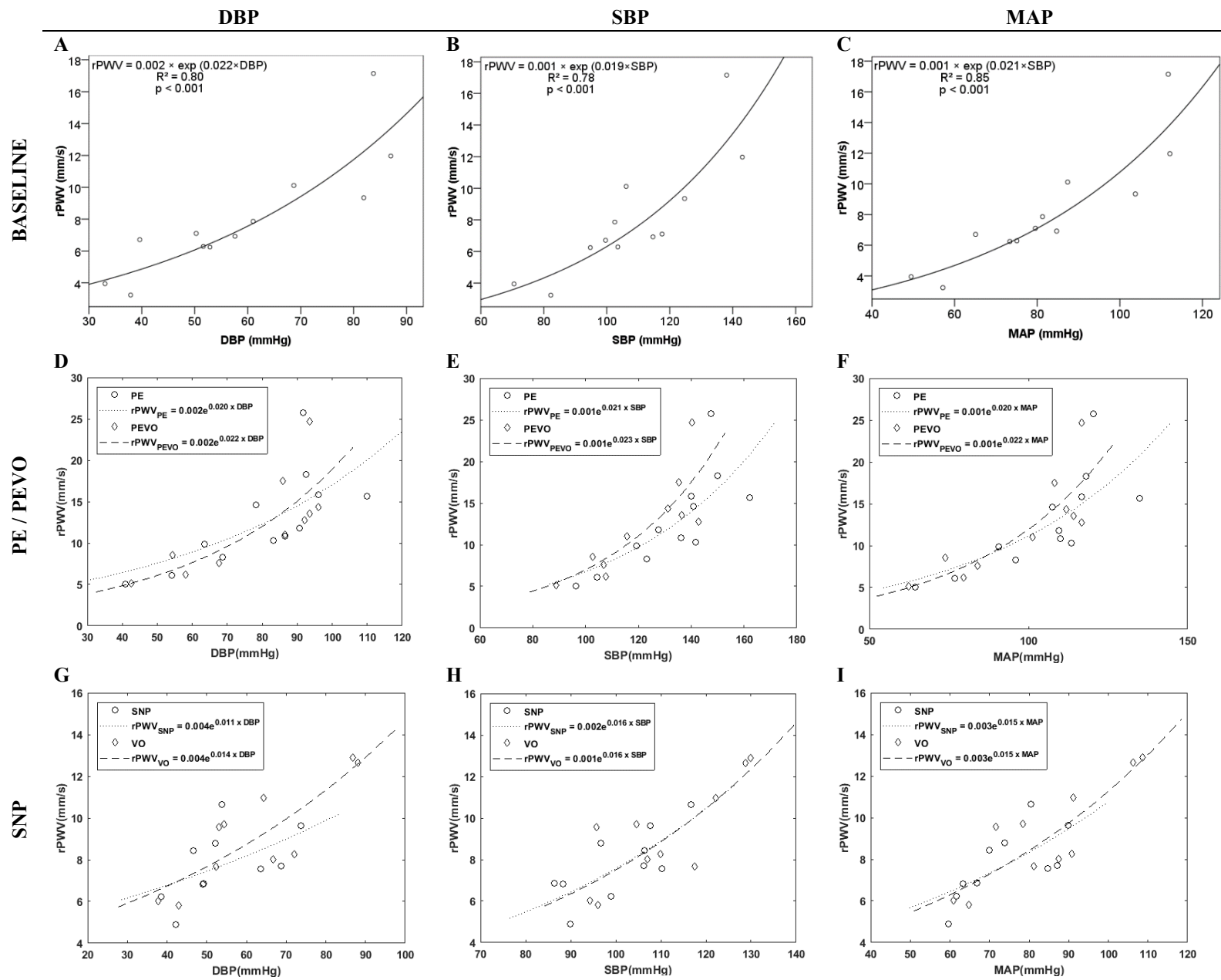


Figure 5.6. rPWV regression on DBP, SBP, and MAP at baseline, during vasoactive drug infusion, and venous return reduction

Table 5.4. Coefficients for exponential regression $rPWV = c \times e^{b \times \text{Variable}}$

	DBP				SBP				MAP			
	R²	p	b	c	R²	p	b	c	R²	p	b	c
PE	0.71	0.001	0.020	0.002	0.77	< 0.001	0.021	0.001	0.76	< 0.001	0.020	0.001
PEVO	0.76	0.001	0.022	0.002	0.81	< 0.001	0.023	0.001	0.80	< 0.001	0.022	0.001
SNP	0.31	0.092	0.011	0.004	0.51	0.020	0.016	0.002	0.52	0.020	0.015	0.003
VO	0.70	0.003	0.014	0.004	0.62	0.007	0.016	0.001	0.722	0.002	0.015	0.003

Analyzing all eyes together there was a positive correlation between rPWV and aPWV ($R^2 = 0.09$, $p = 0.03$; Figure 5.7 (A)). aPWV showed a positive correlation with MAP ($R^2 = 0.07$, $p = 0.05$) as expected. The correlation was far stronger for each individual eye. For 9 out of 11 eyes there was a statistically strong correlation between rPWV and aPWV ($R^2 = 0.88$, $p = 0.02$; Table 5.5). The difference was attributed to inter-animal variances. Once these differences were accounted for through the incorporation of random effects in a linear mixed model, a significant main effect of aPWV was found in rPWV ($R = 0.65$, $p < 0.0001$).

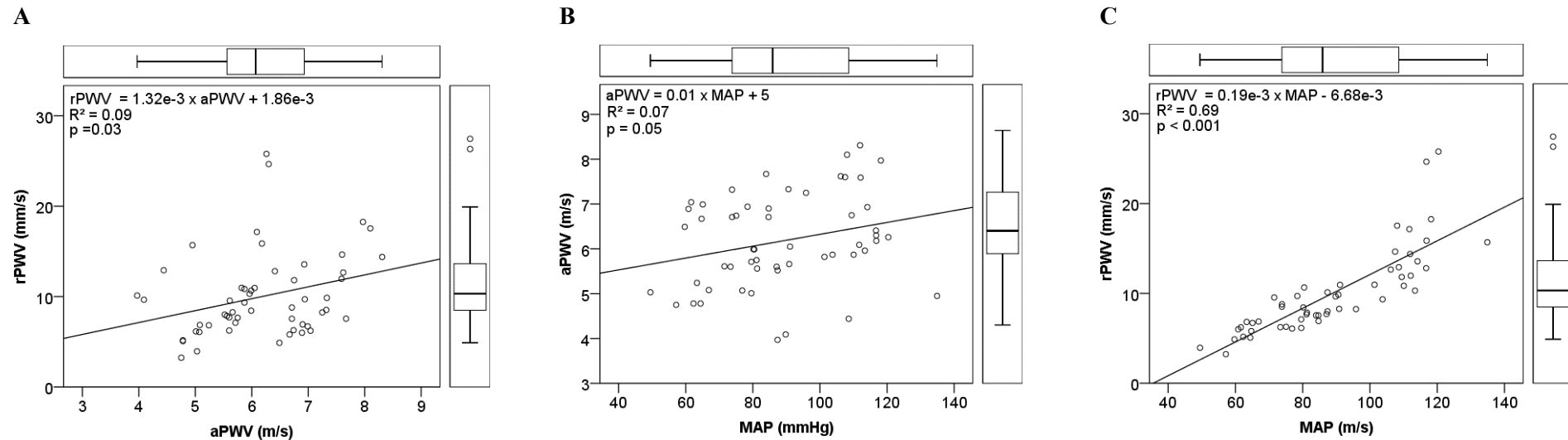


Figure 5.7. Linear regression of (A) rPWV on aPWV; (B) aPWV on MAP; and (C) rPWV on MAP.

Table 5.5. Coefficients for the linear regression $y = c + b \times \text{Variable}$

Eye #	rPWV on aPWV				aPWV on MAP				rPWV on MAP			
	R^2	p	$b (\times 10^{-3})$	$c (\times 10^{-3})$	R^2	p	b	c	R^2	p	$b (\times 10^{-3})$	$c (\times 10^{-3})$
1	0.895	0.015	7.891	-37.802	0.575	0.137	0.011	4.922	0.856	0.024	0.113	-1.337
2	0.933	0.008	51.670	-299.311	0.781	0.047	0.007	5.424	0.871	0.020	0.388	-22.526
3	0.920	0.010	7.274	-41.217	0.889	0.016	0.034	4.190	0.779	0.048	0.240	-10.186
4	0.746	0.059	2.408	-10.213	0.635	0.107	0.026	4.954	0.968	0.002	0.091	-0.365
5	0.877	0.019	7.798	-48.017	0.735	0.063	0.014	6.142	0.955	0.004	0.131	-1.770
6	0.962	0.019	6.245	-15.153	0.995	0.002	0.020	2.265	0.979	0.011	0.126	-1.155
7	0.704	0.075	5.465	-28.794	0.789	0.044	0.041	3.281	0.815	0.036	0.271	-15.888
8	0.002	0.972	0.300	3.575	0.026	0.896	0.002	4.843	0.986	0.076	0.078	0.182
9	0.711	0.361	8.740	-37.541	0.953	0.138	0.012	4.032	0.882	0.223	0.121	-3.302
10	0.932	0.008	3.501	-11.148	0.967	0.003	0.033	3.103	0.846	0.027	0.112	0.032
11	0.803	0.040	4.682	-17.166	0.977	0.001	0.020	3.792	0.832	0.031	0.094	0.332
Mean	0.771	0.144	9.634	-49.344	0.766	0.132	0.020	4.281	0.881	0.045	0.162	-5.296

5.4 Discussion

In this study the diameter changes of retinal vessels in response to BP changes was investigated in the rat eye. Utilizing high-speed imaging we were able to measure delay times between diameter pulses along retinal arteries. This investigation reveals new findings on instantaneous pressure dependency of rPWV and an association between rPWV and aPWV in the rats for the first time.

PWV in macro-vessels as a measure of arterial stiffness is highly correlated with BP (Avolio et al. 2015). However, very little has been published on arterial stiffness alterations in microvessels. The current study found a strong association between rPWV and BP. rPWV followed immediate BP changes showing an increase with increasing blood pressure. The relationship fitted an exponential model instead of a second-order polynomial as obtained in the aorta (Butlin et al. 2015). This can be attributed to the structural difference between the aorta and retinal vessels. With varying arterial wall properties, the effect of wave reflection and consequently PWV alters between proximal elastic and peripheral muscular arteries. Furthermore, intraocular pressure (IOP) might affect PWV in retinal arteries through alteration of effects of transmural pressure on wall stiffness (Zhi et al. 2012).

The pressure sensitivity of rPWV was greater at higher levels of BP similar to what observed in large arteries (Butlin et al. 2015). This was evidenced both as greater sensitivity of rPWV to SBP compared with DBP and when comparing pressure sensitivity of rPWV during PE/PEVO episodes with that during SNP/VO. Prior to this study the pressure dependency of rPWV was evidenced as compared between normotensive and hypertensive young subjects (Kotliar et al. 2013). The current study demonstrated instant effects of elevated BP on rPWV prior to irreversible structural damages in micro- and macro-vessels. Given the homology between retinal microvasculature and peripheral small resistant arteries, this novel observation is of interest in *in-vivo* non-invasive evaluation of microvascular changes associated with hypertension and arterial stiffness.

Furthermore, this study, for the first time reports a positive correlation between rPWV and aPWV in rodents. In the human carotid artery, there is an average change of 1 m/s for a change of pressure of 10 mmHg (Spronck et al. 2015). This current investigation on the rat showed an average increase of 1.9 mm/s in rPWV for a 10 mmHg increase in MAP compared to a rate of 0.1 m/s per 10 mmHg in the rat aorta. The rPWV therefore shows the expected directional change with change in MAP, and expected greater sensitivity at higher BP. Further implication is that the same level of increase in BP results in a more pronounced increase in rPWV than aPWV.

It is worth noting that in eye #8 no significant association between rPWV and aPWV as well as aPWV and MAP was found. However, since the experiment went as planned this eye was kept and analysed as part of the data. There were no animals excluded, although if this result had been excluded as an outlier it would have strengthened the relationship. One limitation of this study is that we were only able to measure average rPWV throughout each episode of BP manipulation. We tried dividing the 40-second time interval to shorter epochs to be able to obtain several measurements of PTT and consequently rPWV rather than a single average value. However, the regression of phase shifts on frequency was non-significant due to insufficient number of FFT samples.

The first attempt to measure PWV in the rat retina using a similar imaging modality in 2014 (Golzan, Butlin, et al. 2014) reported an average rPWV of 114 mm/s in Wistar-Kyoto rats and 98 mm/s in Sprague-Dawley rats which differ by one order of magnitude from current values. Later in 2016, an investigation on mouse retina by Song *et al.* using swept-source OCT concluded that a PWV of more than 1m/s is expected in the retinal arteries in rodents (Song et al. 2016). The discrepancy between reported values of rPWV (discussed in detail in Chapter 7 of this thesis) resulted in somewhat heated discussion between researchers in the field (Spahr et al. 2017; Q. Li et al. 2018). To estimate the theoretical value of rPWV, the effect of blood viscosity needs to be accounted for (see Chapter 7 of this thesis). Considering viscosity of blood, the properties of oscillatory flow including the wave propagation speed is characterised by a

non-dimensional α parameter which is related to the vessel radius (r), frequency of oscillation (ω), fluid density (ρ), and fluid viscosity (μ) as follows:

$$\alpha = r \sqrt{\frac{\omega \rho}{\mu}} \quad \text{Equation 5-5}$$

By taking into account the effect of α parameter for the oscillatory flow of a fluid with finite viscosity, lower PWV values by 1-2 orders of magnitude difference with PWV in large arteries are expected in vessels of size of retinal arteries (50-100 μm) (See Chapter 7).

This study provides new insights into modifications in the dynamic characteristics of retinal arteries secondary to BP alterations. The associations between rPWV and both BP and aPWV though expected based on physiological evidence, had not been corroborated before. Further research is required to establish the relationship in human vasculature and potential clinical applicability of these findings.

Chapter 6

Retinal vs central pulse wave velocity in the elderly

This chapter investigates the association between retinal pulse wave velocity (rPWV) and the PWV measured between carotid and femoral arteries (cPWV) as the gold-standard non-invasive measure of arterial stiffness.

6.1 Introduction

Stiffening of the arterial wall occurs following a reduction in vascular distensibility due to increased calcification and elastin degeneration (Harvey et al. 2015). Ageing and chronic high blood pressure contribute to increased arterial stiffness and vascular resistance. Arterial stiffness is recognized as a risk factor and prognostic index of several increasingly prevalent disorders including hypertension (Sun 2015), diabetes mellitus (Prenner et al. 2015), renal failure (Safar et al. 2004), inflammatory and pulmonary disorders (Vanfleteren et al. 2014), coronary artery disease (Ikonomidis et al. 2015), stroke (Chen et al. 2017), myocardial infarction, and angina pectoris (Vlachopoulos et al. 2014).

Central pulse wave velocity (cPWV), measured between carotid and femoral arteries as the simplest and most robust and reproducible non-invasive surrogate for aortic PWV is the gold-standard measure of arterial stiffness and has been adapted by the European Society of Hypertension (ESH) Guideline for the Management of the Hypertension as part of routine clinical investigation in the diagnosis and management of hypertension (Mancia et al. 2013). The concept was first introduced by Young in the early 19th century and later formulated as the Moens-Korteweg equation (Liberson et al. 2016). The equation models the velocity of the pressure wave in arteries as a function of the vessel size, blood density and elastic modulus.

There is a large body of evidence supporting the importance of cPWV in risk assessment, diagnosis, prognosis, and prediction of therapeutic efficacy of various disorders. cPWV is positively correlated with age and systolic blood pressure and negatively correlated with aortic diameter (Bailey et al. 2014). Elevated PWV has been associated with type 2 diabetes (Zhang et al. 2011) and cognitive decline (Zhong et al. 2014; Nilsson et al. 2014). However, since cPWV is measured as the ratio of distance to time delay between carotid and femoral blood pressure pulses, it does not reflect local arterial stiffness.

The microcirculation can be visualized directly through the retinal vasculature. This unique feature makes the retina an ideal window to study vascular-related pathogenesis. Changes in retinal vasculature and their relation to several systemic disorders have been reported in many earlier studies (Wong 2004; Ikram & Witteman 2006; Nguyen et al. 2007; Lim et al. 2013; Chang et al. 2014). Golzan *et al* introduced a method for non-invasive estimation of cerebrospinal fluid pressure (CSFp) using spontaneous retinal venous pulsation (SRVP) in conjunction with intraocular pressure (IOP) (Golzan et al. 2012). Jonas *et al* (Jonas et al. 2014) reported that raised CSFp induces retinal vasodilation in veins. Studies investigating static retinal vascular biomarkers of Alzheimer's disease (AD) have found vessel thinning, reduced tortuosity and branch density (Frost et al. 2013; Cheung et al. 2014). Golzan *et al* (Golzan, Orr, et al. 2014) observed increased amplitude of both venous and arterial pulses in AD patients. Vasoconstriction of retinal arteries in hypertension has been reported by several studies (Ding et al. 2014; Cheung, Ikram, et al. 2012). These all support the potential and effectiveness of retinal vascular biomarkers in screening early systemic disorders. However, studies of PWV in retinal arteries are scarce (Kotliar et al. 2011; Kotliar et al. 2013; Golzan, Butlin, et al. 2014; Spahr et al. 2015; Qian Li et al. 2018).

This chapter aims to determine the association between rPWV and cPWV in an elderly cohort. cPWV was measured using the SphygmoCor device (AtCor Medical, Sydney). Fundus image sequences were captured using the Dynamic Vessel Analyzer (DVA).

6.2 Methods

6.2.1 Subjects and Instruments

This study was performed in accordance with the guidelines of the Tenants of Helsinki. All subjects provided informed consent and the study was approved by Macquarie University Human Ethics committee.

37 elderly volunteers (28 females / 9 males, age: 78.9 ± 4.7 years) were tested at the Macquarie Eye Clinic, Sydney, Australia. Patients with a previous history of diabetes, or any other neurological or eye-related disorders particularly cataracts or glaucoma that might affect the results were excluded. 24 subjects were on medication for hypertension. IOP was measured using Goldman tonometry. Hypertension was determined by reported clinical diagnosis of hypertension and being on antihypertensive medication. Following this, a random eye was selected, and pupil dilated using a single drop of 1% tropicamide. A 60-second retinal video at a rate of 25 frames per second and a 30° field of view was then captured using the Dynamic Vessel Analyser (DVA) (IMEDOS, Germany). Patients were then asked to visit the Macquarie Heart Clinic for BP and cPWV measurements.

6.2.2 cPWV measurement

Sitting blood pressure (BP) was first measured with a digital sphygmomanometer after a five-minute rest. Measurements were repeated at least twice or until the difference between the readings was less than 5 mmHg. The average value of those measurements that were within 5 mmHg was used.

PWV is calculated as the ratio of the distance to the time taken for a wave to travel between two points. Common points for measuring cPWV as a marker of arterial stiffness are carotid and femoral arteries as they are easy to access and cover the region over aorta which is mostly affected by age-related stiffening. The SphygmoCor device (AtCor Medical, Australia) can measure the heart rate (HR), BP and cPWV noninvasively. Prior to measuring cPWV, brachial blood pressure was measured with the patient in supine position as cPWV was measured in this position too. Mean arterial blood pressure (MAP) was calculated as $1/3 \times \text{SBP} + 2/3 \times \text{DBP}$.

Femoral and carotid pressure waves were recorded in two steps. To record the femoral wave, a cuff was placed around the patient's thigh in the supine position. The carotid pressure wave was captured using a tonometer. SphygmoCor calculates carotid-femoral transit time using the foot-to-foot method. To obtain values for PWV, the user should enter three distances including carotid location to sternal notch, sternal notch to cuff and cuff to femoral location (**Figure 6.1**). Given these inputs, the software (Xcel version 7.01) calculates femoral-carotid distance. Each distance was measured in duplicate. Mean values were entered into the software. Two measurements of CPWV were taken from each subject with 5 minutes in supine position.

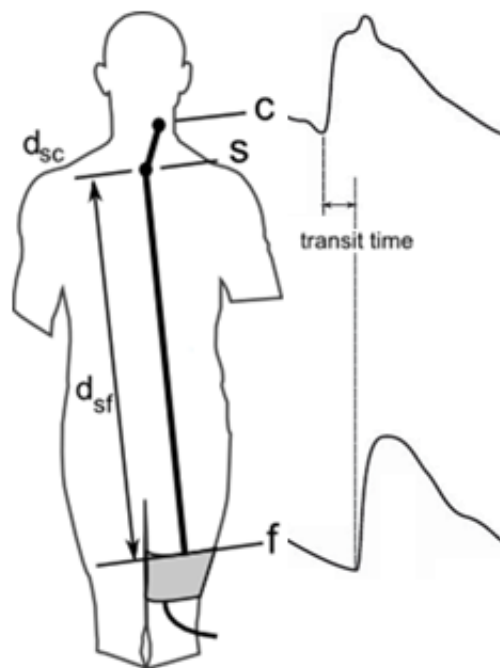


Figure 6.1. cPWV measurement. SphygmoCor carotid-femoral pulse wave velocity (cPWV) measurement simultaneously acquires a femoral pulse by volumetric displacement within a cuff around the upper thigh and a carotid pulse by applanation tonometry. The transit time is measured between the feet of the two waveforms. PWV distance is determined using the subtraction method by measuring the distance between the sternal notch to the top edge of the cuff, the site of the carotid tonometry from the sternal notch and to the top of the cuff. (modified from (Butlin et al. 2017))

6.2.3 Measurement of retinal pulse wave velocity (rPWV)

Retinal artery diameter waveforms at proximal and distal sites (610 μm away) were extracted using an in-house algorithm as described in Chapter 3. The pulse transit time (PTT) between

the two waveforms was computed as the slope of the regression line of phase shifts (computed by Fourier transform) on angular frequencies as shown in **Figure 6.2**.

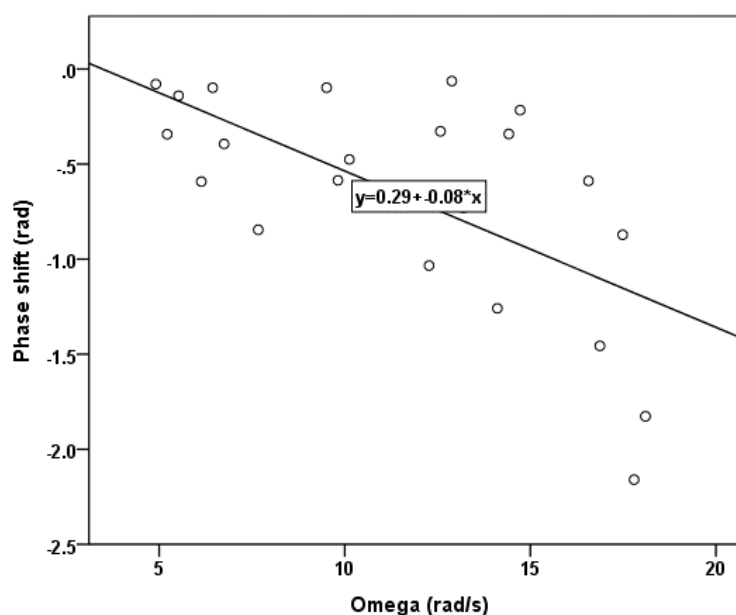


Figure 6.2. Calculation of PTT as the slope of the regression line of phase shifts on the angular frequency. The slope of the regression line estimates the transit time between the proximal and distal sites along a retinal artery

6.2.4 Statistical analysis

Statistical analysis was performed with Statistical Packages for the Social Sciences (SPSS; Version 22, Chicago, IL). Following test of normality of the study variables (systolic blood pressure (SBP), diastolic blood pressure (DBP), mean arterial pressure (MAP), IOP, and cPWV, these variables were compared between normal and hypertensive subjects using a MANOVA test. Next, in search of significant associations, a correlation matrix was produced using a step-wise liner regression with rPWV as the dependent variable and the rest of the variables as predictors. Finally, the association between rPWV and cPWV was investigated after corrections for confounders.

6.3 Results

Demographic characteristics and clinical data of the cohort including age, IOP, SBP, DBP, MAP, and cPWV are summarized in **Table 6.1**.

Table 6.1. Demographics of the normotensive and hypertensive subjects; (values presented as mean \pm standard deviation)

	Normotensive (n = 13)	Hypertensive (n = 24)	All Participants (n = 37)
Age (years)	78.5 \pm 5.3	79.2 \pm 4.5	78.9 \pm 4.7
Sex (female:male)	10:3	18:6	28:9
IOP (mmHg)	13.2 \pm 3.4	13.7 \pm 3.2	13.5 \pm 3.3
SBP (mmHg)	143.5 \pm 15.1	151.1 \pm 17.4	148.4 \pm 16.9
DBP (mmHg)	78.0 \pm 10.9	84.0 \pm 10.9	81.9 \pm 11.1
MAP (mmHg)	99.8 \pm 11.2	106.4 \pm 11.6	104.1 \pm 11.8
cPWV (m/s)	9.1 \pm 1.1	8.8 \pm 1.6	8.9 \pm 1.5

A comparison between normotensive participants and hypertensive subjects was performed for age, BP and IOP levels, and cPWV values using a MANOVA derived by combining all these variables together in a canonical variate. The null hypothesis that any of these variables is significantly different among the two groups was rejected (*Pillai's Trace* = 0.172, $F = 1.04$, $df = (6,30)$, $p = 0.420$).

displays results from independent-samples t -test with Bonferroni correction performed to compare each variable between the two groups. The distributions of the variables were sufficiently normal as verified by the Shapiro Wilk test and as the z values of the Skewness and Kurtosis indices were between -1.96 and +1.96. Furthermore, the homogeneity of variances was also verified by Levene's F test for all variables except cPWV (results listed in Table 6.2). Heteroscedastic t test was performed for comparing cPWV between the groups accordingly.

Table 6.2. Results of Levene's test for homoscedasticity and *t* test for comparing biometrics of normal and hypertensive subjects

Variable	Levene's Test for Equality of Variances		t-test for Equality of Means		
	F	<i>p</i>	T	df	<i>p</i> (2-tailed)
Age	0.111	0.742	-0.453	35	0.653
DBP	0.177	0.677	-1.602	35	0.118
SBP	0.172	0.681	-1.327	35	0.193
MAP	0.928	0.342	-1.654	35	0.107
IOP	0.386	0.539	-0.488	35	0.628
cPWV	4.636	0.038	0.699	35	0.489

The association between rPWV and either of MAP, age, IOP and cPWV variables in each group of participants was examined by a step-wise multiple linear regression. In normotensive subjects only cPWV showed a statistically significant correlation with rPWV ($p = 0.007$). In hypertensive subjects, further to cPWV ($p < 0.0001$), rPWV presented a significant negative correlation with IOP ($p = 0.021$). The correlation coefficients are listed in Table 6.3. No significant correlation was found between cPWV and either age or MAP.

Table 6.3. Correlation coefficients of rPWV with age, MAP, IOP, and cPWV in normotensive and hypertensive subjects obtained by a step-wise linear regression analysis

Group		rPWV	Age	MAP	IOP	cPWV	
Normal	Pearson Correlation	rPWV	1.000	.181	.146	-.215	.662
		Age	.181	1.000	.431	-.608	.272
		MAP	.146	.431	1.000	-.020	-.221
		IOP	-.215	-.608	-.020	1.000	-.244
		cPWV	.662	.272	-.221	-.244	1.000
	<i>p</i> value (1-tailed)	rPWV	.	.277	.317	.240	.007
		Age	.277	.	.071	.014	.184
		MAP	.317	.071	.	.474	.235
		IOP	.240	.014	.474	.	.211
		cPWV	.007	.184	.235	.211	.
Hypertensive	Pearson Correlation	rPWV	1.000	.047	.023	-.420	.903
		Age	.047	1.000	-.045	-.046	.192
		MAP	.023	-.045	1.000	.177	-.124
		IOP	-.420	-.046	.177	1.000	-.323
		cPWV	.903	.192	-.124	-.323	1.000
	<i>p</i> value (1-tailed)	rPWV	.	.413	.457	.021	.000
		Age	.413	.	.417	.416	.185
		MAP	.457	.417	.	.203	.282
		IOP	.021	.416	.203	.	.062
		cPWV	.000	.185	.282	.062	.

A linear regression was applied to study the association between rPWV and cPWV in each group. In normotensive subjects, the regression equation was as $rPWV = 8.24e^{-3} \times cPWV - 51.89e^{-3}$, with a goodness of fit (R^2) value of 0.44 ($p = 0.014$). For each 1 m/s increase in cPWV, there was an average increase of 8.24 mm/s in rPWV in this group. In the hypertensive group, predicted rPWV was equal to $rPWV = 9.24e^{-3} \times cPWV - 54.74e^{-3}$. The R^2 of the regression improved to 0.815 ($p < 0.001$) and the slope of the line increased to $9.24e^{-3}$ in this subset of participants. The scatter plots of rPWV vs. cPWV for each group is depicted in Figure 6.3.

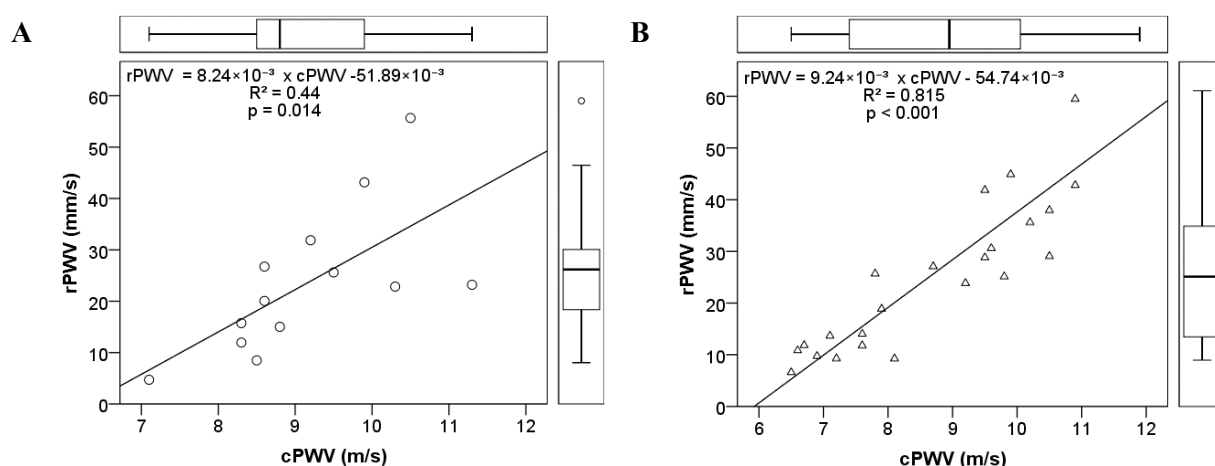


Figure 6.3. rPWV regression on cPWV in normal (A) and subjects on antihypertensive treatments (B)

The coefficients of the regression line of rPWV on cPWV in hypertensive volunteers were similar to those in the healthy ones. The comparison of rPWV between normotensive and hypertensive subjects was performed with a non-parametric independent samples test since the Shapiro-Wilk test indicated a non-normal distribution of rPWV ($p = 0.013$). A Mann-Whitney test showed no statistically significant difference in rPWV values between normotensive and hypertensive groups ($U = 141.00$, $p = 0.649$).

Since there was no evidence to support a significant difference among groups, both groups of subjects were pooled and analysed together. A pooled analysis of the data revealed a

significant positive correlation between rPWV and cPWV expressed as $rPWV = 8.79 e^{-3} \times cPWV - 52.94e^{-3}$ ($R^2 = 0.68, p < 0.001$) (Figure 6.4).

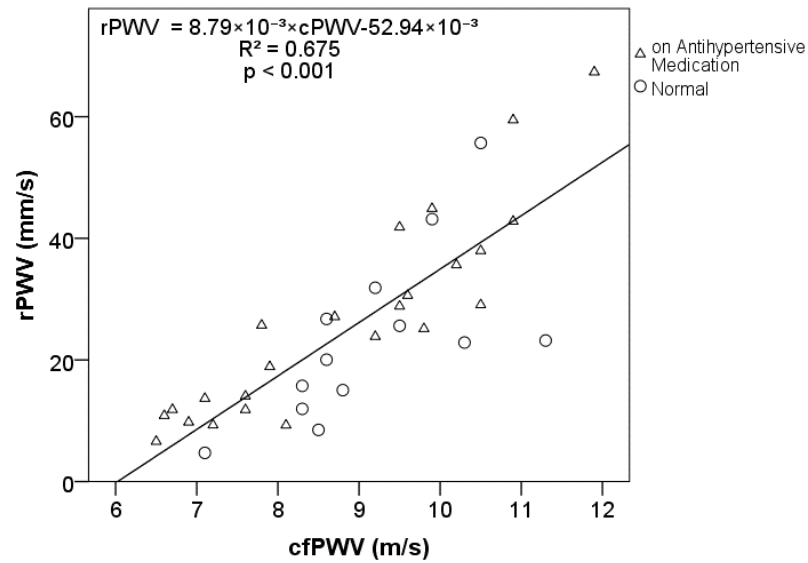


Figure 6.4. Regression model of rPWV based on cPWV; Normotensive and hypertensive objects were pooled together.

The effect of IOP on rPWV was also explored in the pooled data with a linear regression. The relationship was formulated as $rPWV = -1.62e^{-3} \times IOP + 47.4e^{-3}$ ($R^2 = 0.12, p = 0.038$) (Figure 6.5).

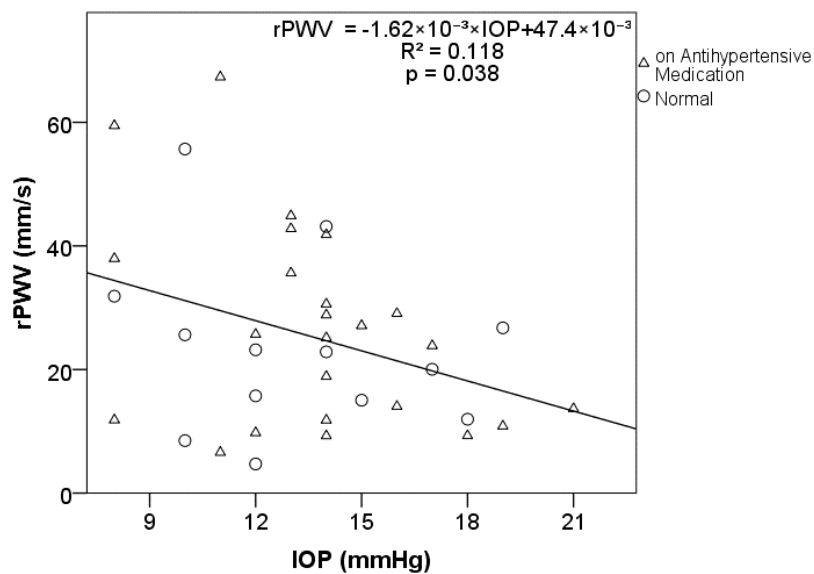


Figure 6.5. Estimation of the effect of IOP on rPWV with a linear regression

When calculated values of rPWV were corrected for IOP as a confounding factor, the regression equation to predict rPWV based on cPWV changed slightly as $rPWV = 7.68 \times 10^{-3} \times cPWV - 55.19 \times 10^{-3}$ ($R^2 = 0.59$, $p < 0.001$) (Figure 6.6). It is worth noting that correction for MAP is not needed as both rPWV and cPWV were measured at same BP in the same person.

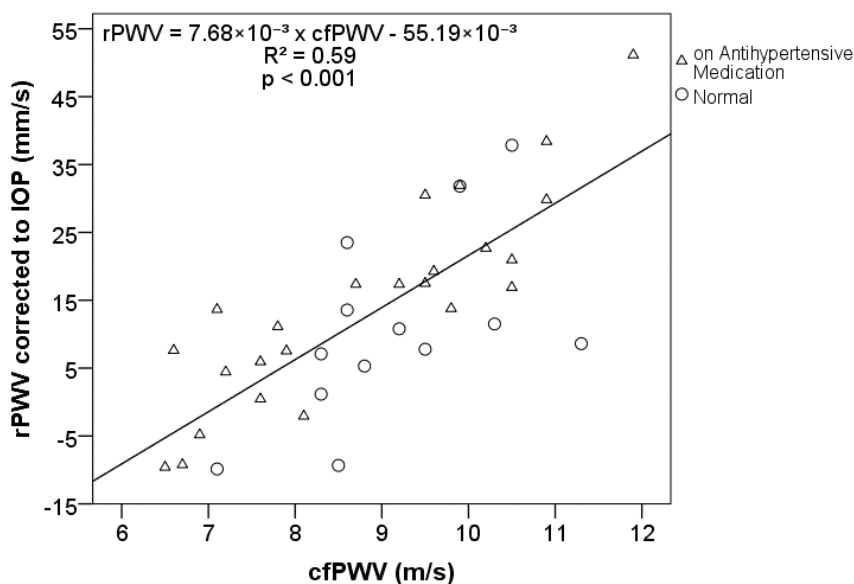


Figure 6.6. Regression model of rPWV based on cPWV after correction of confounding effect of IOP

Contrary to what was expected, no statistically significant correlation was found between cPWV and either age or MAP in either of the groups. However, a comparison of cPWV between subjects divided by 10-year age intervals (69-79 (75.6), and 80-89 (83.4)) showed an average increase of 0.9 m/s in cPWV for 10 years increment in age ($p = 0.03$).

Table 6.4 summarises the biometrics of the two age groups. Neither of BP values including SBP, DBP, and MAP were significantly different between the age groups. rPWV was marginally higher in the older individuals ($p = 0.07$) (Figure 6.7).

Table 6.4. Demographics of the subjects; (values presented as mean \pm standard deviation)

	69-79 (n = 21)	80-89 (n = 16)	<i>p</i>
Age (years)	75.6 \pm 3.0	83.4 \pm 2.1	< 0.001
Sex (female:male)	17:4	11:5	-
IOP (mmHg)	14.0 \pm 3.3	12.9 \pm 3.2	0.15
SBP (mmHg)	146 \pm 16	152 \pm 17	0.13
DBP (mmHg)	84 \pm 11	80 \pm 11	0.16
MAP (mmHg)	104 \pm 12	104 \pm 12	0.46
cPWV (m/s)	8.5 \pm 1.3	9.4 \pm 1.5	0.03
rPWV (mm/s)	22.2 \pm 14.8	29.7 \pm 15.7	0.07

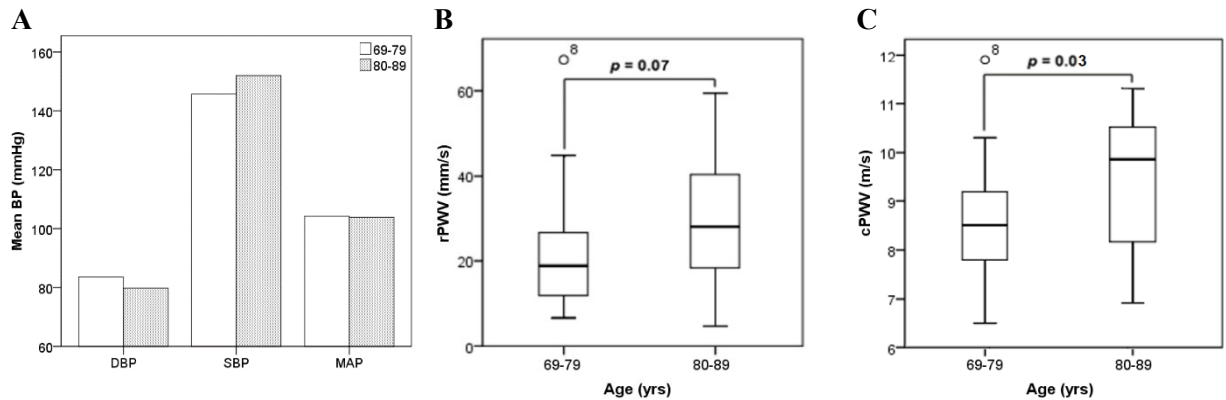


Figure 6.7. Comparison of (A) BP values including DBP, SBP, and MAP, (B) rPWV, and (C) cPWV between deciles of age

A stepwise multiple linear regression analysis of rPWV values corrected to IOP revealed a strong positive correlation between rPWV and both cPWV ($p < 0.001$) and DBP ($p = 0.013$) in the 69-79 age group. In the older group, only cPWV ($p = 0.001$) was correlated with rPWV. The correlation coefficients are listed in Table 6.5.

Table 6.5. Correlation coefficients of rPWV adjusted to IOP with age, DBP, SBP, MAP, and cPWV in two deciles of age obtained by a step-wise linear regression analysis

Group			rPWV	Age	DBP	SBP	MAP	cPWV
69-79	Pearson Correlation	rPWV	1.000	-.264	.484	-.060	.279	.789
		Age	-.264	1.000	.196	.153	.196	-.113
		DBP	.484	.196	1.000	.633	.932	.111
		SBP	-.060	.153	.633	1.000	.871	-.303
		MAP	.279	.196	.932	.871	1.000	-.072
		cPWV	.789	-.113	.111	-.303	-.072	1.000
	p value (1-tailed)	rPWV	.	.124	.013	.398	.110	.000
		Age	.124	.	.197	.254	.197	.313
		DBP	.013	.197	.	.001	.000	.316
		SBP	.398	.254	.001	.	.000	.091
		MAP	.110	.197	.000	.000	.	.379
		cPWV	.000	.313	.316	.091	.379	.
80-89	Pearson Correlation	rPWV	1.000	-.307	-.018	-.067	-.042	.719
		Age	-.307	1.000	.452	.399	.460	-.141
		DBP	-.018	.452	1.000	.731	.947	-.270
		SBP	-.067	.399	.731	1.000	.911	-.279
		MAP	-.042	.460	.947	.911	1.000	-.294
		cPWV	.719	-.141	-.270	-.279	-.294	1.000
	p value (1-tailed)	rPWV	.	.124	.474	.402	.438	.001
		DBP	.124	.	.039	.063	.036	.301
		SBP	.474	.039	.	.001	.000	.156
		Age	.402	.063	.001	.	.000	.148
		MAP	.438	.036	.000	.000	.	.135
		cPWV	.001	.301	.156	.148	.135	.

6.4 Discussion

The aim of the present study was to investigate if there is any association between rPWV as a measure of arterial stiffness in microvessels and cPWV measured between carotid and femoral arteries as the gold-standard non-invasive marker of arterial stiffness in large arteries. To the best of our knowledge, this is the first report on the association between PWV in micro- and macro-vessels. The study was conducted on elderly volunteers (age ranged between 69 and 89 years) and the results demonstrated a strong positive linear correlation between rPWV and cPWV in this cohort. The study population was a convenient sample as a demographic makeup of the glaucoma clinic where the data was collected. Hypertension was diagnosed by subjects' GP/cardiologist according to their medical history and/or based on use of antihypertensive medications. Those subjects were

not hypertensive were categorised as normotensive. However, according to the measurements the normotensive group was not perfectly a clean cohort we expected. The hypertensive patients had a marginally higher cPWV was not an expected finding given the SBP differences, but this may result from the classification of subjects as normotensive vs hypertensive being based on self-reported diagnosis and treatment by their GP, which may not be as reliable.

Age and BP are major contributors to arterial stiffness (Avolio et al. 1983; McEniery et al. 2005; Zheng et al. 2014). In our study population, no significant correlation was found between cPWV and either of age or BP mainly due to the small sample size, subjects' age, and a relatively narrow age range of the participants. Elevated cPWV in the older group (aged 80 to 89) observed in the current study is in accordance with previously reported findings of large population studies such as the Anglo-Cardiff Collaborative Trial (McEniery et al. 2005) over 4001 subjects, Framingham Heart study (Mitchell et al. 2007) over 2036 participants, and a metaanalysis across 223 studies (Khoshdel et al. 2006) suggesting large artery stiffening occurs more markedly later in life.

BP changes with advancing age. While SBP rises linearly from age 30 through the ninth decade of life, after age 50 to 60 years, DBP tends to decline or remain constant and MAP reaches an asymptote (Zheng et al. 2014; McEniery et al. 2005). Despite small sample size these trends are clearly reflected in the study group as illustrated in Figure 6.8. The association between rPWV and DBP in the subjects aged between 69 to 79 reflects progressive stiffening of the microvessels with advancing age.

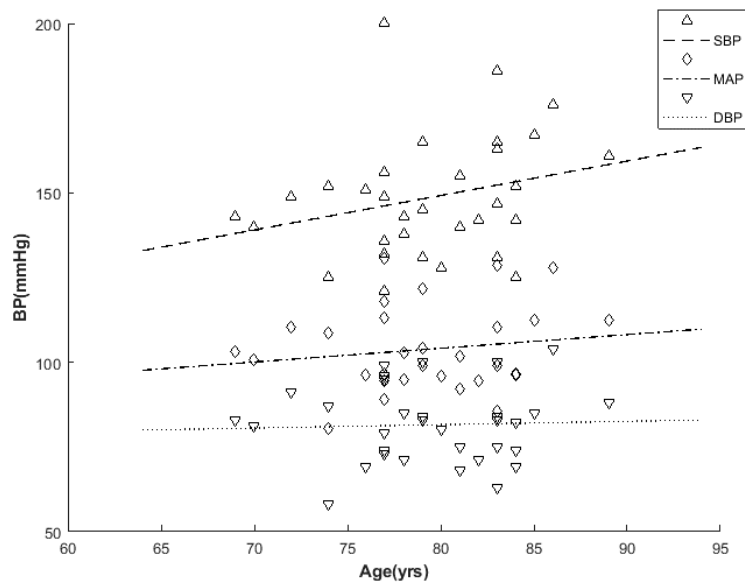


Figure 6.8. Regression lines representing the effect of age on SBP, MAP, and DBP

The novel findings of the current study suggest the independent predictive power of rPWV in age-related arterial stiffness. The narrow age range, limited number of the subjects, and the cross-sectional study design are limitations of the present study. Further longitudinal studies across a broad age range and larger sample size is required. Furthermore, rPWV and cPWV were not measured simultaneously and obtained in different positions which is less than ideal. Considering cross-sectional design of the study, rPWV and cPWV measured for all participants following the same protocol were compared between and not within individuals. Furthermore, the difference between seated and supine BP due to hydrostatic change would be relatively consistent between individuals as the distance between the eye and heart would be relatively constant. rPWV was measured prior to the cPWV in a seated position while cPWV was measured within almost 30 minutes in a supine position. Nevertheless, rPWV if proven by further research as a direct marker of arterial stiffness may be of great interest in the risk specially in aging cohort regularly attending ophthalmology clinic.

Prior to this study, several studies attempt to measure rPWV in human and in rodents. Kotliar *et al.* (2011) demonstrated the effect of age on PWV in retinal arteries. Later, they compared rPWV alterations between normal, high-normal and hypertensive subjects (Kotliar *et al.*

2013). However, the two studies show a difference of a factor of up to 100 in rPWV values (21.5 mm/s vs 0.4 mm/s in young normotensive subjects). Golzan *et al.* presented a method for quantification of rPWV of 114 mm/s in the rat eye using high-speed imaging (Golzan, Butlin, et al. 2014). Spahr *et al.* recently used high temporal and spatial resolution swept-source optical coherence tomography (OCT) to capture retinal vessel pulsations and rPWV based on surrounding tissue motions in a young subject as 620 mm/s (Spahr et al. 2015). The most recent study by Li *et al.* reported rPWV between 20 to 30 mm/s in young normotensive subjects (Qian Li et al. 2018). The reported values of rPWV presents a huge discrepancy by three orders of magnitude. Using retinal artery material stiffness and geometry, rPWV can be calculated *ex-vivo* to investigate the inconsistencies. *Ex-vivo* calculation of rPWV in healthy retinal arteries predict that a PWV in the order of 200 to 500 mm/s in a physiological range of distending pressure between 50 and 150 mmHg would be expected (Butlin et al. 2019). *In-vivo* rPWV was lower than expected yet was correlated with cPWV. A potential confounder in the current measurements might be the role of blood flow velocity which has been reported within a wide range between 1 to 300 mm/s in retinal arteries (Butt et al. 1995; Steigerwalt et al. 1995; Burgansky-Eliash et al. 2013). Further studies are required to uncover what rPWV is a measurement of, if not arterial stiffness.

Chapter 7

Calculation of retinal artery pulse wave velocity

The experiments described have been submitted for publication to the journal *Experimental Eye Research* and is under review as:

Butlin M, **Rezaeian M**, Schulz A, Leloup A, Golzan SM, Graham SL, Avolio PA,. Calculation of retinal artery pulse wave velocity. 2019.

Abstract

Non-invasive measurement of retinal pulse wave velocity (rPWV), as a measure of vessel stiffness, has been reported from 0.0004 to 0.6 m/s, a difference of 3 orders of magnitude between studies. This brings doubt into the accuracy of measurement. Expected rPWV is not known as it has not been quantified without extensive image and signal processing. This study aimed to calculate rPWV from *ex-vivo* measurement of vessel geometry and stiffness to inform the expected order of magnitude of rPWV *in-vivo*. Primary retinal artery branch diameter and wall thickness was assessed in bovine eyes (n=9) by optical coherence tomography. Tensile testing of the same vessel segments quantified material stiffness. Moens-Korteweg and Wolmersley's alpha equations were used to calculate rPWV from vessel geometry and stiffness. The retinal luminal diameter and wall thickness were 149 ± 13 μ m and 17.4 ± 1.6 μ m

respectively. For a theoretical distending pressure between 50 and 150 mmHg, rPWV ranged from 0.21 m/s to 0.51 m/s (average 0.39 ± 0.01 m/s). This computed value is greater than rPWV reported in most *in-vivo* studies though two studies do approach this range of values. The computed value of rPWV gives a reference value to which *in-vivo* methods can be compared in the future in the movement toward the measurement and use of rPWV in clinical studies.

7.1 Introduction

Stiffness of large arteries increases with age due to a multitude of factors including increased disparate calcification, cross-linking of collagen, and elastin degradation (Harvey et al. 2015). One method of assessing arterial stiffness *in-vivo* is by measuring the speed of the pulse wave (c) in the vessel segment by measuring the time it takes for the pulse to travel over a given distance (Equation 7-1). This is termed the pulse wave velocity (PWV). The faster the pulse wave travels along the artery wall, the stiffer the vessel (Butlin et al. 2017). This is a basic principle of materials as first described by Isaac Newton who related wave speed to material stiffness (bulk modulus, K), and material density (ρ) (Equation 7-2).

$$c = \frac{\text{distance}}{\text{transit time}} \quad \text{Equation 7-1}$$

$$c = \sqrt{\frac{K}{\rho}} \quad \text{Equation 7-2}$$

Measuring PWV across the carotid to femoral arterial path is a non-invasive approach for assessing large artery stiffness where the descending aorta is the predominant section of the vasculature assessed. Arterial PWV is inherently dependent on the acute distending blood pressure applied to that vessel (Bramwell et al. 1922; Spronck et al. 2015). Independent of blood pressure, carotid-femoral PWV increases with age (McEniery et al. 2005), indicating

intrinsic effects of vascular aging, and is associated with various diseases including end stage renal disease (Blacher et al. 1999), type 2 diabetes (Zhang et al. 2011) and cognitive decline (Nilsson et al. 2014; Pase et al. 2010; Poels et al. 2007). It is a recognised independent predictor of all-cause and cardiovascular mortality (Laurent et al. 2001) and has been adopted in the European Society of Hypertension guidelines as an associated measure for the management of hypertension (Williams et al. 2018).

Currently there is no direct way to measure the stiffness of microvessels non-invasively. In human studies where microvessel parameters need to be measured directly, a skin biopsy can be taken and microvessels isolated from the subcutaneous fat tissue. This, and other associative measures have been the limit of characterisation of microvessels in humans (Rizzoni et al. 2011). Due to the invasiveness of this procedure, the stiffness of the microcirculation in humans is not commonly studied.

The retinal vasculature provides a unique opportunity to visualise the microcirculation *in-vivo* and non-invasively. This makes the retina an ideal window to study microvascular-related pathogenesis. Retinal vessel visualization is used not only in the diagnosis and description of ophthalmic conditions (Bek 2013) but also other diseases with vascular implications. Alzheimer's disease has been linked with retinal vessel thinning, reduced tortuosity and branch density, and increased retinal venous and arterial pulsatility (Cheung et al. 2014; Frost et al. 2013; Golzan et al. 2017). In hypertension, retinal arteries have been shown to be vasoconstricted (Cheung, Ikram, et al. 2012; Ding et al. 2014) with reduced pulsatility (Rezaeian et al., 2016).

It follows that the stiffness of retinal vessels would be of interest in multiple pathologies. The concept of measuring PWV in retinal vessels is conceptually simple. Video images of the retina are analysed, and a segment of retinal artery analysed at two points a measured distance

apart to extract the diameter waveform at those two points. The time taken for the pulse wave to travel between those two points over a distance can then be measured, for example using the foot-to-foot method or cross-correlation techniques (Mitchell et al. 1997) applied to the diameter waveforms, and the PWV calculated as per Equation 7-1.

However, imaging the retinal vessel wall using current technology results in a low signal to noise ratio for the diameter waveform due to the relatively small (around 4%) pulse changes in diameter (Hao et al. 2012) given the spatial noise in detecting the edge of the vessel in video images. As a result, a degree of imaging and waveform processing is required to arrive at a value of transit time for calculation of rPWV. Kotliar *et al.* (Kotliar et al. 2011) in 2011 were the first to publish rPWV values in humans, reporting values of 0.022 m/s and 0.244 m/s in young and old people respectively. The same research group later reported that rPWV in hypertensive subjects (0.0012 m/s) was greater than in normotensive subjects (0.0004 m/s) (Kotliar et al. 2012; Kotliar et al. 2013). Whilst the change in magnitude was as hypothesised (higher stiffness with age and high blood pressure), the values of rPWV in the two studies differed by a factor of up to 1000. Golzan *et al.* (2014) used anaesthetised animals to take advantage of high light exposure to enable high-speed (250 frames/s) retinal imaging with similar but not identical processing methods to quantify rPWV as 0.114 m/s. Swept-source optical coherence tomography (OCT) has also been used to quantify rPWV, albeit in a single person, with a value of 0.62 m/s obtained (Spahr et al. 2015). The conclusion of the authors using swept-source OCT was that the value of 0.62 m/s is more realistic, given that the PWV in larger vessels is in the range of meters per second and it would be expected that small vessels would have a similar PWV. In 2018, spectral-domain OCT was used to assess rPWV with values reported in the range of 0.020 to 0.030 m/s in healthy individuals (Qian Li et al. 2018). In an experiment on 8 rats as part of this thesis (Chapter 5), for a physiological range of mean arterial blood pressure (MAP) between 50 and 150 mmHg, rPWV between 0.003 to

0.025 m/s (average 0.010 ± 0.004 m/s) was obtained. In the clinical study on 37 elderly participants presented in Chapter 6, an average rPWV of 0.025 ± 0.015 m/s was measured. The range in values reported for rPWV show that measurement of transit time is currently not robust to guarantee accurate absolute measurement of rPWV.

Using a derivation of Equation 7-2 for wave velocity in tubes, and accounting for viscous effects in small arteries, PWV can be calculated if the dimensions and material stiffness of the vessel are known. This study took *ex-vivo* measurements of the material stiffness and geometry of bovine retinal arteries to calculate rPWV to inform which if any of the existing *in-vivo* measures of rPWV represent the expected rPWV.

7.2 Materials and methods

The experiment was performed on 9 bovine eyes. Bovine eyes were chosen to facilitate dissection of retinal arteries and to permit mounting of the retinal arteries for tensile testing. The eyes were collected immediately following euthanasia at an abattoir and stored in 0.9% saline at 4°C. Post-mortem collection and use of the tissue complied by the Australian Code for the Care and Use of Animals for Scientific Purposes.

7.2.1 Geometry measurement

Within hours of collection, the retina *in situ* in the whole eye was imaged using OCT (Spectralis, Heidelberg Engineering, Heidelberg, Germany). A primary branch of the retinal artery adjacent to the optic disc was identified and the diameter and wall thickness of that vessel was measured using Heidelberg Eye Explore software (HEYEXTM, version 1.10.2.0) (Error! Reference source not found.).

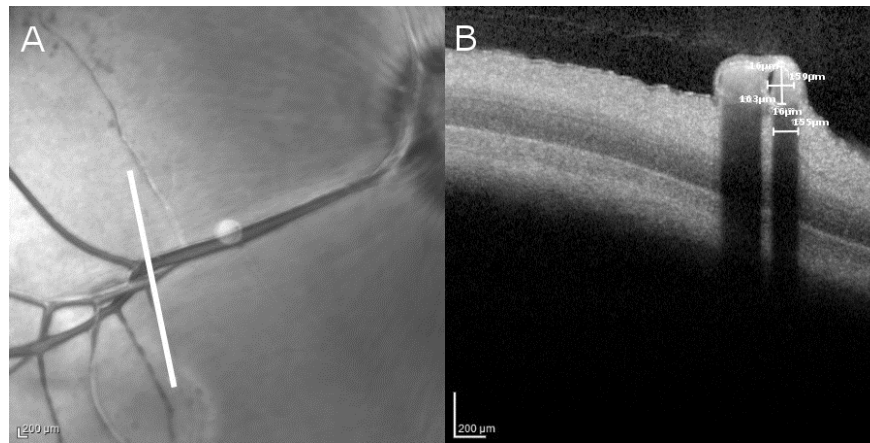


Figure 7.1. An example of an optical coherence tomography image of the bovine retina. (A) A primary branch of a retinal artery identified (optic disc shown in the top right of panel). (B) Cross section indicated by white line in panel (A), from which vessel dimensions were measured.

7.2.2 Tensile testing

Within 24 to 72 hours of tissue collection, the same segment of the retinal artery identified and measured using OCT was isolated. A non-branching section was cut to a length between 1 to 2 mm and mounted as a vessel ring with two stainless steel wires 20 μm in radius through the vessel lumen (**Figure 7.2**). One wire was attached to a force transducer to measure vessel wall tension and the other was attached to a single-axis micrometre screw-gauge (Multi Wire Myograph System 620M, DMT, Denmark). Once the vessel was mounted, the longitudinal length of the vessel was measured using standard microscopy. The vessel was kept submerged in a 0.9% saline solution which was heated to 37°C. The micrometre screw-gauge that applied circumferential strain to the vessel was positioned until the two wires within the lumen were touching and this was defined as zero gauge length. The vessel was then extended in 20 μm increments, allowing time for the vessel to relax at each increment and the force recorded once a force plateau was reached. Steps of 20 μm extension were applied until vessel break, or the maximum force of the transducer was reached (110 mN).

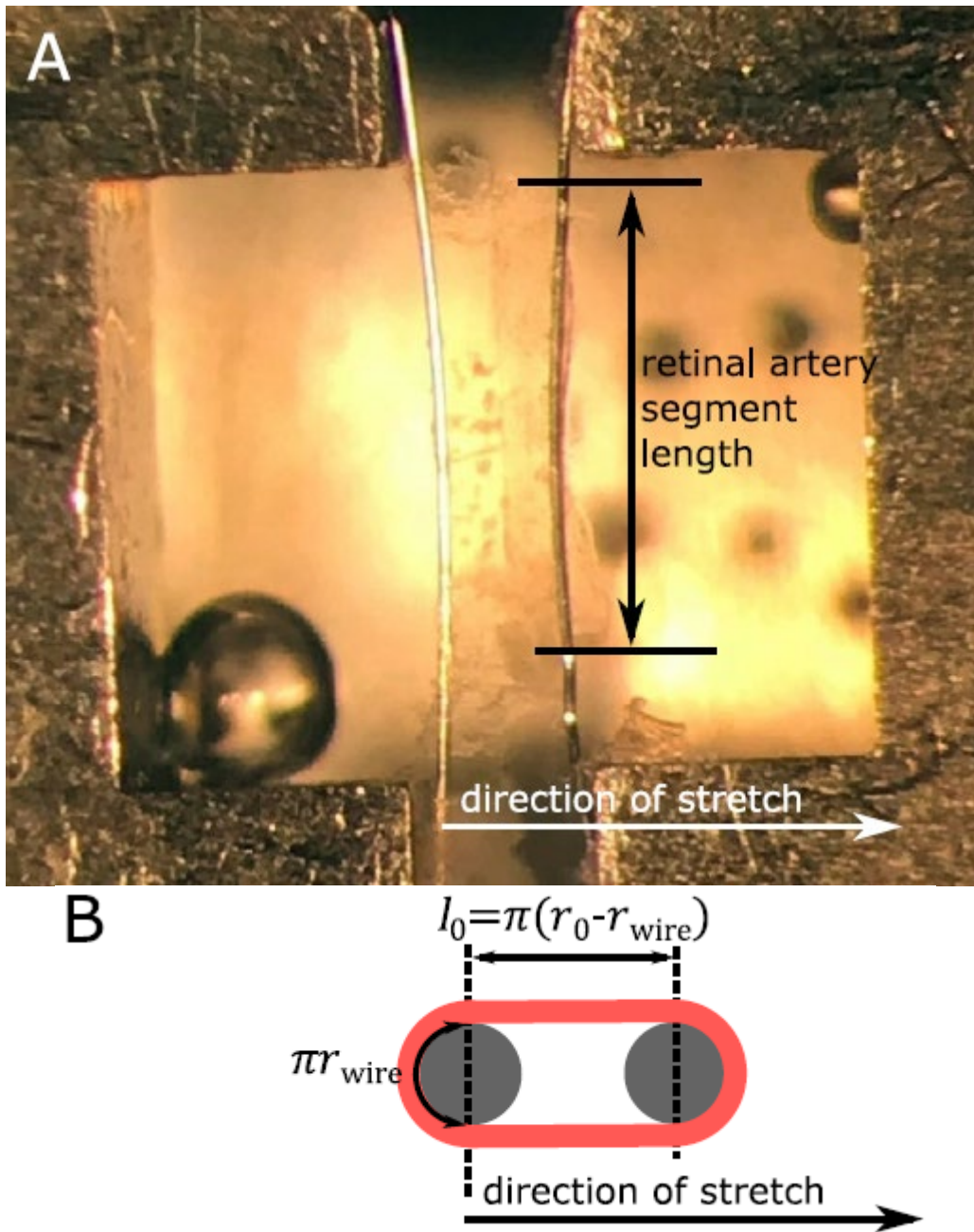


Figure 7.2. Retinal artery segment mounted for tensile testing. (A) Photograph of the retinal artery segment with two stainless steel wires, each 40 μm in diameter, through the vessel lumen that were used to apply the tensile load. (B) Schematic of a cross section of the mounted vessel with the calculation of the zero length (l_0) using the unloaded (0 mmHg) vessel radius (r_0) and the mounting wire radius (r_{wire}).

7.2.3 Calculations

Stress (σ) in Pascals was calculated using the recorded force (F) in Newtons with static values for vessel longitudinal length (l) and wall thickness (h) in meters as measured using OCT for each vessel to calculate the effective cross-sectional area over which the force was applied (Equation 7-3). The strain (ϵ) applied to the vessel was calculated as per Equation 7-6. Zero

length (l_0) was set as equivalent to the equivalent length at 0 mmHg (unpressurised vessel, vessel radius r_0) as measured with OCT. As mounted *ex-vivo* on the wires (**Figure 7.2**), the zero length equated to the internal vessel circumference ($2\pi r_0$) minus the path length around the wire ($2\pi r_{wire}$) divided by two (Equation 7-4). The extension (Δl) from l_0 was the length applied with the micrometer screw gauge (gauge length) plus the wire diameter (Equation 7-5, **Figure 7.2**). The incremental elastic modulus (E_{inc} , the material stiffness defined as the gradient of the stress-strain curve) was then calculated for each incremental extension increase (Equation 7-7).

$$\sigma = \frac{F}{2hl} \quad \text{Equation 7-3}$$

$$l_0 = \pi(r_0 - r_{wire}) \quad \text{Equation 7-4}$$

$$\Delta l = \text{gauge length} + 2 \cdot r_{wire} - l_0 \quad \text{Equation 7-5}$$

$$\varepsilon = \frac{\Delta l}{l_0} \quad \text{Equation 7-6}$$

$$E_{inc} = \frac{\Delta \sigma}{\Delta \varepsilon} \quad \text{Equation 7-7}$$

The applied force per unit area was converted into the theoretical distending transmural pressure. The equivalent radius was calculated at each point using the internal circumference as mounted on the wires (Equation 7-8). The wall thickness was then calculated using that radius assuming the cross-sectional area (A) did not change with stretch of the vessel (Equation 7-9). Using the Laplace formula and the values of wall thickness (h) and vessel radius (r), the theoretical distending pressure was calculated (Equation 7-10).

$$r = \frac{l_0 + \Delta l + \pi r_{wire}}{\pi} \quad \text{Equation 7-8}$$

$$h = -r + \sqrt{\frac{A}{\pi} + r^2} \quad \text{Equation 7-9}$$

$$P = \sigma \times \frac{h}{r} \quad \text{Equation 7-10}$$

The Moens-Korteweg equation (Equation 7-11) is a derivation from Newton's equation for wave speed (Equation 7-2) for the specific scenario of wave speed (PWV) in a thin walled tube, such as an artery. Given the knowledge of incremental elastic modulus (E_{inc}), wall thickness (h) and vessel radius (r) and using a blood density (ρ) of 1050 kg/m³, PWV₀ could be calculated. This value of PWV₀ stands true for PWV measured *in-vivo* for large vessels. However, for small vessels, such as retinal vessels, viscous (μ) effects are much greater and the *in-vivo* measured PWV is much less than that calculated by the Moens-Korteweg equation (Salotto et al. 1986). Using the relationship of Womersley's alpha (Equation 7-12) and knowing the radius of the vessel (r) and heart rate at which the vessel oscillates at (frequency, ω) the ratio of the PWV as calculated by the Moens-Korteweg equation (PWV₀) and the PWV as would be measured *in-vivo* in small vessels can be calculated (See Appendix).

$$PWV_0 = \sqrt{\frac{E_{inc}h}{2\rho r}} \quad \text{Equation 7-11}$$

$$\alpha = r \sqrt{\frac{\omega\rho}{\mu}} \quad \text{Equation 7-12}$$

Taking from the literature, a 24-hour average heart rate for cattle of 67 bpm (1.1 Hz) was used in the calculation (Frese et al. 2017). The radius used was that of the specific vessel as measured using OCT. The PWV₀/PWV ratio (Appendix) was calculated using linear extrapolation of look up tables (Womersley 1957) to find the corresponding PWV₀/PWV value for the calculated α value. Using this ratio for each vessel and PWV₀ calculated as per the Moens-Korteweg equation, the retinal artery wave velocity (PWV) as would be measured *in-vivo* was calculated for each applied stress measured.

7.2.4 Statistics

No statistical comparisons have been performed as the study presents a single group (bovine retinal arteries) of *ex-vivo* measurements of vessel dimension and stress / strain testing, along with the calculated theoretical *in-vivo* distending pressure / PWV relationship. Data where graphically summarised is fitted by least squares regression with a shaded region representing the 95% confidence interval.

7.3 Results

Measured values of vessel geometry are provided in **Table 7.1**. Luminal diameter and wall thickness were relatively consistent between samples, reflecting a consistent location of retinal vessel being located in each bovine eye.

Table 7.1. Bovine retinal artery segment measurement by microscopy (length) and optical coherence tomography (luminal diameter, wall thickness).

sample	length (mm)	luminal diameter (μm)	wall thickness (μm)
1	1.75	172	19.7
2	1.80	133	14.5
3	1.63	149	17.2
4	1.30	156	16.1
5	1.80	132	17.3
6	1.38	152	17.7
7	1.70	149	17.6
8	1.90	134	17.0
9	1.88	160	19.5
mean \pm S.D.	1.68 \pm 0.21	149 \pm 13	17.4 \pm 1.6

Stress-strain curves were obtained for all samples with a quadratic relationship demonstrated between stress and strain that is typical for vascular tissue (**Figure 7.3**). The PWV and distending pressure calculated from the stress-strain data are shown in **Figure 7.4** with PWV having a log relationship with distending pressure across the range of distending pressure that extended above and below the physiological range. Data in a physiological range of distending pressure (nominally 50 to 150 mmHg) had rPWV ranging from 0.09 to 0.50 m/s

(average 0.39 ± 0.01 m/s, **Figure 7.4C**). The line of best fit showed PWV varied from 0.21 m/s at 50 mmHg up to 0.51 m/s at 150 mmHg.

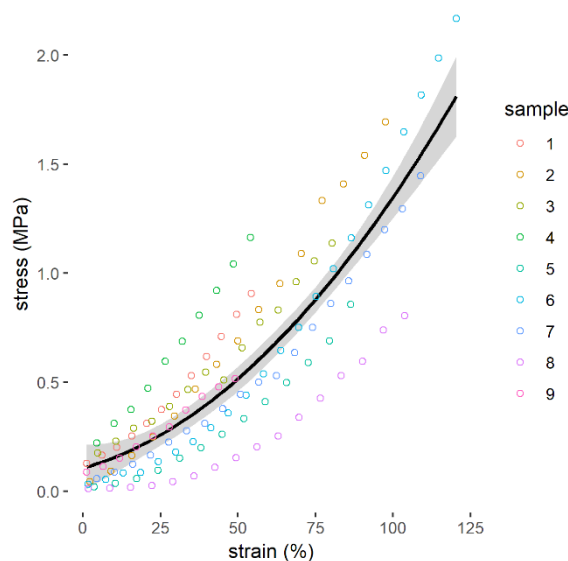


Figure 7.3. The measured relationship between stress (σ) and strain (ϵ) for 9 tested bovine retinal arteries. The solid line provides the quadratic line of best fit ($\sigma = 2.0 \times 10^6 \times \epsilon^2 + 5.5 \times 10^6 \times \epsilon + 0.37 \times 10^6$, $R^2=0.86$).

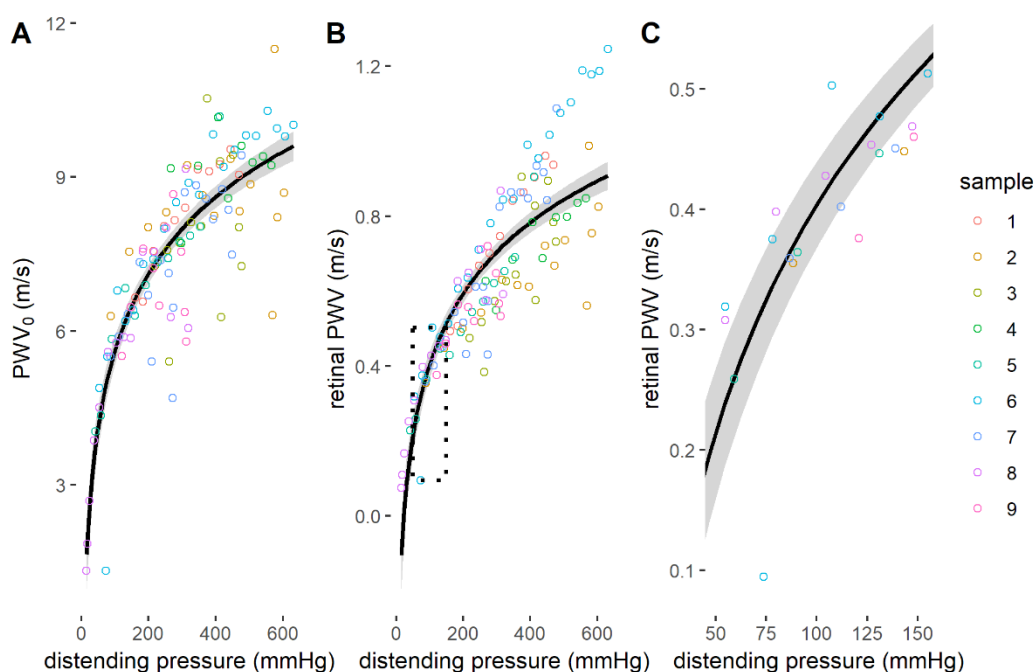


Figure 7.4. Calculated retinal pulse wave velocity. (A) Pulse wave velocity as calculated by the Moens-Korteweg equation (PWV_0) for distending transmural pressure (P) expressed in mmHg. (B) PWV accounting for viscous effects as would be observed in small vessels such as the retinal arteries. The solid line provides the line of best fit ($PWV = 0.276 \ln(P) - 0.855$, $R^2=0.72$). (C) Exploded section of panel (B) for a physiological range of distending pressure (nominally 50 to 150 mmHg, dotted line panel (B)).

7.4 Discussion

The aim of the study was to find the order of magnitude of PWV in retinal arteries under the current limitation that *in-vivo* imaging techniques give highly varied results. By measuring the retinal artery wall elastic modulus and vessel dimensions, rPWV could be calculated. As measurement of the elastic modulus requires fresh tissue, animal tissue was used as an approximate of the human retinal vasculature.

The PWV calculated using the Moens-Korteweg equation (PWV_0) was of the same order of magnitude and range as PWV in large arteries such as the aorta and brachial and femoral arteries (Avolio et al. 1985) and of smaller arteries such as the coronary arteries (Harbaoui et al. 2017). From a physiological point of view, near-constant PWV throughout the arterial network is rational as it would limit impedance mismatch and reduce wave reflection that would otherwise result in an amplification of the pulse pressure. However, it is known that vessels with diameters in the range of those observed in retinal arteries have a viscous effect that modifies PWV from that calculated under the assumptions of the Moens-Korteweg equation. Taking this into account, the calculated rPWV is in the range of tens of cm/s (0.09 to 0.50 m/s).

The calculated range of rPWV is between 1 and 3 orders of magnitude higher than values of rPWV in the literature as measured using imaging techniques (Figure 7.5) with two exceptions. Values of rPWV in the range of 0.2 to 0.5 m/s have been reported in older human subjects (Kotliar et al. 2011). However, in the same study younger subjects with likely healthy small vessels (as were tested in this study) had rPWV values an order of magnitude smaller. Use of swept-source OCT has delivered a value of rPWV of 0.6 m/s (Spahr et al. 2015). Given the quality of the diameter waveforms reported in that study and the value of rPWV calculated, swept-source OCT may be a promising technique for rPWV measurement.

However, it has to date been reported for only a single subject and needs to be tested in a cohort of subjects.

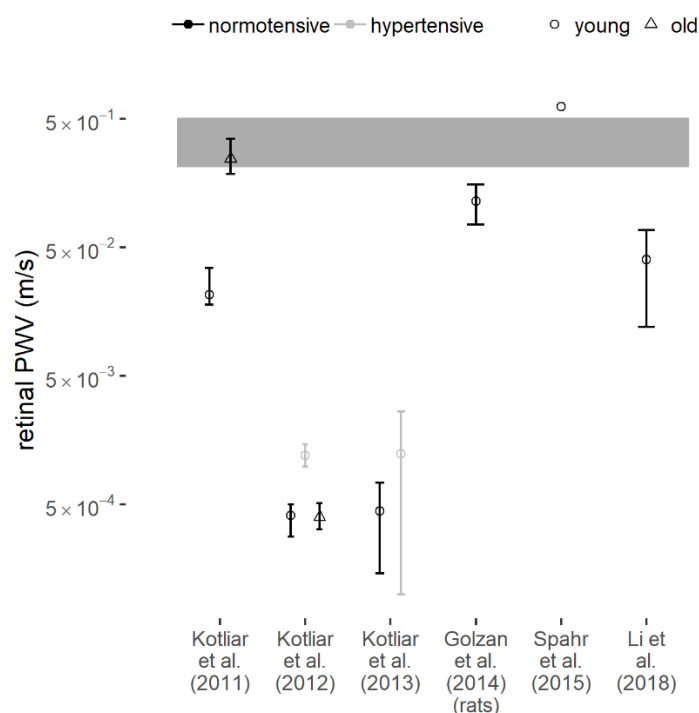


Figure 7.5. Reported values of retinal pulse wave velocity (PWV) in the literature as measured *in-vivo* using imaging techniques. Average values range from 0.004 m/s (Kotliar et al. 2012; Kotliar et al. 2013) to 0.62 m/s (Spahr et al. 2015). The shaded region indicates the expected value of retinal PWV as calculated in this study. Error bars indicate 95% confidence intervals.

The high degree of image and signal processing that is required to obtain a measure of rPWV, the variability in results of 1 to 3 orders of magnitude, and the small sample sizes in many of the studies with some studies relying on sample sizes of 1 and 2, all decrease confidence in the accuracy of the *in-vivo* rPWV measurements. However, the diameter signals produced in these studies have power at the cardiac frequency and some studies show the value of rPWV increases with blood pressure and age as would be hypothesised. It is therefore assumed that the *in-vivo* rPWV values are most likely measuring a true pulse wave, but these are not of the order of magnitude expected of a material of the type of the retinal arteries. It may be that some *in-vivo* rPWV measurement techniques are detecting signals associated with retinal blood flow velocity, and not rPWV. Values of central retinal artery blood flow velocity vary in the literature ranging from 1 to 4 mm/s average velocity (Burgansky-Eliash et al. 2013) up to 100

to 300 mm/s peak systolic velocities (Butt et al. 1995; Steigerwalt et al. 1995). This range of blood flow velocities coincides with reported rPWV by Kotliar *et al.* (Kotliar et al. 2011), Golzan *et al.* (Golzan, Butlin, et al. 2014) and Li *et al.* (Qian Li et al. 2018) but is lower than values reported by Spahr *et al.* (Spahr et al. 2015).

A further possibility is that imaging is detecting pulsatile variation in the choroid in addition to the pulse of the vessel itself. The eye is in contact with the intracranial space via the optic nerve sheath containing cerebrospinal fluid, which has a pulsatility that is synchronous with the heart (Wagshul et al. 2011). It is plausible that a wave initiating at the choroid near the optic sheath travels across the material of the choroid itself with each cardiac cycle. This would impact the depth and focus of the vessels when imaging and could be a possible source of pulsatile variation. However, segments of the choroid, such as the Bruch's membrane, have a high stiffness much greater than that of vascular tissue (Fisher 1987). It would be expected that the pulse wave through the choroid as a result would be much greater than that through the vascular tissue and would not explain the slower PWV reported from *in-vivo* measurement. Other layers of the eye of much less stiffness, such as the choriocapillaris, would have a much slower PWV of either vascular or intracranial fluid origin. Teasing apart these various layers and the impact on imaging of the retinal vessels would be very complex.

With a lack of tools to measure retinal arterial stiffness, other retinal vascular parameters have been associated with large artery stiffness to elucidate whether small and large vascular remodelling follow a similar pathway. A greater large artery stiffness has been related to reduced retinal artery size (García-Ortiz et al. 2015; Triantafyllou et al. 2014) and increased retinal vessel wall to lumen ratio (Rosenbaum et al. 2016). Increased carotid-femoral PWV has also been found to be positively associated with branch retinal vein occlusion (Kaderli et al. 2010; Nakazato et al. 2005). Should a reliable method of measurement of rPWV be

developed it will open up a direct way to assess the microvasculature *in-vivo*. The calculation of rPWV *ex-vivo* can inform *in-vivo* rPWV measurement accuracy so that once a suitable method is obtained it can be applied to clinical conditions such as those mentioned above.

In this study rPWV was not measured but calculated. This is an inherent limitation of the current state of the field in that rPWV measurements give disparate results, depending on the method, and there is currently no gold standard measurement technique that gives a definitive known true value. However, calculating rPWV also has limitations in the assumptions of the Moens-Korteweg equation, namely: (i) there is no, or insignificant change in vessel area; (ii) there is no, or insignificant change in wall thickness; (iii) that $dv(dr^{-1})dxdt$ is small to the point of insignificance (where v is velocity, r the vessel radius, x is arterial segment length, and t is time). Whilst changes in these parameters are limited for blood vessels, they do undergo small changes with applied stress and therefore the calculated PWV must be viewed as an estimate under the caveat of the above assumptions.

The method of tensile testing (wire tensile testing) did not identically replicate an internally fluid pressurised vessel as found *in-vivo* and tests using fluid pressurisation of vessels (as conventionally used in pressure myography) may yield marginally different results. Also, as a result of the method of tensile testing used, there were fewer retinal artery samples contributing data to the physiological range of stress than the number of samples in the study (20 data points from 6 of the 9 samples in the range of 50 to 150 mmHg). However, the fitted line in this region relied on data from all samples (121 data points from 9 samples) including data above and below the range of 50 to 150 mmHg.

7.5 Conclusions

Ex-vivo measurement of material properties and dimension of healthy retinal arteries predict that a PWV in the order of 0.2 to 0.5 m/s would be expected for distending pressures in the range of 50 to 150 mmHg. This has been demonstrated in bovine retinal arteries and a not dissimilar order of magnitude of rPWV would be expected in humans. This is not consistent with the highly varied and much lower values of rPWV that have been reported from processing of *in-vivo* video images of the retina. Better designed and powered studies are required in the space of *in-vivo* measurement of rPWV before it can be used as a reliable parameter for clinical research.

Acknowledgments

M.R. is supported by an Australian Government Research Training Program (RTP) Scholarship. SM.G is supported by a National Health and Medical Research Council-Australian Research Council Dementia Fellowship. We thank Dr Shahab Ranjabr of the University of Sydney for his assistance in sourcing the tissue.

Declaration of interest

Declarations of interest: none

Chapter 8

Discussion

This chapter provides a general discussion on the findings of this research. The significance of the results and limitations of each study have been discussed. Directions for future research has also been suggested. Since each chapter contains detailed discussion of the specific findings, this chapter provides a synthesis of the overall research project and a brief unifying discussion of the main findings and of their contribution to knowledge.

8.1 Summary of contributions and findings

The interrelationship between micro- and macro-vascular alterations related to CVD risk factors specifically hypertension and arterial stiffness has been increasingly recognised (Cooper et al. 2016). Small muscular arteries and arterioles (less than 300 μm in calibre) are the major contributors to peripheral vascular resistance (Mayet et al. 2003) and accordingly play a key role in wave prorogation phenomena associated with arterial stiffness and aetiologies related to vascular compliance such as hypertension (Struijker-Boudier et al. 2012). However, there is a remarkable lack of research on the investigation and explanation of the link.

The retina provides non-invasive *in-vivo* visualization of the microcirculation. The current research was comprised of both controlled animal experiments and an observational clinical study has been conducted to explore the hypothesis whether dynamic characteristics of retinal vessels including pulsatile diameter changes and PTT (in retinal arteries in particular) correlate with BP changes and PWV in large arteries as a clinical marker of arterial stiffness.

One of the contributions of the findings of this thesis is the development of a novel computerised method for the measurement of the dynamic diameter changes of retinal vessels. In contrast to the static methods which are commonly used in almost all epidemiological studies investigating retinal vascular diameter in different diseases, dynamic analysis by measuring time-dependent cardiac changes may provide more useful information on risk prediction of CVD compared with static markers. The proposed vessel segmentation and diameter measurement method is computationally cheap with high level of accuracy and precision when compared with manual vessel segmentation and diameter measurement.

Using the proposed dynamic analysis tool, the abovementioned hypothesis has been addressed through multiple experimental investigations as follows:

First, a comparative study between transgenic hypertensive rats (spontaneously hypertensive rats; SHR) and Wistar Kyoto (WKY) rats which SHR are inbred from as controls showed smaller calibre and pulse amplitude in arterioles but not venules in SHR independent of sex. Retinal arteriolar narrowing has been evidenced by several population-based studies as explained in detail in Section 2.7.1 . In addition to validating the discriminative power of time-dependent diameter changes of retinal vessels, this association provides important insights into the crosstalk between hypertension-related vascular changes in small and large vessels. Assuming retinal arteriolar narrowing represents the same structural remodelling in small resistance arteries of the vascular tree, this observation might imply a link between increased peripheral resistance following arteriolar thinning and elevated BP. Dynamic interactions between retinal arterial calibre and arterial pulse amplitude with elevated BP in hypertensive rats suggest that arteriolar narrowing initiated by raised BP might amplify BP elevation in a vicious cycle.

Arterial stiffness has a known pressure dependence and the measures of arterial stiffness including PWV exhibit the same innate dependence on pressure. The next experiment carried out on Sprague Dawley rats showed a strong negative correlation between retinal artery PTT and increasing BP as expected. Moreover, there was a strong positive correlation between rPWV and aortic PWV measured invasively using pressure catheters introduced into the descending aorta. rPWV followed aPWV alterations induced by BP manipulations. The relationship was described as $rPWV = 1.32e^{-3} \times aPWV + 1.86e^{-3}$ ($R^2 = 0.09$, $p = 0.03$). The immediate effect of BP alterations on rPWV suggests that the measurement of rPWV

might be useful for early detection of hypertension and arterial stiffness before irreversible structural remodelling and end organ damage.

Further to the animal studies, a clinical investigation on an elderly cohort revealed a strong positive correlation between rPWV and central PWV measured between carotid and femoral arteries formulated as $rPWV = 7.68e^{-3} \times cPWV - 55.19e^{-3}$ ($R^2 = 0.59$, $p < 0.001$). The correlation between rPWV and cPWV in the elderly human cohort was different from the correlation between rPWV and aPWV in rats. This could be explained by distinct difference in the structure of the arterial tree between the species. The small arteries the size of arteries in rats are more muscular and the aorta in the human is more elastic compared with that in rats. In addition, while the subjects of the human study were older adults with obvious aged arteries (reflected by an elevated average cPWV of 8.9 m/s compared to 5 m/s in healthy young individuals) the animals were young and healthy. Furthermore, although cPWV and aPWV are highly correlated indices both dependent on age and BP, they are different. Here, in particular, aPWV in rats was measured invasively in the supine position simultaneously with rPWV while cPWV in the volunteers was measured seated almost half an hour after taking retinal recordings. IOP was not measured in rats, however, its effect on rPWV was not that significant in humans. Body position also effects hemodynamics. In this human cohort, no correlation was found between BP and rPWV. It is acknowledged that the study is limited to senior subjects (69-89 yrs) and further studies are required to obtain age-specific baseline values of rPWV.

Previous studies on the measurement of rPWV either in human or animals are very scarce, and the few existing ones do not coincide as discussed in detail in Chapter 7 of this thesis. To estimate the order of magnitude of PWV in retinal arteries, an *ex-vivo* experiment was conducted on bovine eyes to measure the elastic modulus and geometry of retinal arteries and

to calculate rPWV using the Moens-Korteweg equation for the wave speed in a thin wall vessel segment and for an inviscid fluid. According to the Moens-Korteweg equation, PWV in the same range as PWV in large arteries (i.e. in the order of 10 m/s) would be expected in retinal arteries. Taking into account the effect of finite fluid viscosity in small vessels using Womersley's alpha formula, rPWV of two orders of magnitude slower than in large arteries was predictable but this is still one order of magnitude faster than *in-vivo* measurements of this research.

8.2 Limitations and future directions

There are limitations with the current study. First, the proposed method for the measurement of PTT uses the slope of the regression line of the phase shifts derived from FFT on angular frequencies. Accordingly, it is dependent on the number of samples of Fourier transform. This is a constraint in extracting short epochs from the retinal recordings in order to detect more accurate instant changes in PTT. Limited spatial resolution and small signal to noise ratio of the retinal diameter waveforms were other limiting factors of the current research. Furthermore, in the clinical study, simultaneous measurement of rPWV and cPWV was not possible. Furthermore, while rPWV was measured seated, cPWV was measured in the supine position which may affect hemodynamics. In addition, in both human and animal studies, rPWV values were not different in large arteries of the same eye. However, the effect of calibre, tortuosity, branching, distance from the optic disc at which diameter waveforms were calculated, the quadrant the vessel belongs to, and the side of the eye on rPWV needs to be elucidated in future studies.

Although several methodologies have been realised as research tools for the assessment of rPWV, none of them has found its way into the clinical practice. To allow the use of rPWV as a potential risk stratification tool, larger cohort and longitudinal studies are required to obtain

age-specific normative baselines in the first step. Moreover, further research is required to investigate possible additional prognostic and therapeutic information which retinal dynamic vascular markers may provide such as if retinal manifestations precede, coincide with, or follow traditional risk factors of CVD.

8.3 Conclusions

The theoretical estimate of rPWV obtained by the *ex-vivo* experiment suggests that what has been measured *in-vivo* is generally in accordance with predicted estimates of PWV in retinal arteries being orders of magnitude lower than PWV in large arteries, albeit with substantial variation in the measurements. According to the only study (Spahr et al. 2015) which has measured rPWV very close to the theoretical estimate, high standards of imaging requirements in terms of temporal and spatial resolutions and signal to noise ratio are needed for measuring true rPWV. However, this study, similar to studies prior to 2015 using the DVA (Kotliar et al. 2011; Kotliar et al. 2013; Golzan, Butlin, et al. 2014), found promising findings on the association between the retinal measurements and age and BP as the key contributors to CVD risk. The diameter waveforms in this study present power at the cardiac frequency. Furthermore, for the first time, a positive correlation with aortic PWV in rats and central PWV in humans has been observed. It is plausible that detected pulses may also be measuring blood flow velocity which may be a confounder for the pulse disturbance propagating along the arterial wall. Considering that DVA is the only dynamic measure commercially available, further research on the measurements of rPWV and its possible sources of error may facilitate retinal vascular markers to find their way to clinical investigations rather than being only a research tool.

References

- Abdallah, M. Ben & Malek, J., 2015. Automatic Extraction of Blood Vessels in the Retinal Vascular Tree Using Multiscale Medialness. *International Journal of Biomedical Imaging*, 2015(1).
- Abularrage, C. et al., 2005. Evaluation of the microcirculation in vascular disease. *Journal of Vascular Surgery*, 42(3), pp.574–581.
- Aliahmad, B., 2014. *Novel Methods in Retinal Vessel Calibre Feature Extraction for Systemic Disease Assessment*.
- Almotiri, J., Elleithy, K. & Elleithy, A., 2018. Retinal Vessels Segmentation Techniques and Algorithms: A Survey. *Applied Sciences*, 8(2), p.155.
- Araújo, T., Mendonça, A.M. & Campilho, A., 2018. Parametric model fitting-based approach for retinal blood vessel caliber estimation in eye fundus images T. W. Secomb, ed. *PLOS ONE*, 13(4), p.e0194702.
- Avolio, A. et al., 1985. Effects of aging on arterial distensibility in populations with high and low prevalence of hypertension: comparison between urban and rural communities in China. *Circulation*, 71(2), pp.202–10.
- Avolio, A. et al., 1983. Effects of aging on changing arterial compliance and left ventricular load in a northern Chinese urban community. *Circulation*, 68(1), pp.50–58.
- Avolio, A. & Butlin, M., 2015. Dependence of arterial stiffness on pressure quantified in the realm of the cardiac cycle. *Journal of Hypertension*, 33(2), pp.257–259.
- Bailey, M.A. et al., 2014. Carotid-femoral pulse wave velocity is negatively correlated with aortic diameter. *Hypertension Research*, 37(10), pp.926–932.
- Baumann, B. et al., 2011. Total retinal blood flow measurement with ultrahigh speed swept source/Fourier domain OCT. *Biomedical Optics Express*, 2(6), p.1539.
- Bek, T., 2013. Regional morphology and pathophysiology of retinal vascular disease. *Progress in Retinal and Eye Research*, 36, pp.247–259.
- Bernardes, R., Serranho, P. & Lobo, C., 2011. Digital ocular fundus imaging: A review. *Ophthalmologica*, 226(4), pp.161–181.
- Blacher, J. et al., 2003. Aortic pulse wave velocity index and mortality in end-stage renal disease. *Kidney International*, 63(5), pp.1852–1860.
- Blacher, J. et al., 1999. Impact of aortic stiffness on survival in end-stage renal disease. *Circulation*, 99(18), pp.2434–2439.
- Blatter, C. et al., 2013. Dove prism based rotating dual beam bidirectional Doppler OCT. *Biomedical Optics Express*, 4(7), p.1188.
- Boas, D.A. & Dunn, A.K., 2010. Laser speckle contrast imaging in biomedical optics. *Journal of Biomedical Optics*, 15(1), p.011109.
- Bouma, B.E. et al., 2009. Fourier-domain optical coherence tomography: recent advances toward clinical utility. *Current opinion in biotechnology*, 20(1), pp.111–8.

- Boutouyrie, P. et al., 2002. Aortic stiffness is an independent predictor of primary coronary events in hypertensive patients: a longitudinal study. *Hypertension (Dallas, Tex. : 1979)*, 39(1), pp.10–5.
- Boutsidis, C. et al., 2015. Randomized Dimensionality Reduction for k-Means Clustering. *IEEE Transactions on Information Theory*, 61(2), pp.1045–1062.
- Bramwell, J.C. & Hill, A. V., 1922. The Velocity of the Pulse Wave in Man. *Proceedings of the Royal Society B: Biological Sciences*, 93(652), pp.298–306.
- Burgansky-Eliash, Z. et al., 2013. The correlation between retinal blood flow velocity measured by the retinal function imager and various physiological parameters. *Ophthalmic Surgery, Lasers and Imaging Retina*, 44(1), pp.51–58.
- Butlin, M. et al., 2019. Calculation of retinal artery pulse wave velocity. *Experimental eye research* [Under review].
- Butlin, M. et al., 2015. Pressure dependency of aortic pulse wave velocity in vivo is not affected by vasoactive substances that alter aortic wall tension ex vivo. *American Journal of Physiology - Heart and Circulatory Physiology*, 308(10), pp.H1221–H1228.
- Butlin, M. & Qasem, A., 2017. Large Artery Stiffness Assessment Using SphygmoCor Technology. *Pulse (Basel, Switzerland)*, 4(4), pp.180–192.
- Butt, Z. et al., 1995. Measurement of ocular blood flow velocity using colour Doppler imaging in low tension glaucoma. *Eye (London, England)*, 9(1), p.29.
- Cecelja, M. & Chowienzyk, P., 2012. Role of arterial stiffness in cardiovascular disease. *JRSM cardiovascular disease*, 1(4), p.11.
- Cerný, V., Turek, Z. & Parízková, R., 2007. Orthogonal polarization spectral imaging. *Physiological research*, 56(2), pp.141–7.
- Chan, K.K.W. et al., 2017. Retinal vasculature in glaucoma: a review. *BMJ Open Ophthalmology*, 1(1), p.e000032.
- Chang, L. et al., 2014. Alzheimer's disease in the human eye. Clinical tests that identify ocular and visual information processing deficit as biomarkers. *Alzheimer's & dementia : the journal of the Alzheimer's Association*, 10(2), pp.251–61.
- Chen, Y. et al., 2017. Arterial stiffness and stroke: de-stiffening strategy, a therapeutic target for stroke. *BMJ*, 2(2), pp.65–72.
- Cheung, C. et al., 2010. A New Method to Measure Peripheral Retinal Vascular Caliber over an Extended Area. *Microcirculation*, 17(7), pp.495–503.
- Cheung, C. et al., 2014. Microvascular network alterations in the retina of patients with Alzheimer's disease. *Alzheimer's and Dementia*, 10(2), pp.135–142.
- Cheung, C., Ikram, M.K., et al., 2012. Retinal microvasculature as a model to study the manifestations of hypertension. *Hypertension*, 60(5), pp.1094–103.
- Cheung, C., Thomas, G.N., et al., 2012. Retinal Vascular Fractal Dimension and Its Relationship With Cardiovascular and Ocular Risk Factors. *American Journal of Ophthalmology*, 154(4), pp.663–674.
- Cheung, C. et al., 2011. Retinal vascular tortuosity, blood pressure, and cardiovascular risk factors. *Ophthalmology*, 118(5), pp.812–8.
- Choi, W. et al., 2012. Measurement of pulsatile total blood flow in the human and rat retina with ultrahigh speed spectral/Fourier domain OCT. *Biomedical Optics Express*, 3(5), p.1047.
- Cooper, L.L. et al., 2016. Microvascular Function Contributes to the Relation Between Aortic Stiffness and Cardiovascular Events: the Framingham Heart Study. *Circulation: Cardiovascular Imaging*, 9(12), p.e004979.
- Cruickshank, K. et al., 2002. Aortic pulse-wave velocity and its relationship to mortality in diabetes and glucose intolerance: an integrated index of vascular function? *Circulation*, 106(16), pp.2085–90.
- Cutolo, M., Pizzorni, C. & Sulli, A., 2005. Capillaroscopy. *Best Practice & Research Clinical Rheumatology*, 19(3), pp.437–452.

- Dai, C. et al., 2013. Absolute Retinal Blood Flow Measurement With a Dual-Beam Doppler Optical Coherence Tomography. *Investigative Ophthalmology & Visual Science*, 54(13), p.7998.
- Dash, J. & Bhoi, N., 2017. A thresholding based technique to extract retinal blood vessels from fundus images. *Future Computing and Informatics Journal*, 2(2), pp.103–109.
- Dash, J. & Bhoi, N., 2018. Retinal blood vessel segmentation using Otsu thresholding with principal component analysis. In *2018 2nd International Conference on Inventive Systems and Control (ICISC)*. IEEE, pp. 933–937.
- Ding, J. et al., 2014. Review: Retinal vascular caliber and the development of hypertension: A meta-analysis of individual participant data. *Journal of hypertension*, 32(2), pp.207–15.
- Ding, K., Xiao, L. & Weng, G., 2017. Active contours driven by region-scalable fitting and optimized Laplacian of Gaussian energy for image segmentation. *Signal Processing*, 134, pp.224–233.
- Dorner, G.T. et al., 2002. Calculation of the diameter of the central retinal artery from noninvasive measurements in humans. *Current Eye Research*, 25(6), pp.341–345.
- Eriksson, S., Nilsson, J. & Stureson, C., 2014. Non-invasive imaging of microcirculation: a technology review. *Medical devices (Auckland, N.Z.)*, 7, pp.445–52.
- Espona, L. et al., 2007. A Snake for Retinal Vessel Segmentation. In *Pattern Recognition and Image Analysis*. Berlin, Heidelberg: Springer Berlin Heidelberg, pp. 178–185.
- Fekete, G.T. et al., 2015. Retinal blood flow in mild cognitive impairment and Alzheimer's disease. *Alzheimer's & Dementia: Diagnosis, Assessment & Disease Monitoring*, 1(2), pp.144–151.
- Fischer, M.J.M., Uchida, S. & Messlinger, K., 2010. Measurement of meningeal blood vessel diameter in vivo with a plug-in for ImageJ. *Microvascular Research*, 80(2), pp.258–266.
- Fisher, R.F., 1987. The influence of age on some ocular basement membranes. *Eye (London, England)*, 1 (Pt 2), pp.184–189.
- Flammer, J. et al., 2013. The eye and the heart. *European Heart Journal*, 34(17), pp.1270–1278.
- Fleener, B.S. & Berrones, A.J., 2015. *Arterial Stiffness*, Cham: Springer International Publishing.
- Fraz, M.M. et al., 2012. Blood vessel segmentation methodologies in retinal images - A survey. *Computer Methods and Programs in Biomedicine*, 108(1), pp.407–433.
- Frese, D.A. et al., 2017. Twenty-four hour Holter monitoring in finishing cattle housed outdoors. *Journal of Veterinary Cardiology*, 19(2), pp.153–159.
- Frost, S. et al., 2013. Retinal vascular biomarkers for early detection and monitoring of Alzheimer's disease. *Translational psychiatry*, 3, p.e233.
- Gao, X. et al., 2001. A method of vessel tracking for vessel diameter measurement on retinal images. *Proceedings 2001 International Conference on Image Processing (Cat. No.01CH37205)*, 2, pp.881–884.
- García-Ortiz, L. et al., 2015. The role of retinal vessels caliber as a marker of vascular aging in large arteries. *Journal of Hypertension*, 33(4), p.818–26; discussion 826.
- Goedhart, P. et al., 2007. Sidestream Dark Field (SDF) imaging: a novel stroboscopic LED ring-based imaging modality for clinical assessment of the microcirculation. *Optics Express*, 15(23), p.15101.
- Golzan, S., 2012. *Analysis of pulsatile characteristics of the retinal vasculature and association with cerebrospinal fluid pressure*. Macquarie University.
- Golzan, S., Orr, C., et al., 2014. Characterizing Dynamic Properties of Retinal Vessels in Alzheimer's Disease. *Alzheimer's & Dementia*, 10(4), p.P235.
- Golzan, S., Butlin, M., et al., 2014. Characterizing dynamic properties of retinal vessels in the rat eye using high speed imaging. *Microvascular Research*, 92, pp.56–61.
- Golzan, S. et al., 2017. Retinal vascular and structural changes are associated with amyloid burden in the elderly: ophthalmic biomarkers of preclinical Alzheimer's disease.

- Alzheimer's Research & Therapy*, 9(1), p.13.
- Golzan, S., Kim, M. & Seddighi, A., 2012. Non-invasive estimation of cerebrospinal fluid pressure waveforms by means of retinal venous pulsatility and central aortic blood pressure. *Annals of biomedical engineering*, 40(9), pp.1940–1948.
- Gonzalez, R.C., Woods, R.E. & Eddins, S.L., 2007. *Digital Image Processing Using MATLAB®* | Pearson, Prentice Hall Press.
- Guc, M. & Dizdaroglu, B., 2015. Efficient retinal vessel segmentation with level sets. In *2015 Medical Technologies National Conference (TIPTEKNO)*. IEEE, pp. 1–4.
- Gui, B., Shuai, R.-J. & Chen, P., 2018. Optic disc localization algorithm based on improved corner detection. *Procedia Computer Science*, 131, pp.311–319.
- Habib, M.S. et al., 2014. The association between retinal vascular geometry changes and diabetic retinopathy and their role in prediction of progression--an exploratory study. *BMC ophthalmology*, 14, p.89.
- Haindl, R. et al., 2016. Total retinal blood flow and reproducibility evaluation by three beam optical Doppler tomography F. Manns, P. G. Söderberg, & A. Ho, eds. *Ophthalmic Technologies XXVI*, 9693, p.969302.
- Hao, H., 2014. *Analysis of variation in retinal vascular assessment*. RMIT University.
- Hao, H. et al., 2012. Does retinal vascular geometry vary with cardiac cycle? *Investigative Ophthalmology and Visual Science*, 53(9), pp.5799–5805.
- Harbaoui, B. et al., 2017. Development of Coronary Pulse Wave Velocity: New Pathophysiological Insight Into Coronary Artery Disease. *Journal of the American Heart Association*, 6(2).
- Harvey, A., Montezano, A.C. & Touyz, R.M., 2015. Vascular biology of ageing—Implications in hypertension. *Journal of Molecular and Cellular Cardiology*, 83, pp.112–121.
- Heringa, S.M. et al., 2013. Associations between retinal microvascular changes and dementia, cognitive functioning, and brain imaging abnormalities: a systematic review. *Journal of Cerebral Blood Flow & Metabolism*, 33(7), pp.983–95.
- Huang, S. et al., 2016. In vivo imaging of retinal hemodynamics with OCT angiography and Doppler OCT. *Biomedical Optics Express*, 7(2), p.663.
- Hughes, A.D. et al., 2013. Limitations of Augmentation Index in the Assessment of Wave Reflection in Normotensive Healthy Individuals W. R. Bauer, ed. *PLoS ONE*, 8(3), p.e59371.
- Hutchings, S., Watts, S. & Kirkman, E., 2016. The Cytocam video microscope. A new method for visualising the microcirculation using Incident Dark Field technology. *Clinical Hemorheology and Microcirculation*, 62(3), pp.261–271.
- Ikonomidis, I., Makavos, G. & Lekakis, J., 2015. Arterial stiffness and coronary artery disease. *Current Opinion in Cardiology*, 30(4), p.1.
- Ikram, M., Cheung, C., et al., 2013. Retinal vascular caliber as a biomarker for diabetes microvascular complications. *Diabetes care*, 36(3), pp.750–9.
- Ikram, M., Ong, T., et al., 2013. Retinal vascular caliber measurements: clinical significance, current knowledge and future perspectives. *Ophthalmologica*, 229(3), pp.125–36.
- Ikram, M., de Jong, F.J., et al., 2006. Retinal vessel diameters and risk of stroke: The Rotterdam Study. *Neurology*, 66(9), pp.1339–1343.
- Ikram, M. & Witteman, J., 2006. Retinal Vessel Diameters and Risk of Hypertension The Rotterdam Study.
- Ilginis, T., Clarke, J. & Patel, P.J., 2014. Ophthalmic imaging. *British Medical Bulletin*, 111(1), pp.77–88.
- Jeganathan, V.S.E. et al., 2008. Retinal Vascular Caliber and Age-related Macular Degeneration: The Singapore Malay Eye Study. *American Journal of Ophthalmology*, 146(6), p.954–959.e1.
- Jeyasri, K., Subathra, P. & Annaram, K., 2013. Detection of Retinal Blood Vessels for

- Disease Diagnosis. *International Journal Of Advanced Research in Computer Science and Software Engineering*, 3(3), pp.6–12.
- Jonas, J.B. et al., 2014. Retinal vessel diameter and estimated cerebrospinal fluid pressure in arterial hypertension: the Beijing Eye Study. *American journal of hypertension*, 27(9), pp.1170–8.
- Kaderli, A.A. et al., 2010. Impaired aortic stiffness and pulse wave velocity in patients with branch retinal vein occlusion. *Graefe's Archive for Clinical and Experimental Ophthalmology*, 248(3), pp.369–374.
- Kande, G.B., Savithri, T.S. & Subbaiah, P.V., 2008. Retinal vessel segmentation using local relative entropy thresholding. In *2008 IEEE International Conference on Systems, Man and Cybernetics*. IEEE, pp. 3448–3453.
- Kar, S.S. & Maity, S.P., 2017. Detection of neovascularization in retinal images using mutual information maximization. *Computers & Electrical Engineering*, 62, pp.194–208.
- Katsi, V., 2012. Association between retinal microcirculation and aortic stiffness in hypertensive patients. *Journal of the American College of Cardiology*, 59(13), p.E1644.
- Kawasaki, R. et al., 2013. Retinal Vessel Caliber Is Associated with the 10-year Incidence of Glaucoma. *Ophthalmology*, 120(1), pp.84–90.
- Kawashima-Kumagai, K. et al., 2018. Association of retinal vessel calibers and longitudinal changes in arterial stiffness. *Journal of Hypertension*, 36(3), pp.587–593.
- Kelly, R. et al., 1989. Noninvasive determination of age-related changes in the human arterial pulse. *Circulation*, 80(6), pp.1652–9.
- Khoshdel, A.R. et al., 2006. Estimation of an age-specific reference interval for pulse wave velocity: a meta-analysis. *Journal of hypertension*, 24(7), pp.1231–1237.
- Kirin, M. et al., 2017. Determinants of retinal microvascular features and their relationships in two European populations. *Journal of hypertension*, 35(8), pp.1646–1659.
- Koch, E. et al., 2014. Morphometric analysis of small arteries in the human retina using adaptive optics imaging: relationship with blood pressure and focal vascular changes. *Journal of hypertension*, 32(4), pp.890–8.
- Kornfield, T.E. & Newman, E.A., 2015. Measurement of Retinal Blood Flow Using Fluorescently Labeled Red Blood Cells. *eNeuro*, 2(2).
- Kotliar, K. et al., 2012. Does increased blood pressure rather than aging influence retinal pulse wave velocity? *Investigative ophthalmology & visual science*, 53(4), pp.2119–2126.
- Kotliar, K. et al., 2008. Effect of aging on retinal artery blood column diameter measured along the vessel axis. *Investigative ophthalmology & visual science*, 49(5), pp.2094–102.
- Kotliar, K. et al., 2011. Pulse wave velocity in retinal arteries of healthy volunteers. *The British journal of ophthalmology*, 95(5), pp.675–9.
- Kotliar, K. et al., 2013. Retinal Pulse Wave Velocity in Young Male Normotensive and Mildly Hypertensive Subjects. *Microcirculation*, 20(5), pp.405–415.
- Kundu, A. & Chatterjee, R.K., 2012. Retinal vessel segmentation using Morphological Angular Scale-Space. In *2012 Third International Conference on Emerging Applications of Information Technology*. IEEE, pp. 316–319.
- Landa, G. et al., 2012. Initial report of quantification of retinal blood flow velocity in normal human subjects using the Retinal Functional Imager (RFI). *International Ophthalmology*, 32(3), pp.211–215.
- Laurent, S. et al., 2001. Aortic stiffness is an independent predictor of all-cause and cardiovascular mortality in hypertensive patients. *Hypertension*, 37(5), pp.1236–1241.
- Laurent, S. & Boutouyrie, P., 2015. The Structural Factor of Hypertension. *Circulation Research*, 116(6), pp.1007–1021.
- Li, H. et al., A piecewise Gaussian model for profiling and differentiating retinal vessels. In *Proceedings 2003 International Conference on Image Processing (Cat. No.03CH37429)*. IEEE, p. I-1069-72.

- Li, Q. et al., 2018. Response to Comment on “Retinal pulse wave velocity measurement using spectral-domain optical coherence tomography.” *Journal of Biophotonics*, 11(2), pp.9–11.
- Li, Q. et al., 2018. Retinal pulse wave velocity measurement using spectral-domain optical coherence tomography. *Journal of Biophotonics*, 11(2), p.e201700163.
- Liberson, A.S. et al., 2016. A physics based approach to the pulse wave velocity prediction in compliant arterial segments. *Journal of Biomechanics*, 49(14), pp.3460–3466.
- Lim, L.S. et al., 2014. Dynamic responses in retinal vessel caliber with flicker light stimulation in eyes with diabetic retinopathy. *Investigative Ophthalmology and Visual Science*, 55(8), pp.5207–5213.
- Lim, M. et al., 2013. Systemic associations of dynamic retinal vessel analysis: a review of current literature. *Microcirculation*, 20(3), pp.257–68.
- Liu, W. et al., 2015. Measuring retinal blood flow in rats using Doppler optical coherence tomography without knowing eyeball axial length. *Medical physics*, 42(9), pp.5356–62.
- Mancia, G. et al., 2013. 2013 ESH/ESC Guidelines for the management of arterial hypertension. *Blood Pressure*, 22(4), pp.193–278.
- Mapayi, T., Viriri, S. & Tapamo, J.-R., 2015. Adaptive Thresholding Technique for Retinal Vessel Segmentation Based on GLCM-Energy Information. *Computational and Mathematical Methods in Medicine*, 2015, pp.1–11.
- Marín, D. et al., 2011. A new supervised method for blood vessel segmentation in retinal images by using gray-level and moment invariants-based features. *IEEE Transactions on Medical Imaging*, 30(1), pp.146–158.
- Marquardt, D.W., 1963. An Algorithm for Least-Squares Estimation of Nonlinear Parameters. *Journal of the Society for Industrial and Applied Mathematics*, 11(2), pp.431–441.
- Mattace-Raso, F.U.S., 2006. Arterial Stiffness and Risk of Coronary Heart Disease and Stroke: The Rotterdam Study. *Circulation*, 113(5), pp.657–663.
- Mayet, J. & Hughes, A., 2003. Cardiac and vascular pathophysiology in hypertension. *Heart (British Cardiac Society)*, 89(9), pp.1104–9.
- McClintic, B.R. et al., 2010. The relationship between retinal microvascular abnormalities and coronary heart disease: a review. *The American journal of medicine*, 123(4), p.374.e1-7.
- McDonald, D.A., 1968. Regional pulse-wave velocity in the arterial tree. *Journal of applied physiology*, 24(1), pp.73–8.
- McEniery, C.M. et al., 2005. Normal vascular aging: Differential effects on wave reflection and aortic pulse wave velocity - The Anglo-Cardiff Collaborative Trial (ACCT). *Journal of the American College of Cardiology*, 46(9), pp.1753–1760.
- McGeechan, K. et al., 2009. Meta-analysis: retinal vessel caliber and risk for coronary heart disease. *Annals of internal medicine*, 151(6), pp.404–13.
- McGowan, A. et al., 2015. Evaluation of the Retinal Vasculature in Hypertension and Chronic Kidney Disease in an Elderly Population of Irish Nuns. *PloS one*, 10(9), p.e0136434.
- Meglinski, I., Kalchenko, V. & Harmelin, A., 2010. In vivo measurement of skin blood microcirculation using diffusing wave correlation technique. *Dynamics and Fluctuations in Biomedical Photonics VII*, 7563(1), p.75630F–6.
- Mitchell, G.F. et al., 2010. Arterial Stiffness and Cardiovascular Events: The Framingham Heart Study. *Circulation*, 121(4), pp.505–511.
- Mitchell, G.F. et al., 1997. Comparison of techniques for measuring pulse-wave velocity in the rat. *Journal of Applied Physiology*, 82(1), pp.203–210.
- Mitchell, G.F. et al., 2007. Cross-sectional correlates of increased aortic stiffness in the community: The Framingham heart study. *Circulation*, 115(20), pp.2628–2636.
- Mnih, V. et al., 2015. Human-level control through deep reinforcement learning. *Nature*, 518(7540), pp.529–533.
- Montero, D. et al., 2015. The impact of age on vascular smooth muscle function in humans.

- Journal of Hypertension*, 33(3), p.445–53; discussion 453.
- Morgan, W.H. et al., 2004. Retinal venous pulsation in glaucoma and glaucoma suspects. *Ophthalmology*, 111(8), pp.1489–1494.
- Moult, E. et al., 2017. Evaluating anesthetic protocols for functional blood flow imaging in the rat eye. *Journal of Biomedical Optics*, 22(1), p.016005.
- Mudassar, A.A.A. & Butt, S., 2013. Extraction of Blood Vessels in Retinal Images using four different techniques. *Journal of Medical Engineering*, 2013, pp.1–21.
- Mukhopadhyay, P. & Chaudhuri, B.B., 2015. A survey of Hough Transform. *Pattern Recognition*, 48(3), pp.993–1010.
- Muraoka, Y. et al., 2013. Age- and hypertension-dependent changes in retinal vessel diameter and wall thickness: An optical coherence tomography study. *American Journal of Ophthalmology*, 156(4), pp.706–714.
- Nakazato, K. et al., 2005. Evaluation of arterial stiffness in patients with branch retinal vein occlusion. *Ophthalmologica*, 219(6), pp.334–337.
- Nguyen, T.T., Wang, J. & Wong, T., 2007. Retinal vascular changes in pre-diabetes and prehypertension: new findings and their research and clinical implications. *Diabetes care*, 30(10), pp.2708–15.
- Nguyen, T.T. & Wong, T., 2009. Retinal vascular changes and diabetic retinopathy. *Current diabetes reports*, 9(4), pp.277–83.
- Nichols, W., 2005. Clinical measurement of arterial stiffness obtained from noninvasive pressure waveforms. *American Journal of Hypertension*, 18(S1), pp.3–10.
- Nichols, W.W. et al., 2008. Effects of Arterial Stiffness, Pulse Wave Velocity, and Wave Reflections on the Central Aortic Pressure Waveform. *The Journal of Clinical Hypertension*, 10(4), pp.295–303.
- Niiranen, T.J. et al., 2016. Relative Contributions of Arterial Stiffness and Hypertension to Cardiovascular Disease: The Framingham Heart Study. *Journal of the American Heart Association*, 5(11), p.e004271.
- Nilsson, E.D. et al., 2014. Nonlinear association between pulse wave velocity and cognitive function: a population-based study. *Journal of Hypertension*, 32(11), p.2152–7; discussion 2157.
- Okuno, T. et al., 2004. Diurnal variation in microcirculation of ocular fundus and visual field change in normal-tension glaucoma. *Eye (London, England)*, 18(7), pp.697–702.
- Oluleye, S.T., Olusanya, B.A. & Adeoye, A.M., 2016. Retinal vascular changes in hypertensive patients in Ibadan, Sub-Saharan Africa. *International journal of general medicine*, 9, pp.285–90.
- Otto, T., 2000. *Modellierung des retinalen Blutflusses durch Auswertung bewegungskorrigierter Angiographie-Bildfolgen*. University of Heidelberg.
- Palombo, C. & Kozakova, M., 2016. Arterial stiffness, atherosclerosis and cardiovascular risk: Pathophysiologic mechanisms and emerging clinical indications. *Vascular Pharmacology*, 77, pp.1–7.
- Park, J. & Schiffrin, E., 2001. Small artery remodeling is the most prevalent (earliest?) form of target organ damage in mild essential hypertension. *Journal of Hypertension*, 19(5), pp.921–930.
- Pase, M.P. et al., 2010. Healthy middle-aged individuals are vulnerable to cognitive deficits as a result of increased arterial stiffness. *Journal of Hypertension*, 28(8), pp.1724–1729.
- Patton, N. et al., 2005. Retinal vascular image analysis as a potential screening tool for cerebrovascular disease: a rationale based on homology between cerebral and retinal microvasculatures. *Journal of anatomy*, 206(4), pp.319–48.
- Payne, R.A., Wilkinson, I.B. & Webb, D.J., 2010. Arterial stiffness and hypertension: emerging concepts. *Hypertension (Dallas, Tex. : 1979)*, 55(1), pp.9–14.
- Perez-Rovira, A. et al., 2011. VAMPIRE: Vessel assessment and measurement platform for images of the RETina. In *2011 Annual International Conference of the IEEE Engineering*

- in *Medicine and Biology Society*. IEEE, pp. 3391–3394.
- Perona, P. & Malik, J., 1990. Scale-space and edge detection using anisotropic diffusion. *IEEE Transactions on Pattern Analysis and Machine Intelligence*, 12(7), pp.629–639.
- Poels, M.M.F. et al., 2007. Arterial stiffness, cognitive decline, and risk of dementia: the Rotterdam study. *Stroke*, 38(3), pp.888–892.
- Pournaras, C.J. et al., 2008. Regulation of retinal blood flow in health and disease. *Progress in Retinal and Eye Research*, 27(3), pp.284–330.
- Pournaras, C.J. & Riva, C.E., 2013. Retinal blood flow evaluation. *Ophthalmologica*, 229(2), pp.61–74.
- Prenner, S.B. & Chirinos, J.A., 2015. Arterial stiffness in diabetes mellitus. *Atherosclerosis*, 238(2), pp.370–379.
- Qian, X. et al., 2009. A non-parametric vessel detection method for complex vascular structures. *Medical image analysis*, 13(1), pp.49–61.
- Rattathanapad, S., Uyyanonvara, B. & KaewTrakulPong, P., 2011. Vessel Segmentation in Retinal Images Using Graph-Theoretical Vessel Tracking. *MVA*, pp.548–551.
- Reza, A.M., 2004. Realization of the Contrast Limited Adaptive Histogram Equalization (CLAHE) for Real-Time Image Enhancement. *The Journal of VLSI Signal Processing-Systems for Signal, Image, and Video Technology*, 38(1), pp.35–44.
- Ricci, E. & Perfetti, R., 2007. Retinal Blood Vessel Segmentation Using Line Operators and Support Vector Classification. *IEEE Transactions on Medical Imaging*, 26(10), pp.1357–1365.
- Riggio, S. et al., 2010. Pulse wave velocity and augmentation index, but not intima-media thickness, are early indicators of vascular damage in hypercholesterolemic children. *European Journal of Clinical Investigation*, 40(3), pp.250–257.
- Rim, T.H. et al., 2016. Retinal vessel structure measurement using spectral-domain optical coherence tomography. *Eye*, 30(1), pp.111–119.
- Rizzoni, D. et al., 2011. How to Assess Microvascular Structure in Humans. *High Blood Pressure & Cardiovascular Prevention*, 18(4), pp.169–177.
- Rizzoni, D. et al., 2018. New Methods to Study the Microcirculation. *American Journal of Hypertension*, 31(3), pp.265–273.
- Rosenbaum, D. et al., 2016. Relationships between retinal arteriole anatomy and aortic geometry and function and peripheral resistance in hypertensives. *Hypertension Research*, 39(7), pp.536–542.
- Sabanayagam, C. et al., 2015. Retinal microvascular calibre and risk of diabetes mellitus: a systematic review and participant-level meta-analysis. *Diabetologia*, 58(11), pp.2476–85.
- Safar, M.E., 2003. Current Perspectives on Arterial Stiffness and Pulse Pressure in Hypertension and Cardiovascular Diseases. *Circulation*, 107(22), pp.2864–2869.
- Safar, M.E. et al., 2018. Interaction Between Hypertension and Arterial Stiffness. *Hypertension*, 72(4), pp.796–805.
- Safar, M.E., London, G.M. & Plante, G.E., 2004. Arterial Stiffness and Kidney Function. *Hypertension*, 43(2), pp.163–168.
- Salotto, A.G. et al., 1986. Pressure pulse transmission into vascular beds. *Microvascular research*, 32(2), pp.152–63.
- Schneider, C.A., Rasband, W.S. & Eliceiri, K.W., 2012. NIH Image to ImageJ: 25 years of image analysis. *Nature Methods*, 9(7), pp.671–675.
- Seidel, G. et al., 2016. Estimating Retinal Blood Flow Velocities by Optical Coherence Tomography. *JAMA Ophthalmology*, 134(10), p.1104.
- Sethi, S. et al., 2014. Aortic stiffness: pathophysiology, clinical implications, and approach to treatment. *Integrated blood pressure control*, 7, pp.29–34.
- Shirwany, N.A. & Zou, M., 2010. Arterial stiffness: a brief review. *Acta pharmacologica Sinica*, 31(10), pp.1267–76.

- De Silva, D.A. et al., 2012. The relationship between aortic stiffness and changes in retinal microvessels among Asian ischemic stroke patients. *Journal of human hypertension*, 26(12), pp.716–722.
- Singh, N.P. & Srivastava, R., 2016. Retinal blood vessels segmentation by using Gumbel probability distribution function based matched filter. *Computer Methods and Programs in Biomedicine*, 129, pp.40–50.
- Snabre, P., Dufaux, J. & Brunel, L., 2001. Diffuse Laser Doppler Velocimetry from Multiple Scattering Media and Flowing Suspensions. In *Waves and Imaging through Complex Media*. Dordrecht: Springer Netherlands, pp. 369–382.
- Soares, J.V.B. et al., 2006. Retinal vessel segmentation using the 2-D Gabor wavelet and supervised classification. *IEEE Transactions on Medical Imaging*, 25(9), pp.1214–1222.
- Sofka, M. & Stewart, C.V.C. V., 2006. Retinal Vessel Centerline Extraction Using Multiscale Matched Filters, Confidence and Edge Measures. *IEEE Transactions on Medical Imaging*, 25(12), pp.1531–1546.
- Song, S., Wei, W. & Wang, R.K., 2016. Imaging pulse wave velocity in mouse retina using swept-source OCT (Conference Presentation). In V. V. Tuchin et al., eds. International Society for Optics and Photonics, p. 970700.
- Spahr, H. et al., 2017. Comment on “Retinal pulse wave velocity measurement using spectral-domain optical coherence tomography.” *Journal of Biophotonics*, (November), pp.17–19.
- Spahr, H. et al., 2015. Imaging pulse wave propagation in human retinal vessels using full-field swept-source optical coherence tomography. *Optics Letters*, 40(20), p.4771.
- Spronck, B. et al., 2015. Pressure-dependence of arterial stiffness: potential clinical implications. *Journal of Hypertension*, 33(2), pp.330–338.
- Srinivasan, V.J. et al., 2010. Quantitative cerebral blood flow with Optical Coherence Tomography. *Optics Express*, 18(3), p.2477.
- Steigerwalt, R.D.R. et al., 1995. Doppler ultrasonography of the central retinal artery in patients with diabetes and vascular disease treated with topical timolol. , 9(4), pp.495–501.
- Steinman, D.A. & Taylor, C.A., 2005. Flow Imaging and Computing: Large Artery Hemodynamics. *Annals of Biomedical Engineering*, 33(12), pp.1704–1709.
- Steppan, J. et al., 2011. Vascular stiffness and increased pulse pressure in the aging cardiovascular system. *Cardiology research and practice*, 2011, p.263585.
- Struijker-Boudier, H.A.J. et al., 2012. Phenotyping the microcirculation. *Hypertension*, 60(2), pp.523–527.
- Sun, Z., 2015. Aging, arterial stiffness, and hypertension. *Hypertension (Dallas, Tex. : 1979)*, 65(2), pp.252–6.
- Sutton-Tyrrell, K., 2005. Elevated Aortic Pulse Wave Velocity, a Marker of Arterial Stiffness, Predicts Cardiovascular Events in Well-Functioning Older Adults. *Circulation*, 111(25), pp.3384–3390.
- Takai, Y. et al., 2017. Comparisons of retinal vessel diameter and glaucomatous parameters between both eyes of subjects with clinically unilateral pseudoexfoliation syndrome S. Bhattacharya, ed. *PLOS ONE*, 12(6), p.e0179663.
- Theilade, S. et al., 2013. Arterial stiffness is associated with cardiovascular, renal, retinal, and autonomic disease in type 1 diabetes. *Diabetes care*, 36(3), pp.715–21.
- Thevenaz, P., Ruttimann, U.E. & Unser, M., 1998. A pyramid approach to subpixel registration based on intensity. *IEEE Transactions on Image Processing*, 7(1), pp.27–41.
- Thomas, G.N. et al., 2014. Measurement of Macular Fractal Dimension Using a Computer-Assisted Program. *Investigative Ophthalmology & Visual Science*, 55(4), p.2237.
- Tong, J.Y. et al., 2017. Quantitative Retinal Vascular Changes in Obstructive Sleep Apnea. *American Journal of Ophthalmology*, 182, pp.72–80.
- Tozzi, P., Corno, A. & Hayoz, D., 2000. Definition of arterial compliance. *American Journal*

- of Physiology-Heart and Circulatory Physiology*, 278(4), pp.H1407–H1407.
- Triantafyllou, A. et al., 2014. Association between retinal vessel caliber and arterial stiffness in a population comprised of normotensive to early-stage hypertensive individuals. *American Journal of Hypertension*, 27(12), pp.1472–1478.
- Vanfleteren, L.E.G.W. et al., 2014. Arterial stiffness in patients with COPD: the role of systemic inflammation and the effects of pulmonary rehabilitation. *European Respiratory Journal*, 43(5), pp.1306–1315.
- Vennin, S. et al., 2015. Non-invasive calculation of the aortic blood pressure waveform from the flow velocity waveform: a proof of concept. *American Journal of Physiology - Heart and Circulatory Physiology*, p.ajpheart.00152.2015.
- Vlachopoulos, C., Aznaouridis, K. & Stefanadis, C., 2014. Aortic Stiffness for Cardiovascular Risk Prediction. *Journal of the American College of Cardiology*, 63(7), pp.647–649.
- Vlachopoulos, C., Aznaouridis, K. & Stefanadis, C., 2010. Prediction of Cardiovascular Events and All-Cause Mortality With Arterial Stiffness: A Systematic Review and Meta-Analysis. *Journal of the American College of Cardiology*, 55(13), pp.1318–1327.
- Vlachopoulos, C., O'Rourke, M. & Nichols, W.W., 2011. *McDonald's Blood Flow in Arteries 6th Edition: Theoretical, Experimental and Clinical Principles* R. Reneman, ed., CRC Press.
- Wagshul, M.E., Eide, P.K. & Madsen, J.R., 2011. The pulsating brain: A review of experimental and clinical studies of intracranial pulsatility. *Fluids and barriers of the CNS*, 8(1), p.5.
- Wang, J. et al., 2007. Retinal vessel diameter and cardiovascular mortality: Pooled data analysis from two older populations. *European Heart Journal*, 28(16), pp.1984–1992.
- Wang, K.-L. et al., 2013. Aortic Pulse Wave Velocity Improves Cardiovascular Event Prediction. *Journal of the American College of Cardiology*, 63(7), pp.636–646.
- Wang, L., Bhalerao, A. & Wilson, R., 2007. Analysis of Retinal Vasculature Using a Multiresolution Hermite Model. *IEEE Transactions on Medical Imaging*, 26(2), pp.137–152.
- Wang, R. et al., 2014. Cuff-Free Blood Pressure Estimation Using Pulse Transit Time and Heart Rate. *International conference on signal processing proceedings. International Conference on Signal Processing*, 2014, pp.115–118.
- Wang, S.B. et al., 2016. Hypertension is associated with narrower retinal arteriolar calibre in persons with and without coronary artery disease. *Journal of Human Hypertension*, (April), pp.1–5.
- Weber, T. et al., 2004. Arterial Stiffness, Wave Reflections, and the Risk of Coronary Artery Disease. *Circulation*, 109(2), pp.184–189.
- Wiinberg, N., 2000. Measurement of arterial compliance in vivo. *Studies in health technology and informatics*, 71, pp.99–108.
- Williams, B. et al., 2018. 2018 ESC/ESH Guidelines for the management of arterial hypertension: The Task Force for the management of arterial hypertension of the European Society of Cardiology and the European Society of Hypertension: The Task Force for the management of arterial hypertension of the European Society of Cardiology and the European Society of Hypertension. *Journal of hypertension*, 36(10), pp.1953–2041.
- Williams, M. et al., 2015. Retinal microvascular network attenuation in Alzheimer's disease. *Alzheimer's & Dementia: Diagnosis, Assessment & Disease Monitoring*, 1(2), pp.229–235.
- Willoughby, C.E. et al., 2010. Anatomy and physiology of the human eye: effects of mucopolysaccharidoses disease on structure and function - a review. *Clinical & Experimental Ophthalmology*, 38, pp.2–11.
- Willum Hansen, T., 2006. Prognostic Value of Aortic Pulse Wave Velocity as Index of Arterial Stiffness in the General Population. *Circulation*, 113(5), pp.664–670.

- Wink, O., Niessen, W.J. & Viergever, M.A., 2004. Multiscale Vessel Tracking. *IEEE Transactions on Medical Imaging*, 23(1), pp.130–133.
- Womersley, J.R., 1957. An Elastic Tube Theory of Pulse Transmission and Oscillatory Flow in Mammalian Arteries.
- Wong, T., 2006. Fred Hollows lecture: Hypertensive retinopathy - A journey from fundoscopy to digital imaging. *Clinical and Experimental Ophthalmology*, 34(5), pp.397–400.
- Wong, T. et al., 2013. Microvascular Structure and Network in the Retina of Patients With Ischemic Stroke. *Stroke*, 44(8), pp.2121–2127.
- Wong, T., 2004. Retinal Arteriolar Diameter and Risk for Hypertension. *Annals of Internal Medicine*, 140(4), p.248.
- Wong, T. et al., 2002. Retinal arteriolar narrowing and risk of coronary heart disease in men and women. The Atherosclerosis Risk in Communities Study. *JAMA*, 287(9), pp.1153–9.
- Wong, T. et al., 2001. Retinal microvascular abnormalities and incident stroke: the Atherosclerosis Risk in Communities Study. *The Lancet*, 358(9288), pp.1134–1140.
- Wong, T. et al., 2003. Retinal vessel diameters and their associations with age and blood pressure. *Investigative ophthalmology & visual science*, 44(11), pp.4644–50.
- Wong, T. & McIntosh, R., 2005. Hypertensive retinopathy signs as risk indicators of cardiovascular morbidity and mortality. *British Medical Bulletin*, 73–74(1), pp.57–70.
- Wong, T. & Mitchell, P., 2004. Hypertensive Retinopathy. *New England Journal of Medicine*, 351(22), pp.2310–2317.
- Wong, T. & Mitchell, P., 2007. The eye in hypertension. *Lancet (London, England)*, 369(9559), pp.425–35.
- World Health Organization, 2017. Cardiovascular diseases (CVDs). Available at: [https://www.who.int/news-room/fact-sheets/detail/cardiovascular-diseases-\(cvds\)](https://www.who.int/news-room/fact-sheets/detail/cardiovascular-diseases-(cvds)) [Accessed June 8, 2019].
- Wu, H. et al., 2012. Eulerian video magnification for revealing subtle changes in the world. *ACM Trans. Graph.*
- Yang, K. et al., 2012. Association of dilated retinal arteriolar caliber with early age-related macular degeneration: the Handan Eye Study. *Graefe's Archive for Clinical and Experimental Ophthalmology*, 250(5), pp.741–749.
- Yau, J.W.Y. et al., 2011. Retinal Arteriolar Narrowing and Subsequent Development of CKD Stage 3: The Multi-Ethnic Study of Atherosclerosis (MESA). *American Journal of Kidney Diseases*, 58(1), pp.39–46.
- Yazdanfar, S., Rollins, A.M. & Izatt, J.A., 2000. Imaging and velocimetry of the human retinal circulation with color Doppler optical coherence tomography. *Optics Letters*, 25(19), p.1448.
- Yedidya, T. & Hartley, R., 2008. Tracking of Blood Vessels in Retinal Images Using Kalman Filter. In *2008 Digital Image Computing: Techniques and Applications*. IEEE, pp. 52–58.
- Zhang, J. et al., 2014. A retinal vessel boundary tracking method based on Bayesian theory and multi-scale line detection. *Computerized Medical Imaging and Graphics*, 38(6), pp.517–525.
- Zhang, L., Fisher, M. & Wang, W., 2015. Retinal vessel segmentation using multi-scale textons derived from keypoints. *Computerized Medical Imaging and Graphics*, 45, pp.47–56.
- Zhang, M. et al., 2011. Type 2 diabetes is associated with increased pulse wave velocity measured at different sites of the arterial system but not augmentation index in a Chinese population. *Clinical cardiology*, 34(10), pp.622–7.
- Zheng, M. et al., 2014. Age, arterial stiffness, and components of blood pressure in Chinese adults. *Medicine*, 93(29), p.e262.
- Zhi, Z. et al., 2012. Impact of intraocular pressure on changes of blood flow in the retina,

- choroid, and optic nerve head in rats investigated by optical microangiography. *Biomedical Optics Express*, 3(9), p.2220.
- Zhi, Z. et al., 2011. Volumetric and quantitative imaging of retinal blood flow in rats with optical microangiography. *Biomedical optics express*, 2(3), pp.579–91.
- Zhong, W. et al., 2014. Pulse wave velocity and cognitive function in older adults. *Alzheimer disease and associated disorders*, 28(1), pp.44–9.
- Zieman, S.J., Melenovsky, V. & Kass, D.A., 2005. Mechanisms, pathophysiology, and therapy of arterial stiffness. *Arteriosclerosis, Thrombosis, and Vascular Biology*, 25(5), pp.932–943.

Appendix

This section provides supplementary materials required for the calculation of pulse wave velocity in retinal arteries (Chapter 7) considering the effect of blood viscosity according to the Womersley's theory.

The Moens-Korteweg equation relating wave speed to the elastic modulus applies to the thin wall vessel under the assumption of infinite viscosity. In the general case, the velocity of a moving fluid within boundaries is described by the Navier-Stokes equations in computational fluid dynamics. Womersley (1957) applied the theory of fluid flow to blood flow in compliant arteries under a pulsatile pressure. The solutions of the Navier-Stokes equations for one-dimensional oscillating pressure of a frequency of ω assuming the boundary of arteries to be circular contain Bessel functions of a non-dimensional parameter $\alpha = r \sqrt{\frac{\omega \rho}{\mu}}$ (Equation App1).

$$1 - F_{10} = 1 - \frac{2J_1(\alpha j^{\frac{3}{2}})}{\alpha j^{\frac{3}{2}} J_0(\alpha j^{\frac{3}{2}})} \quad (\text{App1})$$

where J_0 and J_1 are the Bessel functions of the first kind of zero and first order respectively, and $j = \sqrt{-1}$.

For an inviscid fluid ($\alpha \rightarrow \infty$) in an isotropic tube (i.e. the mechanical properties of the wall including elastic modulus is constant in all direction) with a thin wall ($h/r < 10$), the wave speed (c_0) is modelled as per the Moens-Korteweg equation.

$$c_0 = \sqrt{\frac{Eh}{2r\rho}} \quad (\text{App2})$$

where E is the elastic modulus and h is the thickness of the wall, r is lumen radius and ρ is fluid density. For real fluid with finite viscosity, the effect of α lowers the wave speed (c) compared to c_0 :

$$\frac{c}{c_0} = \frac{|1 - F_{10}|^{\frac{1}{2}}}{\cos(\frac{\phi + \varphi}{2})} \quad (\text{App3})$$

where $\phi = 0.5$ and $\varphi = 1.0$ are wall viscoelasticity parameters. From Equation App3, the ratio of c/c_0 is dependent on the modulus of $1 - F_{10}$. The values of $1 - F_{10}$ (see Womersley, 1957) rise steeply with increasing α from 0 to 3 and reach an asymptote for $\alpha > 3$ (Figure App1A). For $\alpha > 3$, the c/c_0 ratio is around 0.8 and it falls rapidly for $\alpha < 3$ (Figure App1B).

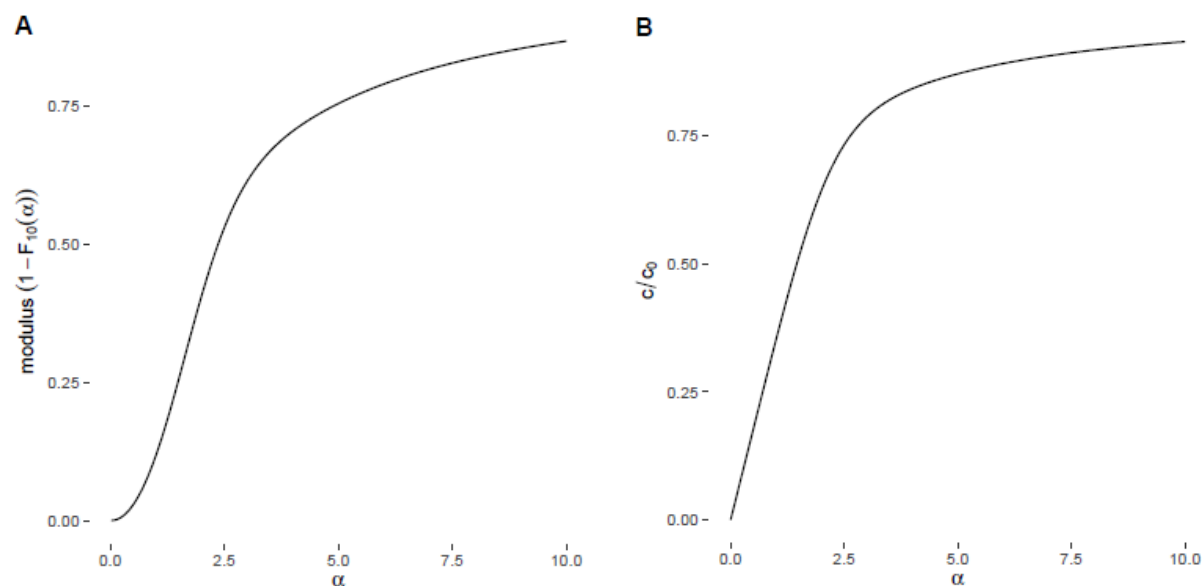


Figure App1. Dependency of (A) the modulus of $1 - F_{10}$ and (B) the ratio c/c_0 on α parameter

Table App1 shows values of α ranged between 0.022 and 0.420 for vessels of diameter from 50 to 300 μm (size of retinal arteries in the rat and human) and for frequencies of 0.5 to 5 Hz (equivalent to heart rate of 30 beats per minute (bpm) to 300 bpm respectively). Figure App2 displays changes of c/c_0 with frequency according to diameter. For a tube the size of human retinal arteries ($D = 150 \mu\text{m}$) the expected pulse wave velocity at a frequency of 1 Hz (i.e. heart rate of 60 bpm) is 3.3% of the estimated value from the Moens-Korteweg equation. Consequently, considering the effect of α and for $c_0 = 5 \text{ m/s}$, the pulse wave velocity of 16 cm/s would be expected in retinal arteries of 150 μm diameter. This would be 37 cm/s in rats at $f = 5 \text{ Hz}$ (heart rate of 300 bpm) for the same c_0 and the same diameter.

Table App1. α and c/c_0 computed for vessels of diameter from 50 to 300 μm and for frequencies of 0.5 to 5 Hz.

D (μm)	f (Hz)	HR (bpm)	α	c/c_0
50	0.5	30	0.022	0.0077
	1	60	0.031	0.0109
	1.5	90	0.038	0.0133
	2	120	0.044	0.0154
	5	300	0.070	0.0243
100	0.5	30	0.044	0.0154
	1	60	0.063	0.0217
	1.5	90	0.077	0.0266
	2	120	0.089	0.0307
	5	300	0.140	0.0491
150	0.5	30	0.066	0.0230
	1	60	0.094	0.0326
	1.5	90	0.115	0.0401
	2	120	0.133	0.0465
	5	300	0.210	0.0743
200	0.5	30	0.089	0.0307
	1	60	0.125	0.0438
	1.5	90	0.153	0.0540
	2	120	0.177	0.0625
	5	300	0.280	0.0989
250	0.5	30	0.111	0.0385
	1	60	0.157	0.0551
	1.5	90	0.192	0.0678
	2	120	0.222	0.0783
	5	300	0.350	0.1238
300	0.5	30	0.133	0.0465
	1	60	0.188	0.0664
	1.5	90	0.230	0.0814
	2	120	0.266	0.0939
	5	300	0.420	0.1486

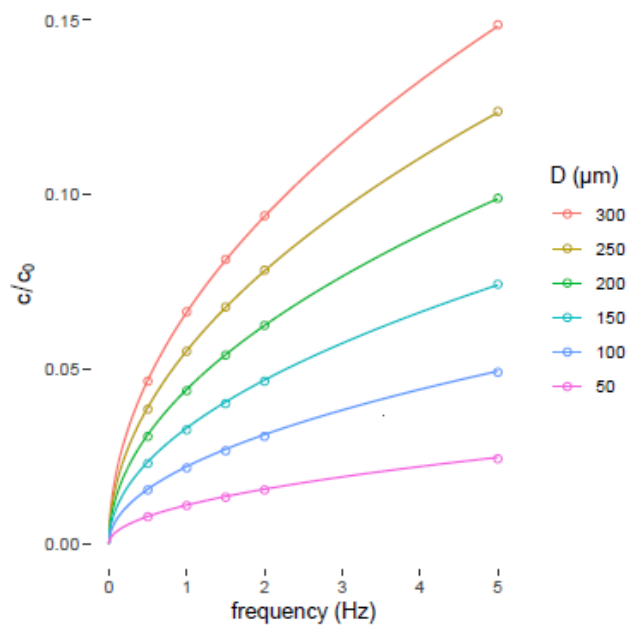


Figure App2. Dependency of c/c_0 on the diameter (D) of the vessel and the frequency of cycling.

Hence, the effect of fluid viscosity will combine with small vessel calibre to give very low values of α , and so result in marked reductions in estimated wave speed in retinal arteries.

References

Womersley, J.R., 1957. An elastic tube theory of pulse transmission and oscillatory ow in mammalian arteries. Tech. Rep. 56-614, Aeronautical Research Laboratory, Wright Air Development Center, Air Research and Development Command, United States Air Force, Wright-Patterson Air Force Base, Ohio.

Ethics approvals

Ethics approvals of this thesis have been removed as they may contain sensitive/confidential content